Preparation of Crystalline Nanostructured Materials by Modification of Layered Silicates Using Organoalkoxysilanes and Organotin Compounds

有機ケイ素アルコキシドと有機スズ化合物を用いた層状ケイ酸塩の修飾による結晶性ナノ構造体の作製

February, 2024

Masashi YATOMI
彌富　昌

Preparation of Crystalline Nanostructured Materials by Modification of Layered Silicates Using Organoalkoxysilanes and Organotin Compounds

有機ケイ素アルコキシドと有機スズ化合物を用いた層状ケイ酸塩の修飾による結晶性ナノ構造体の作製

February, 2024

Waseda University Graduate School of Advanced Science and Engineering

Department of Applied Chemistry, Research on Inorganic Synthetic Chemistry

Masashi YATOMI
彌富　昌

Reviewer of This Thesis

Dr. Atsushi Shimojima

Professor

Waseda University

Thesis advisor

Dr. Yoshiyuki Sugahara

Professor

Waseda University

Dr. Toshiyuki Momma

Professor

Waseda University

Preface

Silica-based materials have features such as high thermal and chemical stability and are applied in catalysis and adsorption through surface modification with organic species and metallic species. For the precise design of these materials, controlling the density and arrangement of modifications is important when using surface silanol (SiOH) groups to immobilize various chemical species. Layered silicates are materials consisting of stacked nanosheets with crystalline silicate frameworks. The well-defined SiOH and silanolate (SiO^-) groups are regularly arranged on the layer surfaces, and counter cations are present between the layers. The surface SiOH/SiO^- groups can be modified with various electrophilic reagents, creating a two-dimensional surface and space with a regular arrangement of chemical species whose local structure is precisely controlled. If the surface SiOH/SiO^- groups of layered silicates can support a high density of metal species with controlled local structures, the application to silica-supported isolated metal catalysts is expected. However, no reports have been published on the preparation of well-defined isolated metal species by precisely controlling the reaction between the metal precursor and the surface SiOH/SiO^- groups. In addition, the introduction of organosilyl groups by silylation reactions has been reported as a way to modify the layer surface organically, leading to the development of selective adsorbents. Organochlorosilanes have been used for high-density and uniform modification because of their high reactivity with surface SiOH groups. However, the organic groups that can be introduced with organochlorosilanes are limited because Si–Cl groups react with highly nucleophilic organic groups. Further development of the metal and organic modification methods is required to design materials that effectively utilize the well-defined SiOH/SiO^- groups of layered silicates.

In this thesis, new approaches to immobilize isolated metal species and dense organic groups on the layer surface of layered silicates by controlling the reactivity of the modifiers are described. First, organotin chlorides were selected as the metal precursor, and the formation of isolated organotin species on the layer surface was investigated. Organotin chlorides are the metal precursors with controllable reactivity in that the number of reaction sites can be adjusted owing to the presence of relatively stable Sn–R (R = organic groups) groups and highly reactive Sn–Cl groups. Furthermore, organotin species immobilized on the silica surface are expected to exhibit Lewis acidity and can be used as catalysts for various reactions. In addition, although organoalkoxysilanes are effective for immobilizing various organic functional groups, high-density modification with uniform local structures is a challenge due to their low reactivity with SiOH groups. Therefore, the use of catalysts and the influence of organic groups on the reactivity of organoalkoxysilanes were investigated.

This thesis is composed of five chapters.

Chapter 1 clarified the significance and challenges in controlling the local structures of chemical species on the interlayer surfaces by summarizing material design through interlayer modification of layered silicates. First, the synthesis, types, and applications of layered silicates are summarized, and the usefulness and specificity of layered silicates are highlighted. Next, the interlayer modification of layered silicates with various metal reagents and silylating agents is summarized, and the issues of each modifier are clarified to demonstrate the significance and originality of this thesis.

Chapter 2 describes the precise immobilization of dimethyltin groups on the layer surface of layered octosilicate, a type of layered silicate. Layered octosilicate has confronting SiOH/SiO^- group pairs on the layer surfaces and can be modified with di-,

tri-, and tetra-functional silylating agents via dipodal (bidentate) silylation. Therefore, the use of dialkyltin dichloride as a modifier would result in the formation of bidentate dialkyltin groups on the layer surface. In this chapter, dimethyltin-modified layered octosilicates were prepared by varying the added amount of dimethyltin dichloride, and detailed characterization was performed to determine the local structure of the dimethyltin groups. The gradual increase in the introduced dimethyltin groups into the interlayer with increasing the amounts was confirmed by powder X-ray diffraction (XRD), solid-state ^{13}C nuclear magnetic resonance (NMR), and elemental analysis. The immobilization of the dimethyltin groups on the layer surface via Si–O–Sn bonds was confirmed by solid-state ^{29}Si NMR. X-ray absorption fine structure (XAFS) analysis was also performed to investigate the local structure of Sn, and four-coordinated Sn species were observed, indicating the successful introduction of bidentate dimethyltin groups on the interlayer surfaces. The maximum degree of modification of the SiOH/SiO^- groups was calculated to be approximately 50%, even though Sn was uniformly introduced throughout the platelet particles. This is considered to be due to the expansion of the silicate framework during the introduction of dimethyltin groups into the SiOH/SiO^- group pairs, resulting in the narrowing of the adjacent SiOH/SiO^- group pairs, which hinder the modification with dimethyltin groups. This suggests that the SiOH/SiO^- groups on the layer surface may be alternately modified with the dimethyltin groups. As described above, well-defined isolated Sn species were successfully created on the layer surface of layered silicates.

Chapter 3 describes the effect of the length of the alkyl group bonded to the Sn on the accessibility of the interlayer for the use of dialkyltin species immobilized in the interlayer as catalysts. Dibutyltin dichloride was selected as a modifier and grafted on the

layer surface of layered octosilicate. The powder XRD pattern showed that the basal spacing of the sample modified with dibutyltin dichlorides was wider than that with dimethyltin dichloride. Furthermore, structural analysis showed that the degree of modification and local structure of Sn in the dibutyltin-modified sample were similar to those in the dimethyltin-modified sample. To evaluate the interlayer accessibility of the dimethyltin- and dibutyltin-modified samples, swelling ability with *N*-methylformamide (NMF) was investigated. Each sample was sonicated in NMF, and XRD measurements of the resulting slurry-like material showed that the basal spacing of the dimethyltin-modified sample changed little, while that of the dibutyltin-modified sample increased by approximately 0.5 nm. In addition, solid-state ^{31}P NMR measurements were performed using trimethylphosphine oxide (TMPO) as a probe molecule to evaluate the acidity of the dialkyltin sites. As a result, only externally deposited TMPO was observed in the dimethyltin-modified sample without intercalation of TMPO into the interlayer. In contrast, the dibutyltin-modified sample showed the presence of TMPO deposited externally, interacting with silanol groups, and interacting with Lewis acid sites. In summary, the immobilization of organotin species with longer alkyl groups improves the accessibility of the interlayer and allows the use of Lewis acid sites on the layer surfaces.

Chapter 4 describes the factors that improve the reactivity of organoalkoxysilanes in silylation to expand the types of organic functional groups that can be densely immobilized on the layer surfaces. First, the effect of fluoride ions on the silylation was examined. Fluoride ions are known to coordinate with the silicon of alkoxysilanes, forming highly coordinated silicon species and promoting nucleophilic attack from water and silanol groups. Therefore, the reactivity of organoalkoxysilanes to SiOH/SiO$^-$ groups on the layer surface is expected to be improved. Tetrabutylammonium

fluoride (TBAF), soluble in organic solvents, was used as the fluoride ion source. In silylation with alkyltriethoxysilanes with different lengths of the alkyl chain, the addition of a tetrahydrofuran solution of TBAF increased the degree of silylation. To investigate the effect of TBAF, the amount of TBAF was varied during the silylation with octyltriethoxysilane. The degree of silylation increased from 33% to 54%, 60%, and 71% when the amount of TBAF was varied from 0, 0.027, 0.27, and 0.54 equivalents to the reaction site. The progress of hydrolysis and condensation between silylating agents at high addition amounts of TBAF was observed. The addition of TBAF at 2.7 mol% relative to the reaction site increased the degree of silylation by 21%, indicating that TBAF acts as a catalyst. Furthermore, the effect of TBAF addition on silylation with 3-mercaptopropyltriethoxysilane (MPTES), which can be applied as a metal support or acid catalyst, was investigated. The degree of silylation was higher than 80% with and without TBAF. On the other hand, when mesoporous silica was silylated with MPTES, a high degree of silylation was not observed. Therefore, ion-dipole interaction between MPTES with polar functional groups and the layer surface of layered silicates, where SiO^- groups and cationic pairs exist, might contribute to the promotion of the silylation. In summary, it was shown that the addition of a catalyst and the interaction between the silylating agent and the layer surface are important factors in the silylation of layered silicates with organoalkoxysilanes.

Chapter 5 summarizes the results obtained in this thesis. In this thesis, the immobilization of dimethyltin groups with precisely controlled local structure and arrangement on the layer surfaces was successfully achieved by the reaction of organotin chlorides with the confronting $SiOH/SiO^-$ groups on the layer surfaces of layered silicates. Furthermore, the alkyl chain length was found to be an important factor in the utilization

of alkyltin species immobilized between the layers. In the silylation of layered silicates with organoalkoxysilanes, it was also shown that the modification density can be increased by using fluoride ion catalysts and by designing reaction systems that consider the interaction between the layer surface and the silylating agent. The findings in this thesis will expand the scope of materials design using layered silicates, leading to the creation of novel silica-based functional materials with advanced adsorption and catalytic properties.

Contents

Preface

Chapter 1: *General Introduction* ……*1*

1.1 Layered silicates

1.1.1 General characteristics

1.1.2 Discovery and synthesis of layered silicates

1.1.3 Structure determination of layered silicates

1.1.4 Summary

1.2 Intercalation reaction of layered silicates

1.2.1 Intercalation through cation exchange

1.2.2 Intercalation through interaction with polar organic molecules

1.2.3 Morphology control of layered silicates after intercalation reaction

1.2.3.1 Conversion into nanosheets through delamination

1.2.3.2 Conversion into nanoscrolls

1.2.3.3 Conversion into mesoporous silicas

1.2.4 Summary

1.3 Immobilization of chemical species via covalent bonds on the interlayer surfaces

1.3.1 Silylation reactions

1.3.1.1 Interlayer silylation of layered silicates with chlorosilanes

1.3.1.2 Interlayer silylation of layered silicates with alkoxysilanes

1.3.2 Esterification reactions

1.3.3 Modification with metal reagents

1.3.4 Summary

1.4 Purpose and significance of this thesis

1.5 References

Chapter 2: *Immobilization of Isolated Dimethyltin Species on Crystalline Silicates through Surface Modification of Layered Octosilicate* ……*43*

2.1 Introduction

2.2 Experimental Methods

2.3 Results and Discussion

2.4 Conclusion

2.5 References

Chapter 3: *Swelling Ability and Lewis Acidity of Layered Octosilicate Modified with Isolated Dialkyltin Species* ……77

3.1 Introduction

3.2 Experimental Methods

3.3 Results and Discussion

3.4 Conclusion

3.5 References

Chapter 4: *Interlayer Silylation of Layered Octosilicate with Organoalkoxysilanes: Effects of Tetrabutylammonium Fluoride as a Catalyst and Functional Groups of Silanes* ……97

4.1 Introduction

4.2 Experimental Methods

4.3 Results and Discussion

4.4 Conclusion

4.5 References

Chapter 5: *General Conclusions* ……135

List of Achievements ……138

1. Original articles related to this thesis
2. Oral or poster presentations

Acknowledgements ……140

Chapter 1

General Introduction

1.1 Layered silicates

1.1.1 General characteristics

Layered silicates are two-dimensional materials consisting of alternately stacked crystalline silicate layers and interlayer cations. They are also called "layered polysilicates" to distinguish them from clay minerals such as smectite. The layers are negatively charged by the surface SiO^- groups to compensate for the interlayer positive charges. The framework of layered silicates is terminated by dense SiOH and SiO^- groups. The position and local structure of the surface SiOH/SiO^- groups and counter cations are crystallography-defined and are consequently regularly arranged. The counter cations are mainly monovalent hydrated alkali metals and ammonium ions, which can be replaced with other cations by ion exchange. In addition, the spacing between the layers varies depending on the size of the interlayer cations. Furthermore, regularly arranged SiOH/ SiO^- groups on the layer surface can be modified with various chemical species by nucleophilic reactions, resulting in the regular arrangement of modifiers on the layer surface.[1] Therefore, layered silicates, possessing features such as regularly arranged SiOH/ SiO^- groups and controllable layer spaces, are distinctly different from other silica-based materials (crystalline silica such as quartz and zeolite; amorphous silica such as mesoporous silica and silica particles), and are applicable for various applications including adsorption and catalysis through diverse materials design (Fig. 1.1).

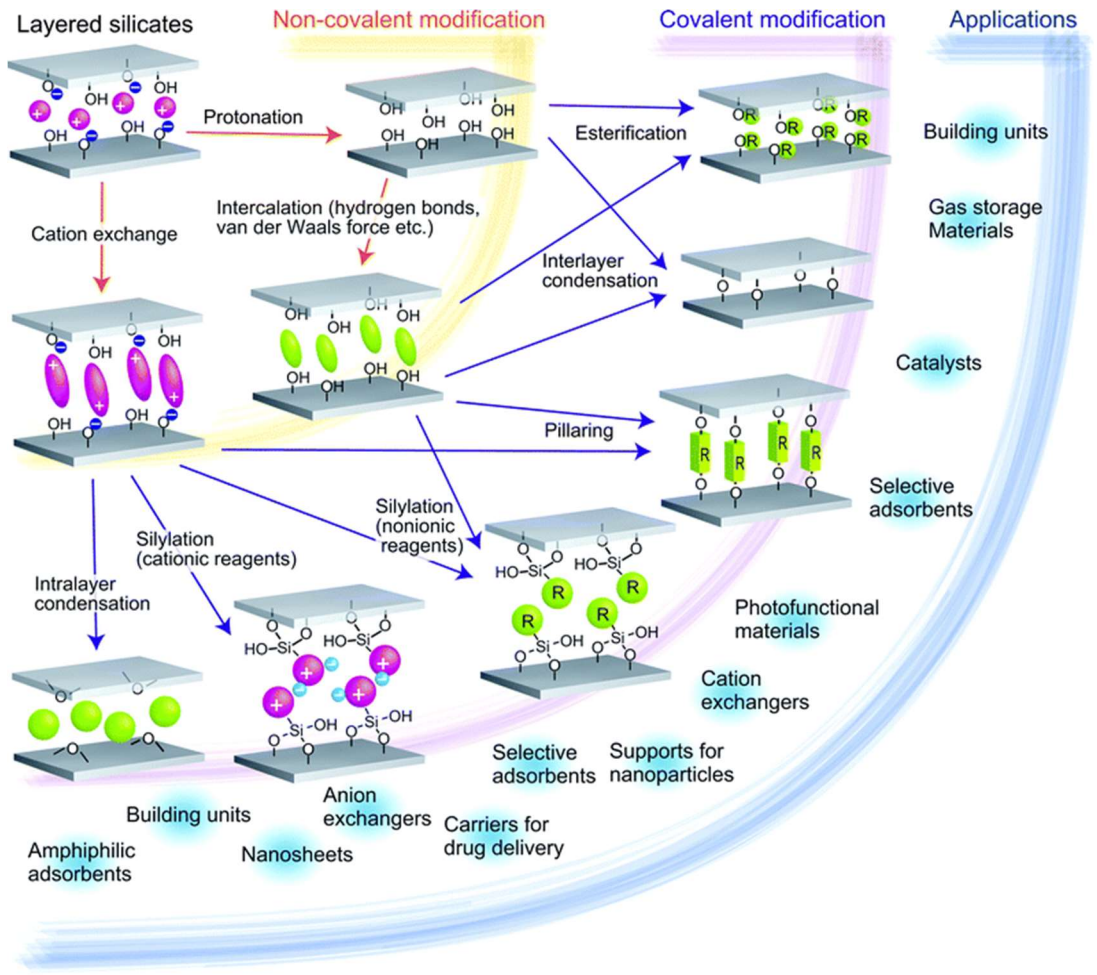

Fig. 1.1 Material design of layered silicates through various reactions.[1]
Reprinted with permission from Ref. 1. Copyright 2011 Royal Society of Chemistry.

Various types of layered silicates with different network structures of SiO_4 tetrahedra, interlayer cations, and stacking modes have been discovered in nature and chemically synthesized, and currently more than 40 types[2] have been identified. The morphology of the crystals is mainly plate-like with a lateral size in the range of several micrometers square and a thickness of tens of nanometers. Some types have a rosette-like morphology consisting of aggregated multiple plate-like particles.

1.1.2 Discovery and synthesis of layered silicates

(i) Discovery of natural layered silicates

Natural layered silicates with interlayer hydrated sodium cations are found in limited areas: in 1967, two different compositions of layered silicates, magadiite ($NaSi_7O_{13}(OH)_3 \cdot 3H_2O$) and kenyaite ($Na_2Si_{22}O_{41}(OH)_8 \cdot 6H_2O$), were discovered in Lake Magadi, Kenya.[3] In 1970, makatite ($Na_2Si_4O_8(OH) \cdot 4H_2O$) with a higher proportion of sodium was discovered in the same lake.[4] In 1972, kanemite was discovered in Lake Chad.[5] These lakes have alkaline water quality, including high levels of trona (sodium carbonate and sodium bicarbonate), and layered silicates are considered to be generated in the limited environment of their subsurface. These layered silicates attracted attention because of their high crystallinity, large basal spacing, and water content.

(ii) Synthesis of layered silicates with alkali metal cations

Layered silicates with interlayer alkali metal cations, also called layered alkali silicates, are synthesized by hydrothermal reactions under basic conditions. In 1952, McCulloch synthesized layered silicates with a Na_2O/SiO_2 ratio of 9.4 and 13.1, rectangular platelet shapes, and large basal spacings from silica gel and sodium hydroxide by hydrothermal reactions at 100 °C.[6] These layered silicates are considered to be layered octosilicate ($Na_2O/SiO_2 = 9.4$) and magadiite ($Na_2O/SiO_2 = 13.1$). Iler synthesized plate-like crystals with a Na_2O/SiO_2 ratio of 8.0 from colloidal silica by a similar hydrothermal method, which is later called Ilerlite (layered octosilicate, RUB-18).[7] In addition, kanemite,[8] makatite,[9] and kenyaite,[10] were also hydrothermally synthesized. Layered disilicates with various crystal systems (α-,[11] β-,[12] γ-,[13] δ-,[13] and ε-$Na_2Si_2O_5$[14]) have also been synthesized. As a layered alkali silicate containing alkali metal cations other than

Na in the interlayer, $NaLiSi_2O_5 \cdot 2H_2O$ (Silinaite),[15] $Li_2Si_2O_5$,[16] $Na_{1.55}K_{0.45}Si_2O_5$,[17] $NaKSi_2O_5$,[18] $Na_{0.67}K_{1.33}Si_2O_5$,[18] $KHSi_2O_5$[19] (K-LDS[20]), $K_2Si_2O_5$,[16] $RbHSi_2O_5$,[21] and $CsHSi_3O_7$[21,22] have been synthesized.

The morphology of the crystals can be controlled by the additives during the hydrothermal synthesis. Feng and Balkus, while investigating various silica and alkali metal sources and reaction times for the synthesis of octosilicate, magadiite, and kenyaite, found that the addition of poly(ethylene glycol) (PEG) caused the change of the normally plate-like form of octosilicate into rosette-like shape.[23] In contrast, Yuan *et al.* found that adding NaF and PEG during magadiite synthesis caused magadiite, which is usually in a rosette-like shape, to become plate-like.[24] Because controlling the particle size and crystallinity of layered silicates is also important, Iwasaki *et al.* investigated the influence of seed crystals on the hydrothermal synthesis of layered octosilicate.[25] As a result, the addition of highly crystalline octosilicate as seed crystals accelerated the crystal growth of octosilicate. Furthermore, adding seed crystals increased the particle size of octosilicate plates up to approximately twice as much.

(iii) Synthesis of layered silicates with quaternary ammonium cations

Using organic structure directing agents (OSDA), layered zeolites with quaternary ammonium cations as a counter cation have also been synthesized. These groups possess crystalline nanosheets composed of SiO_4 tetrahedra and $SiOH/SiO^-$ groups on the layer surfaces and thus can be considered a type of layered silicates. In 1983, Whittam reported Nu-6(1),[26] a precursor of NSI-type zeolite, which is the first layered zeolite. Subsequently, synthesis of EU-19,[27] PREFER (precursor of FER-type zeolite),[28] ITQ-2,[29] ITQ-8,[30] PLS-1,[31] ERS-12,[32] UCB-1,[33] UCB-4,[34] MCM series

developed by Mobil Corporation (MCM-22P,[35] -47,[36] -65,[37] -69[38]…), RUB series developed by Gies *et al.* at Ruhr University (RUB-6,[39] -15,[40] -20,[41] -36,[42] -38,[41] -39,[43] -40,[41] -48,[41] -51,[44] -52,[45] -53,[45] -55[46]…), and HUS series developed by Hiroshima University (HUS-1,[47] -2,[48] -5,[49] -7[50]…) was reported.

(iv) Incorporation of heteroatoms into the framework of layered silicates

Layered silicates with isomorphic substitution of Si in the layer framework with heteroatoms have been synthesized by hydrothermal methods. Isomorphous substitutions with trivalent elements have been reported for magadiite substituted with B, Al, and Ga,[51–54] kanemite substituted with Al or Ga,[55,56] and Al-containing layered octosilicates.[57,58] These layered silicates isomorphically substituted with trivalent elements can be used as Brønsted acid catalysts. Isomorphic substitution with tetravalent Ti and Sn is also possible. Kanemite,[59] magadiite,[60–62] and octosilicate,[60,61] including these metals, have been synthesized, which are expected to apply to Lewis acid catalysts.

1.1.3 Structure determination of layered silicates

It was known early on that layered silicates are stacked crystalline silicate nanosheets by powder XRD, electron microscopy, and elemental analyses. In this section, the history of crystal structure determination is described. Single-crystal X-ray structure analysis is a typical analysis that significantly contributes to the determination of crystal structures. The relatively large single crystals and the inferred initial structure model make it practically possible to determine the crystal structure. Because the makatite particle size can be increased by adding triethanolamine during synthesis, its structure (Fig. 1.2(A)) was determined by single-crystal X-ray structure analysis in 1982.[9]

However, it is challenging to apply single-crystal X-ray structural analysis to most layered silicates because they are crystalline fine powders.

Gies *et al.* determined the crystal structure of RUB-18 (layered octosilicate and Ilerlite, Fig. 1.2(B)) regarding the silicate framework structure and Na arrangement using Rietveld refinement.[63] In addition, the hydrogen bonding network, which is difficult to analyze by only X-ray analysis, was determined by solid-state ^{1}H and ^{29}Si NMR.[64] The chemical formula of the unit cell of four silicate layers is $Na_8[Si_{32}O_{64}(OH)_8]\cdot 32H_2O$, where one layer consists of $[5^4]$cage (four five-membered rings) composed of eight SiO_4 tetrahedra. The layer surfaces have parallel grooves in 1D direction, which are mutually perpendicular to each other on the front and back surfaces of the layers. The hydrated Na cations between the layers were arranged along the grooves on the layer surfaces in a 1D structure of edge-sharing NaO_6 octahedra (Figs. 1.2(B) (a) and (b)). Furthermore, the structure of kanemite (Fig. 1.2(C)) was successfully determined by the same method.[65] However, it is challenging to estimate the initial structure of the thicker silicate layers and obtain clean powder patterns for magadiite and kenyanite, and many structural refinements have been attempted. In particular, several inferred structures have been proposed for magadiite because of its prior application. Pinnavaia *et al.* (1986)[66] and Garcés *et al.* (1988)[67] tried to determine the structure using powder XRD, FT-IR, and solid-state ^{29}Si NMR, and Ide *et al.* (2018)[68] used PDF analysis, but no widely accepted structure had been proposed.

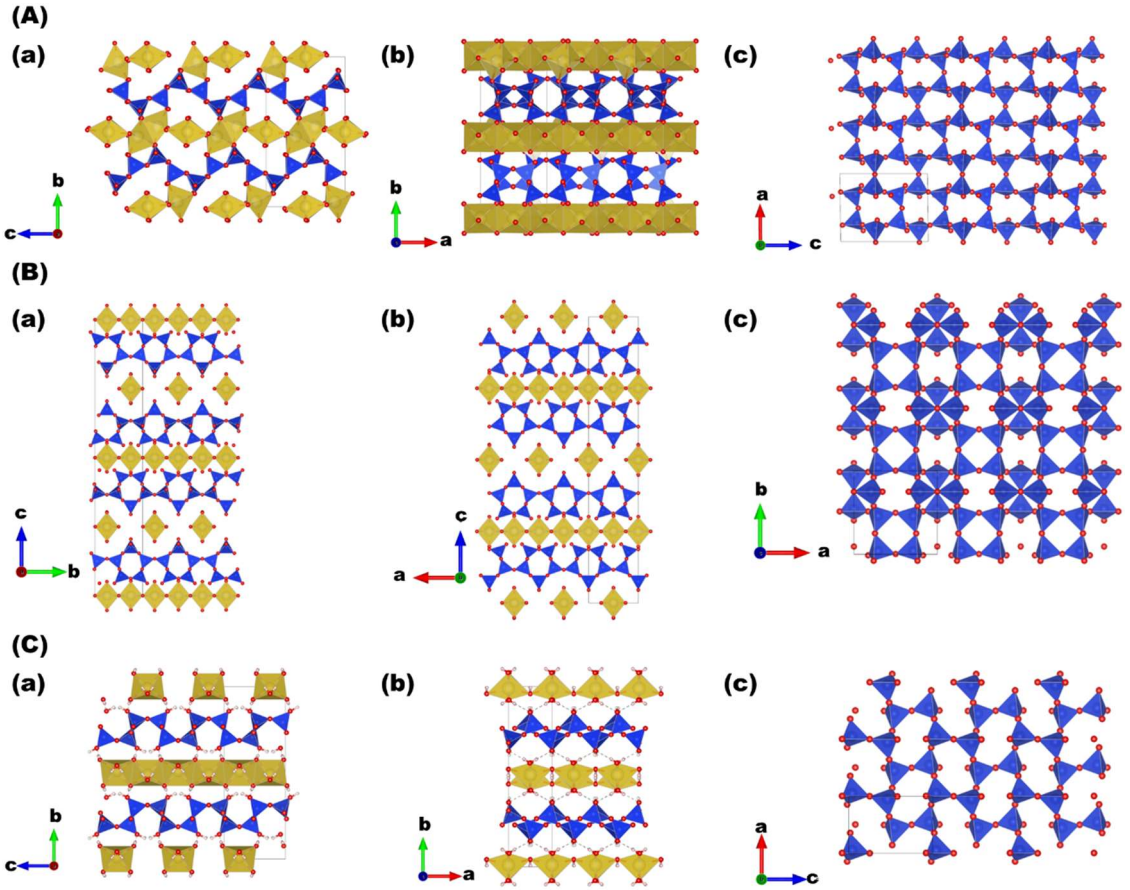

Fig. 1.2 Crystalline structural models of (A) makatite, (B) layered octosilicate (Ilerite or RUB-18), and (C) kanemite.

Recent developments in electron microscopy techniques have made it possible to determine the crystal structure with a few nm orders size using 3D electron diffraction (ED). The structures of synthetic[69] and natural[70] magadiite ($Na_{1.9}Si_{14}O_{28}(OH)_{2.1}\cdot 7.4H_2O$ and $Na_{1.9}Si_{14}O_{28}(OH)_{2.4}\cdot 10.2H_2O$) and kenyaite ($H_{0.2}Na_{1.9}Si_{20}O_{40}(OH)_2\cdot 6.9H_2O$)[71] were determined by Marler's group by 3D ED (Fig. 1.3(A) and (B)). Thus, the structures of layered silicates are gradually elucidated with the progress of analytical techniques.

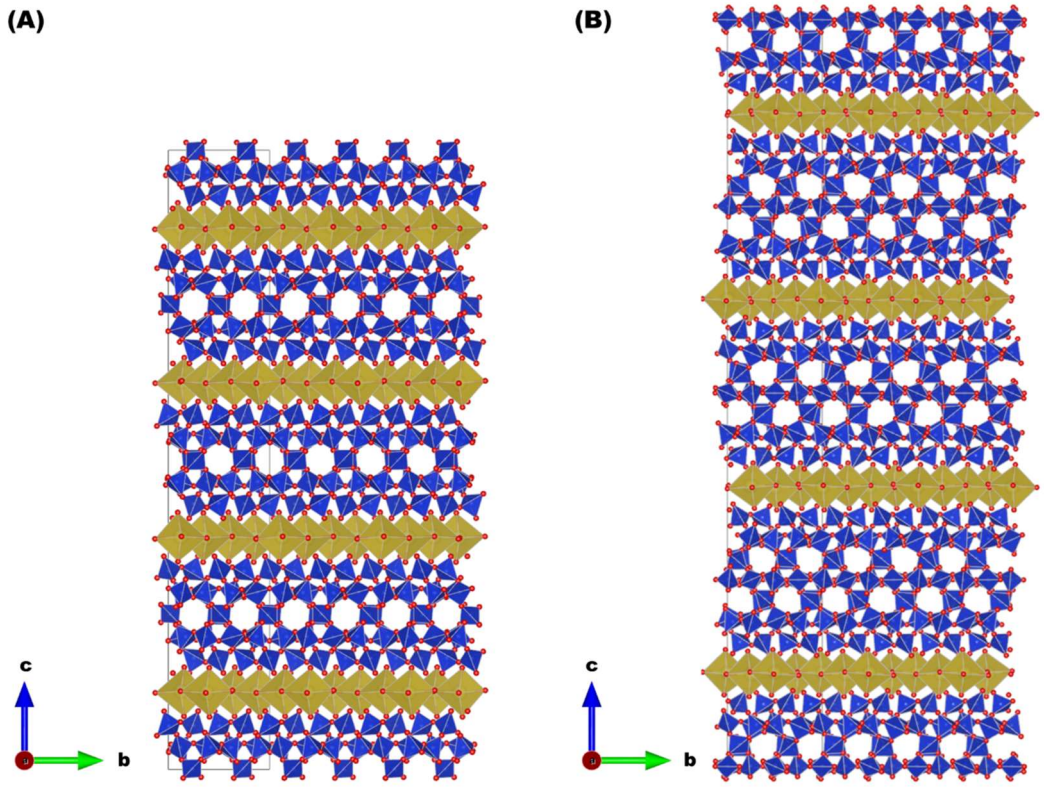

Fig. 1.3 Crystalline structural models of (A) synthetic magadiite and (B) kenyaite.

1.1.4 Summary

Layered silicates are unique silica-based materials due to their nano-scale thin layers and crystallinity. Their structural variety is abundant, and new crystal structures have been determined in recent years. Therefore, the material design utilizing the properties of the layers themselves, the layer surfaces, and the interlayers is expected.

1.2 Intercalation reaction of layered silicates

1.2.1 Intercalation through cation exchange

The interlayer cations of layered silicates are ion-exchangeable, and their high cation exchange capacity has long attracted attention. Because ion exchange proceeds due to the concentration gradient between the cations within the layered silicate and the cations in the solution, full ion exchange is completed by stirring for several hours in an aqueous solution containing an enriched cation and then replacing the solution with a fresh aqueous solution several times. Iler confirmed the successful ion exchange of Na-type layered octosilicate by H^+, Li^+, Mg^{2+}, Ni^{2+}, Cu^{2+}, and cetyltrimethylammonium$^+$ ($C_{16}TMA^+$), with the layer spacing depending on the size of the cation.[7]

Lagaly *et al.* fully ion-exchanged magadiite with various organic cations and investigated their basal spacings.[72] It was confirmed that the basal spacing increases linearly with the length of the alkyl groups. An interlayer structure in which the alkylammonium in the all-*trans* conformation forms a vertical bilayer arrangement between the layers of magadiite has been proposed. However, it was also noted that a monolayer arrangement may be formed under some conditions. The interlayer structure can be estimated based on some analyses. The conformation of alkylammonium is characterized using solid-state ^{13}C NMR because signals derived from all-*trans* and *trans*/*gauche* conformation of alkyl chain are observed at 33 and 30 ppm, respectively. Moreover, by comparison of the gallery height, which is the basal spacing of the sample subtracted by the thickness of the layers, to the ideal length of alkylammonium cation, the arrangement (monolayer or bilayer) and angle of alkylammonium cations can be elucidated. For layered silicic acids obtained by acid treatment of layered silicates, alkylamines can be used to obtain intercalation compounds similar to those obtained by

ion exchange with ammonium cations.[73] Such layered silicates with significantly expanded layer spacing serve as a valuable precursor for the interlayer reactions described below.

1.2.2 Intercalation through interaction with polar organic molecules

Interlayer alkali metal cations in layered silicates are basically hydrated, and changes in water content cause slight changes in the basal spacing. However, the interaction of alkali metals with SiOH/SiO^- groups and hydrated water on the layer surfaces is strong, making intercalation other than ion exchange difficult. On the other hand, layered silicic acids have layer surfaces covered with polar SiOH groups and can intercalate a variety of molecules. Lagaly *et al.* reported intercalation of water, alcohols, ketones, nitriles, amines, amides, urea derivatives, nitroxides, and sulfoxides to H-type magadiite.[74] In particular, amines, basic organic molecules, are intercalated through acid-base reactions with interlayer SiOH groups as the driving force. The other molecules, polar molecules with high dielectric constants, are intercalated driven by dipole interactions.

1.2.3 Morphology control of layered silicates after intercalation reaction

1.2.3.1 Conversion into nanosheets through delamination

Even when the layer spacing is expanded by intercalation of guest species into the layered silicate, the layers do not separate on their own, resulting in reversible swelling between the layers. There are two methods for delamination: one is to add shearing force, such as ultrasonic waves, and the other is to use repulsive osmotic swelling. Although the obtained anisotropic crystalline silica nanosheets are expected to have high

specific surface area and gas barrier properties, exfoliation is not easy because of the strong interlayer attraction caused by the large lateral size and layer charge.

Exfoliation of layered silicate was performed by ultrasonicating didodecyldimethylammonium-intercalated layered octosilicate in pentane.[75] Utilizing ammonium with two long-chain alkyl groups suppresses the interlayer attraction and the packing of alkyl groups between layers. However, broken sheets were obtained, and the large lateral size of layered silicates cannot be fully exploited. Subsequently, exfoliations by expanding the interlayer of RUB-15 with cetyltrimethylammonium followed by heating and stirring in polystyrene[76] or by introducing tetrabutylammonium into layered octosilicate followed by sonication in water/alcohol solution[77] have been reported. These are delamination methods based on interlayer expansion and hydrophobization and external shearing force, which cannot avoid the destruction of the layers. Recently, Loch *et al.* showed that layered octosilicate can be spontaneously exfoliated in water by ion exchange with protonated *N*-methyl-D-glucamine (meglumine).[78] This method is quite distinct from conventional delamination methods. The sheets were less likely to break because the interlayer spaces were more hydrophilic, facilitating the introduction of water and allowing them to exfoliate without shearing forces.

1.2.3.2 Conversion into nanoscrolls

A phenomenon of rolling up of layers (scrolling) derived from study for exfoliation of layered silicate has also been reported. Asakura *et al.* produced silicate nanoscrolls by solvothermal treatment of layered octosilicate ion-exchanged with dimethyldioctadecylammonium bromide ($(C_{18})_2$DMABr) in a heptane solvent (Fig. 1.4).[79] The difference in the structure of the front and back of the layer is considered

crucial for this scrolling to occur. The octosilicate is structured with grooves that intersect at 90 degrees on the front and back of the layer, which can induce different tensions on the front and back of the layer. In addition, not only $(C_{18})_2DMA^+$, interacting with the silanolate groups, but also physisorbed $(C_{18})_2DMABr$ is present on the layer surface. In addition, not only $(C_{18})_2DMA^+$, interacting with the silanolate groups, but also physisorbed $(C_{18})_2DMABr$ is present on the layer surface. Solvothermal treatment causes desorption of $(C_{18})_2DMABr$ from the top of the layer, leading to a decrease in $(C_{18})_2DMA$ density at the topmost layer and upward sheet roll-up. Such silicate nanoscrolls have attracted attention as tubular structured materials with regularly arranged $SiOH/SiO^-$ groups.

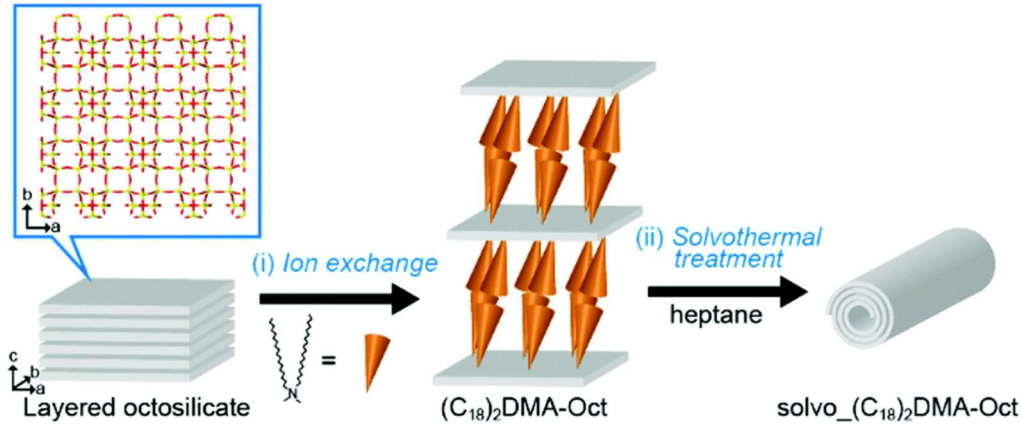

Fig. 1.4 Formation of nanoscrolls from layered octosilicate.[79]
Reprinted with permission from Ref. 79. Copyright 2019 Royal Society of Chemistry.

1.2.3.3 Conversion into mesoporous silicas

Mesoporous silicas are silica-based materials with regular pores in the range of 2–50 nm and are applied to adsorbent and catalysis owing to their high specific surface area. Yanagisawa *et al.* synthesized a mesoporous silica KSW-1 with 1D channels of 2–4 nm in diameter by heat treatment of kanemite intercalated with alkyltrimethylammonium.[80] Such porosity is considered to be caused by the bending of

the layers along with alkylammonium micelles upon heating. However, because the crystallinity of KSW-1 is not high, post-treatments such as ion exchange, acid treatment, and hydrothermal treatment were investigated to achieve higher crystallinity. FSM-16[81,82] with 2D hexagonal 1D channels and KSW-2[83] with 2D orthorhombic 1D channels (Fig. 1.5) were synthesized from kanemite derivatives. The types of layered silicates were also expanded, converting makatite,[84] layered disilicate,[85,86] and layered octosilicate[87,88] to mesoporous silica. KSW-1 was the first mesoporous silica in the world, and mesoporous silica derived from such layered silicates is unique in having crystalline wall surfaces.[89,90]

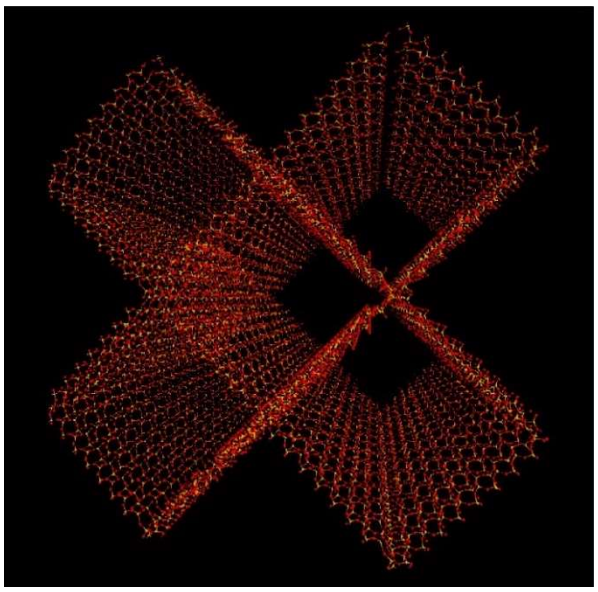

Fig. 1.5 Possible structural model of KSW-2.[89]
Reprinted with permission from Ref. 89. Copyright 2008 American Chemical Society.

1.2.4 Summary

Layered silicates can intercalate various cation species through ion exchange because they have exchangeable cations between the layers. In particular, protonated layered silicates, called layered silicic acids, can intercalate various organic molecules through acid/base reactions and hydrogen bonds as a driving force. Interlayer compounds

obtained by intercalation reactions not only increase the accessibility of SiOH/SiO^- groups on the interlayer surfaces but also lead to various morphological conversions such as nanosheets, nanoscrolls, and mesoporous silicas.

1.3 Immobilization of chemical species via covalent bonds on the interlayer surfaces

As described above, the interlayer SiOH and SiO^- groups of layered silicate can reversibly adsorb various compounds via ionic and dipole interactions. In addition, immobilizing chemical species via irreversible covalent bonding is likewise a critical modification method. Here, the reports of covalent immobilization of electrophilic reagents on the layer surface using the nucleophilic attack property of the SiOH group are presented.

1.3.1 Silylation reactions

Silylation is a reaction to introduce silyl groups ($–SiR_3$) to a molecule or solid surface. Silane compounds used for silylation are called "silylating agents" and are often referred to as "silane coupling agents" in terms of introducing organic functional groups to inorganic solid surfaces. For the silylation of silica-based materials, chlorosilane and alkoxysilane are mainly used as a silylating agent. The silica surfaces are covered with silanol groups, which nucleophilically attack the silylating agent, resulting in silylation via siloxane (Si–O–Si) bonds.

$$\equiv SiOH + ClSiR_3 \rightarrow \equiv SiOSiR_3 + HCl \qquad (1)$$

$$\equiv SiOH + (R'O)SiR_3 \rightarrow \equiv SiOSiR_3 + R'OH \qquad (2)$$

(R and R' denotes organic groups)

A similar reaction can be used on the layer surfaces of layered silicates to introduce silyl groups via Si–O–Si bonds. As for the choice of silylating agent, chlorosilanes are more reactive than alkoxysilanes and can densely silylate the layer surfaces. However, the types of organic functional groups are limited because Si–Cl

groups react with highly nucleophilic organic groups. On the other hand, alkoxysilanes can modify the interlayer with various organic functional groups without generating corrosive HCl as a by-product. Thus, it is important to select silylating agents based on the desired functionality and reactivity.

1.3.1.1 Interlayer silylation of layered silicates with chlorosilanes

Chlorosilanes are silane compounds represented by R_nSiCl_{4-n} (R = organic species; n = 0–3) and have very high reactivity toward silanol groups on the layer surfaces. When the number of Cl bonded to Si is 1, 2, 3, or 4, they are called mono-, bi-, tri-, and tetra-functional chlorosilanes, respectively. Selecting a chlorosilane with a suitable functional number is important depending on the location of the $SiOH/SiO^-$ groups on the layer surface. Because chlorosilane reacts with silanol to produce HCl as a byproduct, basic molecules such as pyridine and triethylamine are also added for trapping.

Although chlorosilanes are highly reactive with silanol groups, interlayer $SiOH/SiO^-$ groups in Na-type layered silicates cannot be silylated. This is considered to be due to the narrow and hydrophilic nature of the interlayer spaces, which prevents hydrophobic chlorosilanes from accessing, so that only the outermost surface is silylated. In 1980, Ruiz-Hitzky and Rojo first succeeded in interlayer silylation of layered silicates (Fig. 1.6).[91] First, Na-type magadiite was protonated by acid treatment and intercalated with polar organic substance (dimethyl sulfoxide (DMSO), *N*-methylformamide (NMF), or *N,N*-dimethylformamide (DMF)) to enlarge the interlayer. By adding trimethylchlorosilane, the interlayer trimethylsilylation was performed. The above problems of interlayer spaces have been solved through interlayer compounds intercalated with polar organic molecules. However, it was difficult to introduce silyl

groups other than trimethylsilyl groups due to the limited expansion of interlayer spacing in this method.[92]

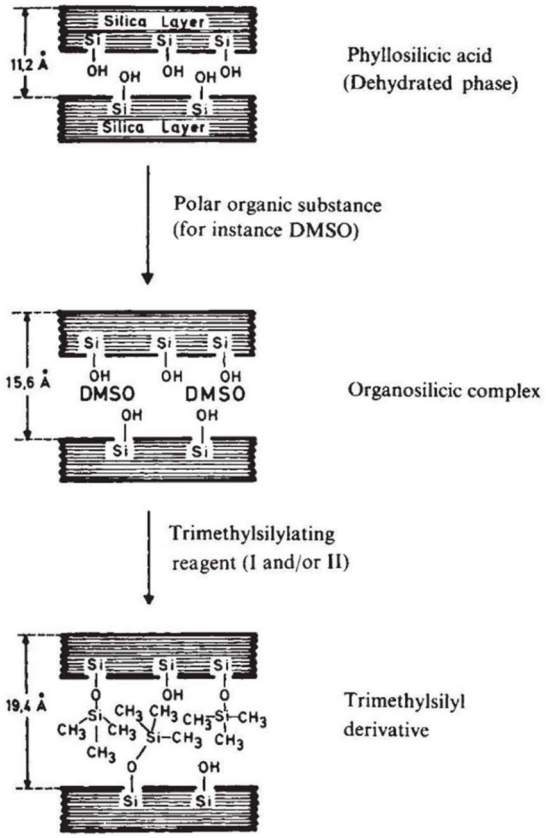

Fig. 1.6 Interlayer silylation of protonated magadiite intercalated with DMSO.[91]
Reprinted with permission from Ref. 91. Copyright 1980 Springer Nature.

Yanagisawa *et al.* (1988) ion-exchanged the interlayer Na^+ of magadiite and kenyaite with long-chain alkylammonium cations and subsequently silylated the interlayer compounds with more expanded interlayers as a precursor.[93–95] This approach enabled interlayer silylation with bulky silylating agents such as diphenylmethylchlorosilane and allyldimethylchlorosilane as well as trimethylchlorosilane. Ogawa *et al.* (1998)[96] and Okutomo *et al.* (1999)[97] reported that interlayer silylation with triethylchlorosilane, triisopropylchlorosilane, butyldimethylchlorosilane, octyldimethylchlorosilane, octadecyldimethylchlorosilane,

and [2-(perfluorohexyl)ethyl]dimethylchlorosilane. In subsequent interlayer silylation, the interlayer expanded layered silicates with alkylammonium cations are used as a precursor.

The development flow of interlayer silylation of layered silicates with monofunctional silylating agents was shown above. An essential analysis for confirming silylation and calculating the degree of silylation is solid-state ^{29}Si NMR. Layered silicates are mainly composed of Q^3 ($\underline{\boldsymbol{Si}}(OSi)_3(OH/O^-)$) and Q^4 ($\underline{\boldsymbol{Si}}(OSi)_4$) units. The silylation reaction converts the Q^3 unit to the Q^4 unit, resulting in the appearance signals derived from attached silyl groups. Therefore, the degree of silylation can be calculated from the decrease in the integral intensity ratio. However, in silylation with monofunctional chlorosilanes, the Q^3 unit was reduced but not completely consumed.

Interlayer silylation of magadiite with bifunctional or trifunctional alkylchlorosilanes was performed by Ogawa *et al.*[98] Solid-state ^{29}Si NMR exhibited that the degree of silylation was nearly 100%, indicating that all SiOH/SiO$^-$ sites are capable of reacting. The fact that differences in functionality affect the degree of silylation means that the local structure of the SiOH/SiO$^-$ groups on the layer surfaces is critical. Therefore, it is essential to understand the crystal structure of layered silicates. The crystal structure of kanemite was identified using the Rietveld method by Gies *et al.,*[65] as described above. The existence of confronting SiOH/SiO$^-$ groups on the layer surface and the silicate flameworks composed of Q^3 units had been known. Shimojima *et al.*[99] silylated kanemite with mono-, di-, and tri-functional alkylchlorosilanes and precisely investigated its local structure. The structure of the attached alkylsilyl group is estimated by the ratio of the silylated Q^3 units to the silylating agent-derived units (M, D, and T). In the case of monochlorosilane, the degree of silylation was confirmed to be approximately 50%. In

the case of di- and tri-chlorosilane, two types of silylated structures were proposed (Fig. 1.7). Model A shows one silyl group is immobilized by bridging the confronting SiOH/SiO^- groups. Model B shows a dimerized two silyl group is immobilized on the confronting SiOH/SiO^- groups. For silylating agents with short alkyl chain lengths, the silylation inducing Model B occured. On the other hand, as the alkyl chain length increases, the silylation inducing Model A increased. Thus, the bridging of confronting SiOH/ SiO^- groups of existing layered silicates has enabled the synthesis of layered materials with a new silicate framework.

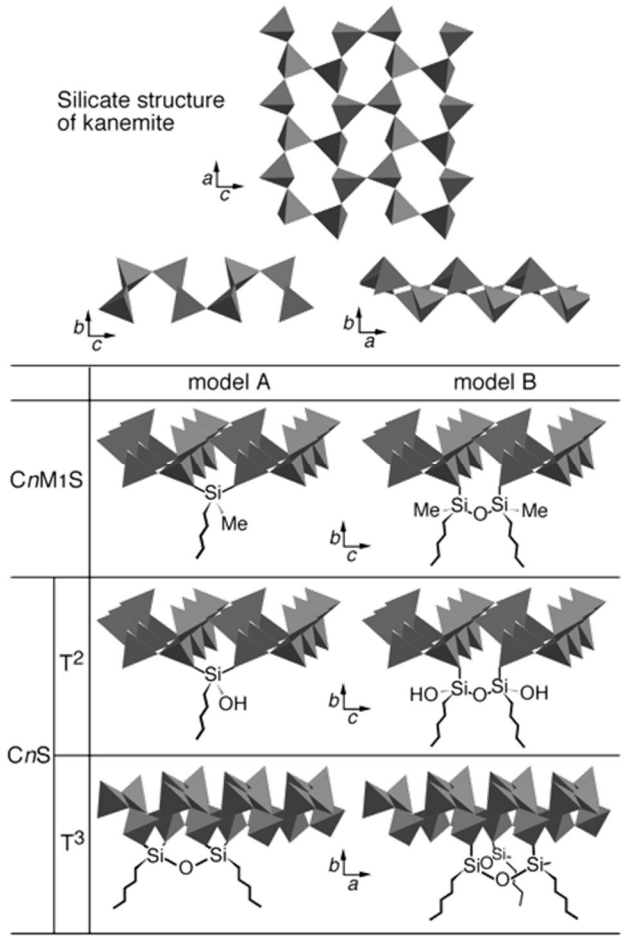

Fig. 1.7 Possible structural models of alkylsilylated kanemite.[99]
Reprinted with permission from Ref. 99. Copyright 2001 American Chemical Society.

Mochizuki *et al.* reported the interlayer silylation of layered octosilicate with chlorosilane possessing alkoxy groups.[100,101] Although alkoxysilanes can also react with surface silanol groups, alkoxysilylation occurs preferentially because chlorosilanes are more reactive. It was confirmed that silylation using alkoxychlorosilane ($(RO)_nSiCl_{4-n}$: n = 1 or 2, R = alkyl groups) bridged all the confronting $SiOH/SiO^-$ groups in layered octosilicate by single alkoxysilyl groups (dipodal or bidentate silylation). Thus, a structure with a regular arrangement of dipodal alkoxysilyl groups was constructed (Fig 1.8(A)). The alkoxysilyl group can be converted to a silanol group by hydrolysis. In the case of intercalation with DMSO after hydrolysis, a new two-dimensional crystalline framework that retains the layered structure is generated (Fig. 1.8(B)). On the other hand, the use of acetone instead of DMSO results in a novel 3D framework owing to interlayer condensation (Fig. 1.8(C)). Such synthesis of new crystalline silicate frameworks by alkoxysilylation was also performed for magadiite and kenyanite.[102] Asakura *et al.*[103,104] also confirmed that bidentate silylation is possible for RUB-51. RUB-51 has benzyl trimethylammonium cation in the interlayer from the beginning and few interlayer hydration water. Therefore, interlayer silylation of RUB-51 with tetrachlorosilane was performed by taking great care of humidity.[104] Dichlorosilyl groups were fixed on the layer surfaces because RUB-51 also has confronting $SiOH/SiO^-$ groups. After adding water and DMSO, novel 3D frameworks were synthesized by interlayer condensation through calcination (Fig. 1.8(D)).

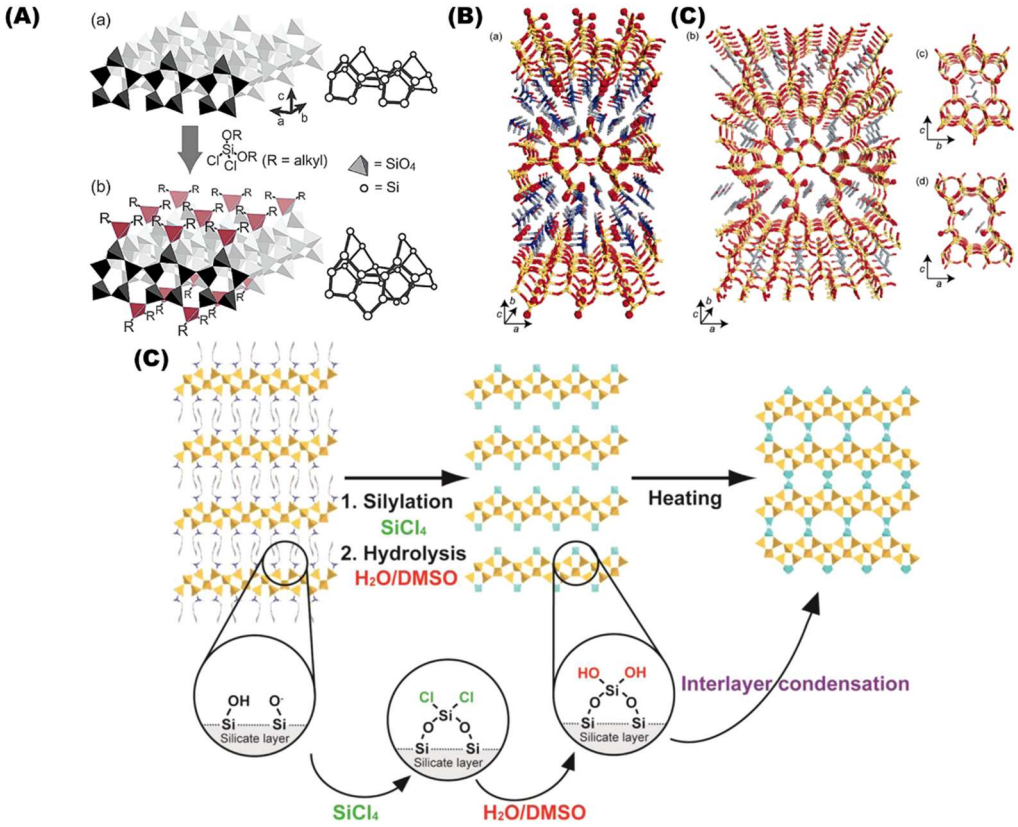

Fig. 1.8 (A) Dipodal silylation of layered octosilicate with dialkoxydichlorosilanes.[100] (B) Product obtained by hydrolysis and intercalation of DMSO after silylation with alkoxytrichlorosilanes.[101] (C) Product obtained by hydrolysis and intercalation of acetone after silylation with alkoxytrichlorosilanes.[101] (D) Interlayer condensation of dipodal-silylated RUB-51 with tetrachlorosilanes.[104]

In silylation with chlorosilane, the functional groups available for interlayer modification are limited to mainly alkyl and phenyl groups. Therefore, silanol groups as well as organic functional groups are effectively used in material design. Bidentate silylation with alkyltrichlorosilanes on the layer surface induces alkylsilanol groups through the hydrolysis of the chlorosilyl groups.[98] In addition, the interlayer ratio of alkyl groups to silanol groups can be controlled by reducing the amount of silylating agent

added, thereby adjusting the degree of silylation.[105,106] Thus, by controlling the balance of alkyl and silanol groups between the layers, high and selective alcohol adsorption capacity is achieved. Mochizuki *et al.*[107] cross-linked the layers of layered octosilicate via bidentate silylation with *p*-bis(trichlorosilyl)benzene or *p*-bis(dhichloromethylsilyl)-benzene. When the former silylating agent was used, the unreacted chlorosilyl groups were converted into silanol groups by hydrolysis, allowing the design of a space in which phenylene and silanol groups were regularly arranged. On the other hand, when the latter was used, a derivative in which the hydroxyl group was replaced with a methyl group was obtained. Comparing these samples, the sample using the former silylating agent was more selectively adsorbed with phenol.

1.3.1.2 Interlayer silylation of layered silicates with alkoxysilanes

Alkoxysilanes are silane compounds represented by $R^1_nSi(OR^2)_{4-n}$ (R^1 and R^2 = organic species; n = 0–3). Although the reactivity of alkoxysilanes is inferior to that of chlorosilanes, the diversity of organic functional groups that can be introduced into R^1 is significantly wider. In addition, the generation of alcohols rather than HCl during the reaction of alkoxysilanes with silanol groups is advantageous for the industrial utilization. Therefore, material design has been developed for the emergence of catalytic and selective adsorption ability by utilizing the functions of organic groups.[1]

(i) Material design through interlayer silylation using alkoxysilanes

Amino groups, basic organic functional groups, are immobilized on layered silicates and are mainly applied as solid base catalysts and CO_2 adsorbents. Kwon *et al.* modified the interlayer surfaces of kenyanite with aminopropyl groups using 3-

aminopropyltriethoxysilane (APTES).[108] Ide *et al.* designed a selective adsorbent for CO_2 by simultaneously immobilizing aminopropyl and octadecyl groups on the layer surface of magadiite (Fig. 1.9(A)).[109] CO_2 was selectively adsorbed from a mixture of N_2, CO_2, and H_2O gases because of coexisting hydrophobic long-chain alkyl and amino groups which serve as CO_2 adsorption sites between the layers. Tsunoji *et al.* used aminopropyl-modified HUS-2 and HUS-7 as catalysts for the transesterification of triacetin with methanol.[110] The interlayer expansion caused by the residual surfactant after silylation improved the accessibility of the substrate to the interlayer amino groups, resulting in higher catalytic activity.

Mercapto (thiol) groups are also typical functional groups immobilized on layered silicates and are expected to be used as ligands to metals or as acid sites through oxidation to sulfonic acid groups. Ide *et al.* modified layered octosilicate with 3-mercaptopropyltrimethoxysilane (MPTMS) to support Au nanoparticles in the interlayer (Fig. 1.9(B)).[111] For supporting Au nanoparticles, the loading and reduction processes of Au ions were performed separately to suppress excessive Au nanoparticle deposition. Thus, the material was designed to ensure the deposition of Au nanoparticles only in the interlayer spaces. Such a material design allows metal deposition only in the interlayer spaces, suggesting the fabrication of anisotropic metal nanostructures that take advantage of the limiting field between the layers. Baerdemaeker *et al.* cross-linked the layers of layered zeolites RUB-36 and RUB-39 with (3-mercaptopropyl)methyldimethoxysilane and converted the SH groups to SO_3H groups by subsequent hydrogen peroxide treatment.[112] It was used as a solid acid catalyst for the tetrahydropyranylation of alcohols.

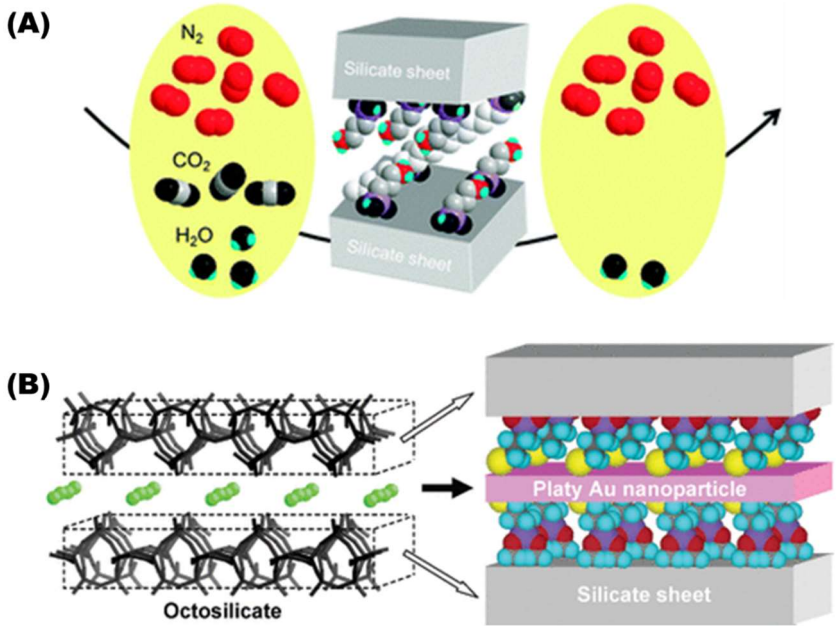

Fig. 1.9 Interlayer design using alkoxysilanes for (A) CO_2 adsorbent through the modification with amino groups[109] and (B) Au support through the modification with thiol groups[111].
Reprinted with permission from Ref. 109. Copyright 2013 Royal Society of Chemistry.
Reprinted with permission from Ref. 111. Copyright 2007 American Chemical Society.

Various other applications have been reported by immobilizing diverse functional groups to the interlayer surfaces of layered silicates. A list of silylation with alkoxysilanes, including those presented above, is shown in Table 1.1. Isoda *et al.* prepared layered silicate-polymer nanocomposites by polymerizing magadiite modified with 3-methacryloxypropyltrimethoxysilane with methyl methacrylate.[113] This nanocomposite can be fabricated more easily than conventional clay-polymer composites because of the immobilization of polymer initiators on the layer surface. Takahashi *et al.* converted the interlayer cation-exchange property to the anion-exchange property by silylating layered octosilicate with alkoxysilanes containing alkylimidazolium groups.[114] In the adsorption of various anions (Cl^-, Br^-, I^-, and NO_3^-), the selectivity of the adsorbed

anions changed with the length of the alkyl group. In addition, the adsorption behavior was quite distinct from layered double hydroxide (LDH), a common anion adsorbent. Furthermore, the dense immobilization of butylimidazolium groups, which have a high affinity for water, promoted hydration swelling and exfoliation of the layers. Nomi *et al.* silylated layered octosilicate with (4-diethoxyphosphorylphenyl)triethoxysilane and subsequently hydrolyzed ethoxyphosphoryl groups to immobilize phenylphosphonic acid.[115] This silylated derivative functioned as a catalyst for the acetalization of ketones due to its solid acid properties. Moreover, the intercalation of alkylamines via acid-base reactions enabled the exfoliation of layers in dichloromethane.

(ii) Possible mechanism of interlayer silylation with alkoxysilanes

Layered silicates naturally have SiO^- groups as well as SiOH groups on the interlayer surfaces. The nucleophilic attack of the SiOH groups on alkoxysilanes progresses with the generation of alcohols, while it is unlikely that the nucleophilic attack of the SiO^- groups leads to the release of unstable alkoxide anions. Therefore, Isoda *et al.* proposed the following reaction mechanism of interlayer silylation with alkoxysilane (Fig. 1.10).[113]

(1) Nucleophilic attack by the SiOH group on the alkoxysilane leads to forming a Si–O–Si bond.

(2) Subsequent reaction of the alcohol with another SiOH group generates water, which converts the SiO^- group to the SiOH group, resulting in the desorption of interlayer organic ammonium cation as hydroxide salt. The conversion of the SiO^- group is also caused by contaminated water in the reaction system.

(3) The generated SiOH group derived from the SiO^- group can react with the

alkoxysilane.

Thus, although water is involved in the interlayer silylation with alkoxysilanes, excess water causes hydrolytic condensation between alkoxysilanes, which prevents the introduction of well-defined silyl groups.

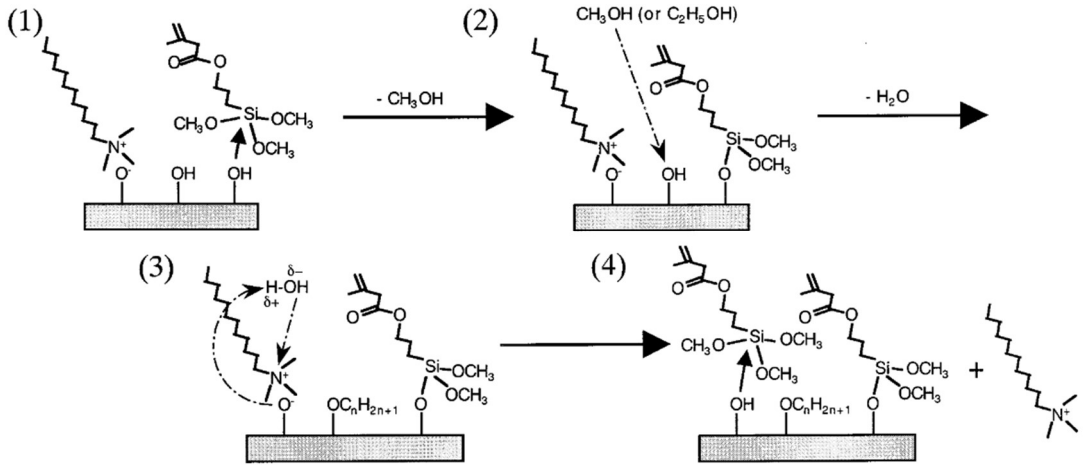

Fig. 1.10 Possible mechanism of interlayer silylation with alkoxysilanes.[113]
Reprinted with permission from Ref. 113. Copyright 2000 American Chemical Society.

(iii) The reactivity of alkoxysilanes with interlayer SiOH/SiO$^-$ groups

The research cases on the reactivity of alkoxysilanes are presented in this section. The degree of silylation using alkoxysilanes is often lower than that using chlorosilanes owing to the difference in their reactivity. A list of interlayer silylation with alkoxysilanes and the degrees of silylation is shown in Table 1.1. This table exhibited that the kinds of layered silicates and organic groups attached to alkoxysilanes affect the degree of silylation. Takahashi *et al.* silylated layered octosilicate, kanemite, and magadiite with 1-Butyl-3-(3-triethoxysilylpropyl)-4,5-dihydroimidazolium chloride.[114,116] The degrees of silylation were 82%, 55%, and 68%, respectively, which is considered to be attributed to the difference in the framework structure of layered silicates. The high-density silylation of layered octosilicate has also been confirmed by silylation with chlorosilane.[100] Ide *et*

al. achieved a high degree of silylation with MPTMS by concentrating a mixture of C_{12}TMA-exchanged magadiite, stoichiometric amount of silylating agents, and toluene.[117] This method may be one of the most efficient ways for dense immobilization using alkoxysilanes; however, MPTMS was densely grafted on the layer surfaces even with a general reflux method.[118] Moreover, a trend of lower degrees of silylation using alkoxysilanes with phenyl groups can be discerned from Table 1.1. Therefore, the properties of organic functional groups of alkoxysilanes are likely to affect the degree of interlayer silylation.

Table 1.1 List of silylation with alkoxysilanes and the degrees of silylation

Layered silicates	Silylating agents [a]	The degree of silylation	References
Layered octosilicate	4,4'-Bis(TES)biphenyl	33%	Ishii *et al.* (2005)[119]
	4,4'-Bis(TES)biphenyl 4,4'-Bis(methylDES)biphenyl 4,4'-Bis(dimethylES)biphenyl	18%~39%	Ishii *et al.* (2006)[120]
	p-AminophenylTMS	53%	Ishii *et al.* (2009)[121]
	3-MercaptopropylTMS	~100% [c]	Ide *et al.* (2009)[122]
	1-Butyl-3-(3-TESpropyl)-4,5-dihydroimidazolium chloride	82%	Takahashi *et al.* (2010)[114]
	1-Octyl-3-(3-TESpropyl)-4,5-dihydroimidazolium chloride	83%	Takahashi *et al.* (2010)[114]
	1,3-bis(3-(TES)propyl)urea	74%	Doustkhah *et al.* (2018)[123]
	(4-diethoxyphosphoryl-phenyl)TES	50%	Nomi *et al.* (2022)[115]
Magadiite	4,4'-Bis(TMSpropyl)viologen	~50%	Díaz *et al.* (2007)[124]
	3-MercaptopropylTMS	~100% [c]	Ide *et al.* (2007)[117]
	1-Butyl-3-(3-TESpropyl)-4,5-dihydroimidazolium chloride	68%	Takahashi *et al.* (2011)[116]
	3-ChloropropylTMS	29%	Vieira *et al.* (2018)[125]
	3-GlycidyloxypropylTMS	27%	Vieira *et al.* (2018)[125]

	3-GlycidyloxypropylTMS	10%	Vieira & Pastore (2018)[126]
	$(NH_2(C_2H_4)NH(C_2H_4)NH$-$C_3H_6)TMS$	8%	Vieira & Pastore (2018)[126]
kanemite	1-Butyl-3-(3-TESpropyl)-4,5-dihydroimidazolium chloride	55%	Takahashi *et al.* (2010)[114]
MWW	4,4'-Bis(TES)benzene	32%	Corma *et al.* (2010)[127]
HUS-2	3-AminopropylTES	63%	Tsunoji *et al.* (2014)[128]
	1,3-dimethyltetramethoxy-disiloxane	50%	Yang *et al.* (2018)[129]
HUS-7	3-MercaptopropylTES	90%	Jadav *et al.* (2022)[118]
SiO_2 [b]	3-AminopropylTES	59%	Doustkhah *et al.* (2023)[130]

[a] The terminal TMS and TES mean trimethoxysilane and triethoxysilane, respectively. ES, DES, TES in parentheses mean ethoxysilyl, diethoxysilyl, and triethoxysilyl, respectively. [b] In this report, the name used layered silicate was not described. A layered silicate with the following composition ($(Na[Si_{10}O_{20.3}(OH)_{1.7}])\cdot 4H_2O$[68]) is considered to have been used. [c] The values were calculated based on TG analysis, not ^{29}Si MAS NMR.

Park *et al.* reported that the addition of dodecylamine during the silylation of H-type magadiite with alkylalkoxysilanes increases the degree of silylation by expanding the interlayer and acting as a base catalyst.[131] However, a significant condensation between silylating agents was also confirmed on the basis of solid-state ^{29}Si NMR, suggesting hydrolysis and condensation of alkoxysilane because of water contamination, which cannot be achieved the well-defined local structure of the silyl groups.

Recently, Millot *et al.* reported that it is impossible to silylate the interlayer surfaces of layered octosilicate with APTES.[132] In this paper, the amount of silylating agent added to the reaction site ($SiOH/SiO^-$ group) was 1.4 equivalents, which was relatively small and was considered to cause no proceedings of the reaction. Many reports on the silylation of layered silicates using APTES and similar silylating agents have already been presented in this section, and excess amounts of silylating agents were added

in these reports. Therefore, this report is considered to reinforce the importance of excessive addition.

1.3.2 Esterification reactions

Esterification is a reaction to organically modify the layer surface via Si–O–R bonds by alkoxylation of the SiOH groups of layered silicic acid. Mercier *et al.* carried out esterification of NMF-intercalated H-type magadiite by refluxing in ethylene glycol.[133] Mitamura *et al.* esterified NMF-intercalated H-type magadiite by solvothermal treatment in various alcohols ($C_nH_{2n+1}OH$ (n = 1, 2, 4, 5, 6, 8, 9) and *tert*-butanol).[134] The degree of modification decreased with increasing alcohol length, and the basal spacing remained unchanged, suggesting that the alkyl chain was lying parallel to the surface. Kiba *et al.* confirmed the methoxylation of H-type octosilicate by solvothermal treatment in methanol and the appearance of hydrogen adsorption capacity.[135] As described above, alcohols are generally used for esterification, but ethylene sulfide can be used as another modifier. Ethylene sulfide is a three-membered ring molecule consisting of two C and one S, which undergoes nucleophilic attack from the silanol groups, resulting in the formation of 2-mercaptoethoxy groups on the layer surface.[136]

1.3.3 Modification with metal reagents

The surface SiOH/SiO^- group groups of layered silicates can also react with metal reagents. The modification of the dense and ordered silanol groups of layered silicates with metal species is expected to create single metal atom sites with a high loading amount and control of the local environment and arrangement of single metal sites. The single metal sites with these features are expected to be highly active catalysts

in various reactions.

Corma *et al.* modified the surface silanol groups of the layered zeolite ITQ-2, which is synthesized by delamination of pure siliceous MWW-type zeolite (ITQ-1), with Cp_2TiCl_2 (Cp = cyclopentadienyl).[137] The titanosilicate produced by calcination acted as a catalyst in the epoxidation of cyclohexene. Tsunoji *et al.* synthesized titanosilicates by intercalating $Ti(acac)_4$ (acac = acetylacetonate) into layered silicates HUS-2 and HUS-7 to catalyze the oxidation of cyclohexane and epoxidation of cyclohexene (Fig. 1.11).[138–140] These titanosilicates show high catalytic activity due to the high amount of Ti introduced, which is ascribable to the high silanol density of the layered silicates. However, externally precipitated TiO_2 species were also observed, and the local structure of Ti species were not elucidated sufficiently. Controlling accessibility to the interlayer is also an important factor in the catalytic application of layered silicates with immobilized metal species. The interlayer accessibility of HUS-2 modified with $Ti(acac)_4$ was improved by interlayer residual alkylammonium cations; however, it is gradually eliminated during the catalytic reaction (Fig. 1.11 (B)).

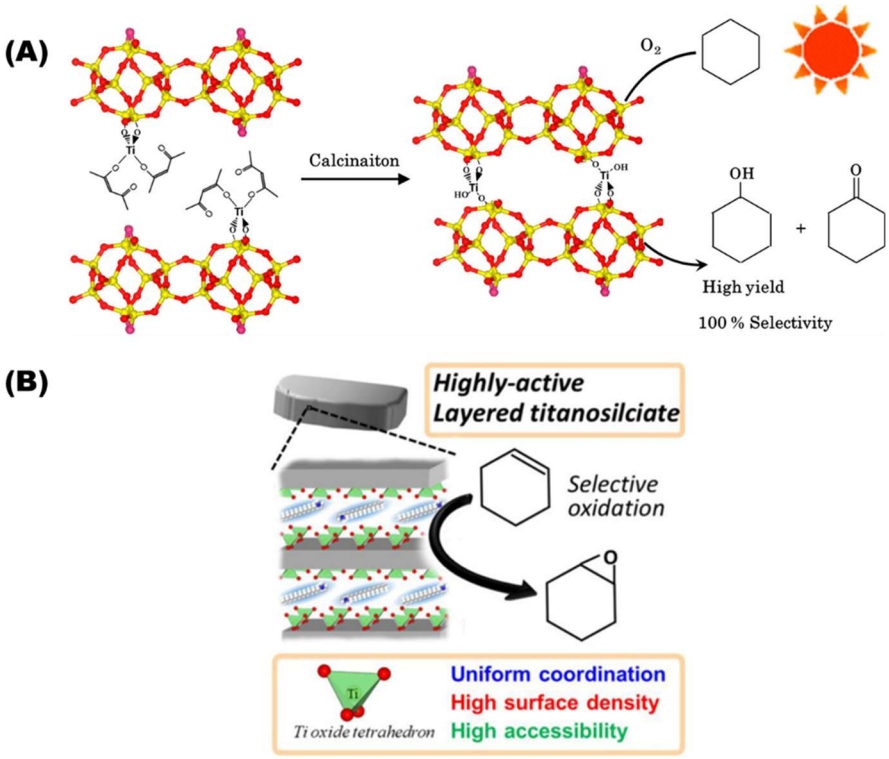

Fig. 1.11 (A) Interlayer modification of HUS-2 with Ti(acac)4 and catalytic reaction of the calcined products for oxidation of cyclohexane.[138] (B) Interlayer modification of HUS-7 with Ti(acac)4 and catalytic reaction of the interlayer-expanded products for epoxidation of cyclohexene.[139]
Reprinted with permission from Ref. 151. Copyright 2014 American Chemical Society.
Reprinted with permission from Ref. 152. Copyright 2018 John Wiley and Sons.

Regarding controlling the local environment, Grosso-Giordano *et al.* designed a titanium precursor for monopodal immobilization by capping three of the four reaction sites of Ti with a calix[4]arene (Fig. 1.12).[141] The calix[4]arene-Ti complexes grafted on the surface-defective silanol sites of MWW-type layered zeolite UCB-4. Monopodal grafting allows control of the coordination environment. Furthermore, immobilization to a specific silanol group of the crystalline support makes the local environment homogeneous. However, the use of defect sites limits the loading amounts and the control of the arrangement of Ti species.

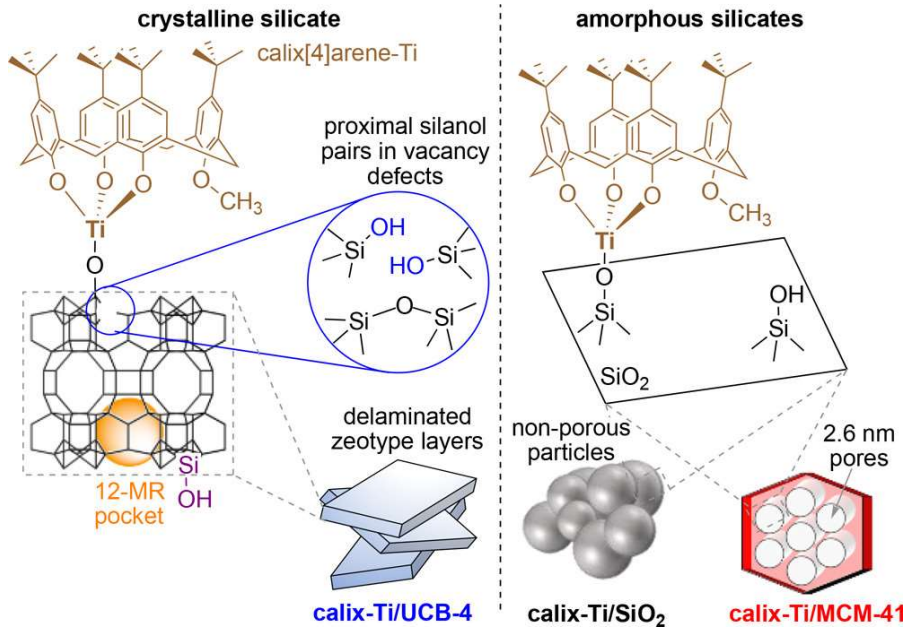

Fig. 1.12 Surface modification of UCB-4 (MWW-type 2D zeolite) with calix[4]arene-Ti and comparison with amorphous silica support.[141]
Reprinted with permission from Ref. 154. Copyright 2018 American Chemical Society.

1.3.4 Summary

The covalent immobilization of chemical species onto SiOH/SiO$^-$ groups on the layer surfaces of layered silicates has led to the development of various applications. Especially when highly reactive chlorosilanes are used, silyl groups are introduced into all of the regularly arranged SiOH/SiO$^-$ groups, inducing new crystalline frameworks and leading to selective adsorption ability. Such surface modification of layered silicates is one of the methods that maximize the unique feature of layered silicates, densely and regularly arranged reaction sites. On the other hand, alkoxysilanes with various functional groups could be utilized for the interlayer silylation of layered silicates, and a wide range of applications have been investigated. Although the degree of silylation is generally low, they vary depending on the structure of the layered silicates, the type of silylating agents, and the addition of catalysts. Therefore, the immobilization of dense and well-defined

silyl groups on the layer surfaces is challenging. Layered silicates have also been expected as promising supports for isolated metal species; however, high density and precise control of the local structure of the metal species have not been achieved.

1.4 Purpose and significance of this thesis

The purpose of this thesis is to present a methodology for immobilizing well-defined chemical species on the SiOH/SiO$^-$ groups of layered silicates using metal precursors and organoalkoxysilanes. Layered silicates are clearly distinct from other silica/silicate materials because the local structure of SiOH/SiO$^-$ groups on the layer surfaces are well-defined due to their framework crystallinity. By maximizing these superior features as a support, it is expected that chemical species with well-defined local structures can be immobilized at high density. Namely, new methods to precisely modify surface SiOH/SiO$^-$ groups without causing condensation between modifiers are required. The creation of well-defined isolated metal species on the interlayer surfaces would lead to attractive catalytic activity but has not been achieved due to challenges in controlling the reactivity of metal precursors. In addition, the development of efficient silylation using alkoxysilanes is desired because alkoxysilanes can possess diverse functional groups and do not produce HCl byproducts. However, factors affecting the degree of silylation are not well organized. It is difficult to overcome the low reactivity of alkoxysilanes and to immobilize silyl groups at high density while controlling their local structure. Therefore, progress in the development of methods for surface modification using metal reagents and alkoxysilanes will potentially lead to designing materials effectively utilizing the SiOH/SiO$^-$ groups of layered silicates.

1.5 References

1 N. Takahashi and K. Kuroda, *J. Mater. Chem.*, 2011, **21**, 14336–14353.

2 P. Zuber, Hydrous Layer Silicates, https://www.hls-database.com/contact/, (accessed 1 January 2024).

3 H. P. Eugster, *Science*, 1967, **157**, 1177–1180.

4 R. A. Sheppard and A. J. Gude, *Am. Mineral.*, 1970, **55**, 358–366.

5 Z. Johan and G. Maglione, *Bull. la Société française Minéralogie Cristallogr.*, 1972, **95**, 371–382.

6 L. McCulloch, *J. Am. Chem. Soc.*, 1952, **74**, 2453–2456.

7 R. K. Iler, *J. Colloid Sci.*, 1964, **19**, 648–657.

8 K. Beneke and G. Lagaly, *Am. Mineral.*, 1977, **62**, 763–771.

9 H. Annehed, L. Fäith and F. J. Lincoln, *Zeitschrift fur Krist. - New Cryst. Struct.*, 1982, **159**, 203–210.

10 K. Beneke and G. Lagaly, *Am. Mineral.*, 1983, **68**, 818–826.

11 A. K. Pant and D. W. J. Cruickshank, *Acta Crystallogr. Sect. B Struct. Crystallogr. Cryst. Chem.*, 1968, **24**, 13–19.

12 A. K. Pant, *Acta Crystallogr. Sect. B Struct. Crystallogr. Cryst. Chem.*, 1968, **24**, 1077–1083.

13 W. Hoffmann and H.-J. Scheel, *Zeitschrift für Krist.*, 1969, **129**, 396–404.

14 M. E. Fleet and G. S. Henderson, *J. Solid State Chem.*, 1995, **119**, 400–404.

15 K. Beneke, P. Thiesen and G. Lagaly, *Inorg. Chem.*, 1995, **34**, 900–907.

16 B. H. W. S. De Jong, H. T. J. Supèr, A. L. Spek, N. Veldman, G. Nachtegaal and J. C. Fischer, *Acta Crystallogr. Sect. B Struct. Sci.*, 1998, **54**, 568–577.

17 S. Rakić and V. Kahlenberg, *Eur. J. Mineral.*, 2001, **13**, 1215–1221.

18 S. Rakić, V. Kahlenberg and B. C. Schmidt, *Zeitschrift für Krist. - Cryst. Mater.*, 2003, **218**, 413–420.

19 D. Benbertal and A. Mosset, Journal of Solid State Chemistry, 1994, 108, 340–345.

20 K. Komura, T. Ikeda, A. Kawai, F. Mizukami and Y. Sugi, *Chem. Lett.*, 2007, **36**, 1248–1249.

21 I. Bull and J. B. Parise, *Acta Crystallogr. Sect. C Cryst. Struct. Commun.*, 2003, **59**, 1–10.

22 X. Wang, L. Liu, J. Huang and A. J. Jacobson, *J. Solid State Chem.*, 2004, **177**, 2499–2505.

23 F. Feng and K. J. Balkus, *J. Porous Mater.*, 2003, **10**, 5–15.

24 Z. Yuan, W. Tao, Z. Wang and W. Yang, *Appl. Clay Sci.*, 2019, **181**, 105231.

25 T. Iwasaki, T. Kuroda, S. Ichio, M. Satoh and T. Fujita, *Chem. Eng. Commun.*, 2006,

193, 69–76.

26 T. V. Whittam, US4397825A, 1983, 825.

27 A. J. Blake, K. R. Franklin and B. M. Lowe, *J. Chem. Soc. Dalt. Trans.*, 1988, 2513.

28 L. Schreyeck, P. Caullet, J. C. Mougenel, J. L. Guth and B. Marler, *Microporous Mater.*, 1996, **6**, 259–271.

29 A. Corma, V. Fornes, S. B. Pergher, T. L. M. Maesen and J. G. Buglass, *Nature*, 1998, **396**, 353–356.

30 M. J. Díaz-Cabañas, M. A. Camblor, Z. Liu, T. Ohsuna and O. Terasaki, *J. Mater. Chem.*, 2002, **12**, 249–257.

31 T. Ikeda, Y. Akiyama, Y. Oumi, A. Kawai and F. Mizukami, *Angew. Chemie Int. Ed.*, 2004, **43**, 4892–4896.

32 R. Millini, L. C. Carluccio, A. Carati, G. Bellussi, C. Perego, G. Cruciani and S. Zanardi, *Microporous Mesoporous Mater.*, 2004, **74**, 59–71.

33 I. Ogino, M. M. Nigra, S.-J. Hwang, J.-M. Ha, T. Rea, S. I. Zones and A. Katz, *J. Am. Chem. Soc.*, 2011, **133**, 3288–3291.

34 I. Ogino, E. A. Eilertsen, S. J. Hwang, T. Rea, D. Xie, X. Ouyang, S. I. Zones and A. Katz, *Chem. Mater.*, 2013, **25**, 1502–1509.

35 M. E. Leonowicz, J. A. Lawton, S. L. Lawton and M. K. Rubin, *Science*, 1994, **264**, 1910–1913.

36 A. Burton, R. J. Accardi, R. F. Lobo, M. Falcioni and M. W. Deem, *Chem. Mater.*, 2000, **12**, 2936–2942.

37 D. L. Dorset and G. J. Kennedy, *J. Phys. Chem. B*, 2004, **108**, 15216–15222.

38 L. D. Rollmann, J. L. Schlenker, S. L. Lawton, C. L. Kennedy and G. J. Kennedy, *Microporous Mesoporous Mater.*, 2002, **53**, 179–193.

39 B. Marler, Y. Krysiak, U. Kolb, C. Grafweg and H. Gies, *Microporous Mesoporous Mater.*, 2020, **296**, 109981.

40 U. Oberhagemann, P. Bayat, B. Marler, H. Gies and J. Rius, *Angew. Chemie Int. Ed. English*, 1996, **35**, 2869–2872.

41 B. Marler, Y. Wang, J. Song and H. Gies, *Dalton Trans.*, 2014, **43**, 10396–10416.

42 H. Gies, U. Müller, B. Yilmaz, M. Feyen, T. Tatsumi, H. Imai, H. Zhang, B. Xie, F. S. Xiao, X. Bao, W. Zhang, T. De Baerdemaeker and D. De Vos, *Chem. Mater.*, 2012, **24**, 1536–1545.

43 Y. X. Wang, H. Gies and J. H. Lin, *Chem. Mater.*, 2007, **19**, 4181–4188.

44 Z. Li, B. Marler and H. Gies, *Chem. Mater.*, 2008, **20**, 1896–1901.

45 B. Marler, Z. Li, G. Wang and H. Gies, *Acta Crystallogr. Sect. A*, 2011, **67**, 650.

46 B. Marler, A. Grünewald-Lüke, S. Grabowski and H. Gies, *Zeitschrift für Krist.*, 2012,

227, 427–437.

47 T. Ikeda, Y. Oumi, K. Honda, T. Sano, K. Momma and F. Izumi, *Inorg. Chem.*, 2011, **50**, 2294–2301.

48 N. Tsunoji, T. Ikeda, Y. Ide, M. Sadakane and T. Sano, *J. Mater. Chem.*, 2012, **22**, 13682.

49 N. Tsunoji, M. Fukuda, K. Yoshida, Y. Sasaki, T. Ikeda, Y. Ide, M. Sadakane and T. Sano, *J. Mater. Chem. A*, 2013, **1**, 9680–9688.

50 N. Tsunoji, T. Ikeda, M. Sadakane and T. Sano, *J. Mater. Chem. A*, 2014, **2**, 3372–3380.

51 G. Pál-Borbély and A. Auroux, in *Studies in Surface Science and Catalysis*, 1995, vol. 94, pp. 55–62.

52 W. Schwieger, K. Pohl, U. Brenn, C. A. Fyfe, H. Grondey, G. Fu and G. T. Kokotailo, in *Studies in Surface Science and Catalysis*, 1995, vol. 94, pp. 47–54.

53 G. B. Superti, E. C. Oliveira, H. O. Pastore, A. Bordo, C. Bisio and L. Marchese, *Chem. Mater.*, 2007, **19**, 4300–4315.

54 H. M. Moura, F. A. Bonk, R. C. G. Vinhas, R. Landers and H. O. Pastore, *CrystEngComm*, 2011, **13**, 5428.

55 S. Inagaki, Y. Yamada and Y. Fukushima, *Stud. Surf. Sci. Catal.*, 1997, **105**, 109–116.

56 Q. Kan, V. Fornés, F. Rey and A. Corma, *J. Mater. Chem.*, 2000, **10**, 993–1000.

57 W. Supronowicz and F. Roessner, *Clays Clay Miner.*, 2011, **59**, 95–105.

58 F. S. O. Ramos and H. O. Pastore, *Dalton Trans.*, 2017, **46**, 11728–11737.

59 T. Kimura, M. Suzuki, T. Ikeda, K. Kato, M. Maeda and S. Tomura, *Microporous Mesoporous Mater.*, 2006, **95**, 146–153.

60 W. Supronowicz, F. Roessner, W. Schwieger, M. Meilikhov and D. Esken, *Clays Clay Miner.*, 2012, **60**, 254–264.

61 M. Morita, Y. Horiuchi, M. Matsuoka and M. Ogawa, *Cryst. Growth Des.*, 2022, **22**, 1638–1644.

62 T. G. Dos Santos, A. O. S. Da Silva and S. M. Plentz Meneghetti, *Catal. Sci. Technol.*, 2020, **10**, 6111–6115.

63 S. Vortmann, J. Rius, S. Siegmann and H. Gies, *J. Phys. Chem. B*, 1997, **101**, 1292–1297.

64 I. Wolf, H. Gies and C. A. Fyfe, *J. Phys. Chem. B*, 1999, **103**, 5933–5938.

65 S. Vortmann, J. Rius, B. Marler and H. Gies, *Eur. J. Mineral.*, 1999, **11**, 125–134.

66 T. J. Pinnavaia, I. D. Johnson and M. Lipsicas, *J. Solid State Chem.*, 1986, **63**, 118–121.

67 J. M. Garcés, S. C. Rocke, C. E. Crowder and D. L. Hasha, *Clays Clay Miner.*, 1988, **36**, 409–418.

68 Y. Ide, S. Tominaka, H. Kono, R. Ram, A. Machida and N. Tsunoji, *Chem. Sci.*, 2018, **9**,

8637–8643.

69 Y. Krysiak, M. Maslyk, B. N. Silva, S. Plana-Ruiz, H. M. Moura, E. O. Munsignatti, V. S. Vaiss, U. Kolb, W. Tremel, L. Palatinus, A. A. Leitão, B. Marler and H. O. Pastore, *Chem. Mater.*, 2021, **33**, 3207–3219.

70 B. Marler, Y. Krysiak, I. Grosskreuz, H. Gies and U. Kolb, *Am. Mineral.*, 2022, **107**, 2101–2110.

71 B. Marler, I. Grosskreuz and H. Gies, *J. Solid State Chem.*, 2021, **300**, 122215.

72 G. Lagaly, K. Beneke and A. Weiss, *Am. Mineral.*, 1975, **60**, 642–649.

73 G. Lagaly, K. Beneke, P. Dietz and A. Weiss, *Angew. Chemie - Int. Ed.*, 1974, **13**, 819–821.

74 K. Beneke and G. Lagaly, *Am. Mineral.*, 1989, **74**, 224–229.

75 S. Osada, A. Iribe and K. Kuroda, *Chem. Lett.*, 2013, **42**, 80–82.

76 M. Dakhchoune, L. F. Villalobos, R. Semino, L. Liu, M. Rezaei, P. Schouwink, C. E. Avalos, P. Baade, V. Wood, Y. Han, M. Ceriotti and K. V. Agrawal, *Nat. Mater.*, 2021, **20**, 362–369.

77 K. Awaya, K. Sekiguchi, H. Kitagawa, S. Yamada and S. Ida, *Chem. Commun.*, 2021, **57**, 6304–6307.

78 P. Loch, D. Schuchardt, G. Algara-Siller, P. Markus, K. Ottermann, S. Rosenfeldt, T. Lunkenbein, W. Schwieger, G. Papastavrou and J. Breu, *Sci. Adv.*, 2022, **8**, eabn9084.

79 Y. Asakura, M. Sugihara, T. Hirohashi, A. Torimoto, T. Matsumoto, M. Koike, Y. Kuroda, H. Wada, A. Shimojima and K. Kuroda, *Nanoscale*, 2019, **11**, 12924–12931.

80 T. Yanagisawa, T. Shimizu, K. Kuroda and C. Kato, *Bull. Chem. Soc. Jpn.*, 1990, **63**, 988–992.

81 S. Inagaki, Y. Fukushima and K. Kuroda, *J. Chem. Soc. Chem. Commun.*, 1993, 680–682.

82 S. Inagaki, A. Koiwai, N. Suzuki, Y. Fukushima and K. Kuroda, *Bull. Chem. Soc. Jpn.*, 1996, **69**, 1449–1457.

83 T. Shigeno, M. Nagao, T. Kimura and K. Kuroda, *Langmuir*, 2002, **18**, 8102–8107.

84 H. Tamura, D. Mochizuki, T. Kimura and K. Kuroda, *Chem. Lett.*, 2007, **36**, 444–445.

85 M. Kato, T. Shigeno, T. Kimura and K. Kuroda, *Chem. Mater.*, 2004, **16**, 3224–3230.

86 M. Kato, T. Shigeno, T. Kimura and K. Kuroda, *Chem. Mater.*, 2005, **17**, 6416–6421.

87 R. García, I. Díaz, C. Márquez-Álvarez and J. Pérez-Pariente, *Chem. Mater.*, 2006, **18**, 2283–2292.

88 N. Alam and R. Mokaya, *J. Mater. Chem.*, 2008, **18**, 1383.

89 T. Kimura, H. Tamura, M. Tezuka, D. Mochizuki, T. Shigeno, T. Ohsuna and K. Kuroda, *J. Am. Chem. Soc.*, 2008, **130**, 201–209.

90 T. Kimura and K. Kuroda, *Adv. Funct. Mater.*, 2009, **19**, 511–527.

91 E. Ruiz-Hitzky and J. M. Rojo, *Nature*, 1980, **287**, 28–30.

92 E. Ruiz-Hitzky, J. M. Rojo and G. Lagaly, *Colloid Polym. Sci.*, 1985, **263**, 1025–1030.

93 T. Yanagisawa, K. Kuroda and C. Kato, *React. Solids*, 1988, **5**, 167–175.

94 T. Yanagisawa, K. Kuroda and C. Kato, *Bull. Chem. Soc. Jpn.*, 1988, **61**, 3743–3745.

95 T. Yanagisawa, H. Masatoshi, K. Kuroda and C. Kato, *Solid State Ionics*, 1990, **42**, 15–19.

96 M. Ogawa, *Chem. Mater.*, 1998, **10**, 3787–3789.

97 S. Okutomo, K. Kuroda and M. Ogawa, *Appl. Clay Sci.*, 1999, **15**, 253–264.

98 M. Ogawa, S. Okutomo and K. Kuroda, *J. Am. Chem. Soc.*, 1998, **120**, 7361–7362.

99 A. Shimojima, D. Mochizuki and K. Kuroda, *Chem. Mater.*, 2001, **13**, 3603–3609.

100 D. Mochizuki, A. Shimojima and K. Kuroda, *J. Am. Chem. Soc.*, 2002, **124**, 12082–12083.

101 D. Mochizuki, A. Shimojima, T. Imagawa and K. Kuroda, *J. Am. Chem. Soc.*, 2005, **127**, 7183–7191.

102 D. Mochizuki and K. Kuroda, *New J. Chem.*, 2006, **30**, 277–284.

103 Y. Asakura, Y. Matsuo, N. Takahashi and K. Kuroda, *Bull. Chem. Soc. Jpn.*, 2011, **84**, 968–975.

104 Y. Asakura, Y. Sakamoto and K. Kuroda, *Chem. Mater.*, 2014, **26**, 3796–3803.

105 I. Fujita, K. Kuroda and M. Ogawa, *Chem. Mater.*, 2003, **15**, 3134–3141.

106 I. Fujita, K. Kuroda and M. Ogawa, *Chem. Mater.*, 2005, **17**, 3717–3722.

107 D. Mochizuki, S. Kowata and K. Kuroda, *Chem. Mater.*, 2006, **18**, 5223–5229.

108 K.-W. Park, S.-Y. Jeong and O.-Y. Kwon, *Appl. Clay Sci.*, 2004, **27**, 21–27.

109 Y. Ide, N. Kagawa, M. Sadakane and T. Sano, *Chem. Commun.*, 2013, **49**, 9027–9029.

110 N. Tsunoji, M. Bandyopadhyay, Y. Yagenji, H. Nishida, M. Sadakane and T. Sano, *Dalton Trans.*, 2017, **46**, 7441–7450.

111 Y. Ide, A. Fukuoka and M. Ogawa, *Chem. Mater.*, 2007, **19**, 964–966.

112 T. De Baerdemaeker, W. Vandebroeck, H. Gies, B. Yilmaz, U. Müller, M. Feyen and D. De Vos, *Catal. Today*, 2014, **235**, 169–175.

113 K. Isoda, K. Kuroda and M. Ogawa, *Chem. Mater.*, 2000, **12**, 1702–1707.

114 N. Takahashi, H. Hata and K. Kuroda, *Chem. Mater.*, 2010, **22**, 3340–3348.

115 M. Nomi, M. Morita, A. Kondo and K. Maeda, *Inorg. Chem.*, 2022, **61**, 5255–5261.

116 N. Takahashi, H. Hata and K. Kuroda, *Chem. Mater.*, 2011, **23**, 266–273.

117 Y. Ide and M. Ogawa, *Bull. Chem. Soc. Jpn.*, 2007, **80**, 1624–1629.

118 D. Jadav, P. Shukla, R. Bandyopadhyay, P. J. Sarma, R. C. Deka, R. Kumar, S. Das, N. Tsunoji and M. Bandyopadhyay, *New J. Chem.*, 2022, **46**, 9418–9431.

119 R. Ishii and Y. Shinohara, *J. Mater. Chem.*, 2005, **15**, 551–553.

120 R. Ishii, T. Ikeda, T. Itoh, T. Ebina, T. Yokoyama, T. Hanaoka and F. Mizukami, *J. Mater. Chem.*, 2006, **16**, 4035–4043.

121 R. Ishii, T. Ikeda and F. Mizukami, *J. Colloid Interface Sci.*, 2009, **331**, 417–424.

122 Y. Ide, G. Ozaki and M. Ogawa, *Langmuir*, 2009, **25**, 5276–5281.

123 E. Doustkhah, S. Rostamnia, N. Tsunoji, J. Henzie, T. Takei, Y. Yamauchi and Y. Ide, *Chem. Commun.*, 2018, **54**, 4402–4405.

124 U. Díaz, A. Cantín and A. Corma, *Chem. Mater.*, 2007, **19**, 3686–3693.

125 R. B. Vieira, P. A. S. Moura, E. Vilarrasa-García, D. C. S. Azevedo and H. O. Pastore, *J. CO2 Util.*, 2018, **23**, 29–41.

126 R. B. Vieira and H. O. Pastore, *Dalton Trans.*, 2018, **47**, 3102–3111.

127 A. Corma, U. Díaz, T. García, G. Sastre and A. Velty, *J. Am. Chem. Soc.*, 2010, **132**, 15011–15021.

128 N. Tsunoji, K. Takahashi, M. Sadakane and T. Sano, *Bull. Chem. Soc. Jpn.*, 2014, **87**, 1379–1385.

129 B. Yang, J.-G. Jiang, H. Xu, H. Wu and P. Wu, *Chinese J. Chem.*, 2018, **36**, 227–232.

130 E. Doustkhah, N. Tsunoji, M. H. N. Assadi and Y. Ide, *Adv. Mater. Interfaces*, 2023, **10**, 1–9.

131 K. Park, J. Hwa, S. Kim and O. Kwon, *Appl. Clay Sci.*, 2009, **46**, 251–254.

132 Y. Millot, A. Hervier, J. Ayari, N. Hmili, J. Blanchard and S. Boujday, *J. Am. Chem. Soc.*, 2023, **145**, 6671–6681.

133 L. Mercier, G. A. Facey and C. Detellier, *J. Chem. Soc. Chem. Commun.*, 1994, 2111.

134 Y. Mitamura, Y. Komori, S. Hayashi, Y. Sugahara and K. Kuroda, *Chem. Mater.*, 2001, **13**, 3747–3753.

135 S. Kiba, T. Itagaki, T. Nakato and K. Kuroda, *J. Mater. Chem.*, 2010, **20**, 3202–3210.

136 M. M. de Oliveira, M. M. Fernandes, M. G. Fonseca, E. C. da Silva Filho, A. G. de Souza, F. Gaslain and M. Jaber, *Microporous Mesoporous Mater.*, 2014, **196**, 292–299.

137 A. Corma, U. Díaz, V. Fornés, J. L. Jordá, M. Domine and F. Rey, *Chem. Commun.*, 1999, 779–780.

138 N. Tsunoji, Y. Ide, Y. Yagenji, M. Sadakane and T. Sano, *ACS Appl. Mater. Interfaces*, 2014, **6**, 4616–4621.

139 N. Tsunoji, M. V. Opanasenko, M. Kubů, J. Čejka, H. Nishida, S. Hayakawa, Y. Ide, M. Sadakane and T. Sano, *ChemCatChem*, 2018, **10**, 2536–2540.

140 N. Tsunoji, H. Nishida, Y. Ide, K. Komaguchi, S. Hayakawa, Y. Yagenji, M. Sadakane and T. Sano, *ACS Catal.*, 2019, **9**, 5742–5751.

141 N. A. Grosso-Giordano, C. Schroeder, A. Okrut, A. Solovyov, C. Schöttle, W. Chassé,

N. Marinković, H. Koller, S. I. Zones and A. Katz, *J. Am. Chem. Soc.*, 2018, **140**, 4956–4960.

Chapter 2

Immobilization of Isolated Dimethyltin Species on Crystalline Silicates through Surface Modification of Layered Octosilicate

The major part of this chapter was adapted with permission from M. Yatomi, T. Hikino, S. Yamazoe, K. Kuroda, A. Shimojima, "Immobilization of Isolated Dimethyltin Species on Crystalline Silicates through Surface Modification of Layered Octosilicate", *Dalton Trans.*, **2023**, *52*, 18158.

2.1 Introduction

Single metal atoms immobilized on silica surfaces are used as highly active heterogeneous catalysts for various reactions.[1–5] Precise control of the loading amount, coordination environment, and location of metal species is crucial for improving catalytic activity and understanding the catalytic mechanisms.[4,5] To efficiently utilize isolated metal sites, metal species are generally immobilized on the surface silanols of amorphous silica with a high surface area (e.g., silica gel, fumed silica, and mesoporous silica) or silanol nests in zeolites.[6,7] However, there are challenges with these silica-based supports in terms of controlling the local environment and increasing the amount of metal species. The monopodal metal species can be generated using isolated silanol groups formed by dehydroxylating amorphous silica at high temperatures under vacuum.[3,8,9] The dipodal metal species are prepared by immobilizing a metal complex bearing bidentate disiloxane ligands.[10] However, amorphous silica has no crystallinity, making it difficult to control the local environment and distribution of the metal species. Zeolites have crystalline structures; however, silanol nests are defect sites obtained by acid treatment to remove Al and B atoms, which limits the amount of introduced metal species to a few wt%.[6,7,11,12] In addition, micropores in the rigid framework of zeolites limit the accessibility of substrates.[13]

Layered silicates (also called layered polysilicates) consist of 2D nanosheets with a crystalline silicate framework alternately stacked with interlayer-exchangeable cations. Silanol (Si–OH) and silanolate ($Si–O^-$) groups are arranged regularly and densely on the surfaces of the layers. The modification of these groups enables the design of functional 2D spaces with regularly arranged chemical species.[14,15] Surface modification and interlayer pillaring by immobilizing organosilyl groups and metal species were

investigated for applications in catalysis[16,17] and adsorption.[18–20] For immobilizing bulky species between the layers, it is effective to expand the interlayer spaces by exchanging the interlayer alkali metal cations with long-chain alkylammonium cations.[21] Layered silicates such as kanemite, layered octosilicate, and RUB-51, which have confronting SiOH/SiO^- groups on the layer surfaces, can be grafted with chlorosilanes (R_nSiCl_{4-n}: n = 0–2, and R'$OSiCl_3$, where R and R' are alkyl groups), producing functional materials with crystalline frameworks with dense and regular arrangements of dipodal silyl groups.[20,22–24] Several reports are available on interlayer swelling[25,26] and exfoliation of the layers,[27,28] enabling the control of substrate accessibility to the interlayer surfaces. Thus, layered silicates have the potential to serve as excellent supports for creating well-defined single metal sites, overcoming the aforementioned challenges of amorphous silica and zeolite supports.

The formation of Si–O–M (M = metal atom) bonds on the surface of layered silicates was reported by Tsunoji *et al.* for grafting $Ti^{IV}(acac)_4$ (acac = acetylacetonate) onto layered silicates HUS-2[16] and HUS-7.[29,30] These studies showed that the catalytic activity was improved by high loading amounts of Ti and the expansion of interlayer spaces. However, the local environment of Ti(IV) was not sufficiently elucidated. Layered zeolites, which are another type of 2D crystalline silicates, were also used as supports for metal species.[31,32] Grosso-Giordano *et al.* immobilized Ti(IV) on the surface defect sites of a delaminated MWW-type layered zeolite (UCB-4) and analyzed the local environment of Ti.[32] The precise control of the coordination state of the Ti(IV) species and the environment of the surrounding silanol groups resulted in higher catalytic activity compared to metal species supported on amorphous silica. However, the amount of Ti

introduced was extremely small because of the limited amount of defect sites, which made it difficult to control the arrangement of metal sites.

To precisely control the immobilization of metal species on layered silicates via Si–O–M bonds, controlling the number of reaction sites in the metal precursors is essential. When metal alkoxides and chlorides are used as precursors, limiting the number of alkoxy or chloro groups is crucial to prevent the unwanted formation of M–O–M bonds. Alkyltin chlorides (R_nSnCl_{4-n}) were focused as a metal precursor because the number of highly reactive Sn–Cl bonds can be easily controlled by introducing relatively stable Sn–C bonds.[33–36] This feature of Sn is clearly distinctive from the organometallic compounds of transition metals such as Ti and Zr, where M–C bonds are highly reactive.[37,38] Recently, Sn-modified silica has attracted considerable attention as Lewis acid catalysts. Tetrachlorotin ($SnCl_4$) reacts with the silanol nest of zeolites to form 4-coordinated isolated SnO_4, which acts as a Lewis acid site.[6,11,12,39] Organotin(IV) compounds also exhibit Lewis acidity by controlling the coordination number and introducing electron-withdrawing functional groups.[40–43] Hence, the introduction of alkyltin species into silicate frameworks via Si–O–Sn bonds is a promising approach for their use as catalysts. The immobilization of alkyltin species on zeolites and amorphous silica was reported in the literature;[33–35,44] however, these silica supports have the aforementioned limitations that hamper the high density and regular immobilization of Sn species.

In this study, the successful immobilization of well-defined and isolated dimethyltin species on the interlayer surfaces of layered octosilicates (Scheme 2.1) is demonstrated. Na-type layered octosilicate (RUB-18, Ilerite, $Na_8Si_{32}O_{64}(OH)_8 \cdot 32H_2O$, named as Na-Oct) has a high density of confronting $SiOH/SiO^-$ groups (3.4 OH/nm^2) on the layer surface (Scheme 2.1 (a) and (b)). The two Sn–Cl groups of dimethyltin

dichloride are expected to react with the confronting SiOH/SiO^- groups, resulting in bidentate immobilization of the dimethyltin groups. Tri- or tetra-chlorotin compounds are not suitable because Sn–Cl groups remain on the layers even after bidentate immobilization, which may induce condensation with other Sn species in the presence of water. The degree of dimethyltin modification was tailored by varying the amount of Me_2SnCl_2 added to the reaction. Moreover, comparisons were made between these tin-modified samples and those prepared using the silane analogue, dichlorodimethylsilane, to discuss the differences in the interlayer environments. The local environment around the grafted dimethyltin groups was investigated by UV–Vis spectroscopy, X-ray photoelectron spectroscopy (XPS), and X-ray absorption fine structure (XAFS) analysis to identify the state of the immobilized dimethyltin on the layered silicates.

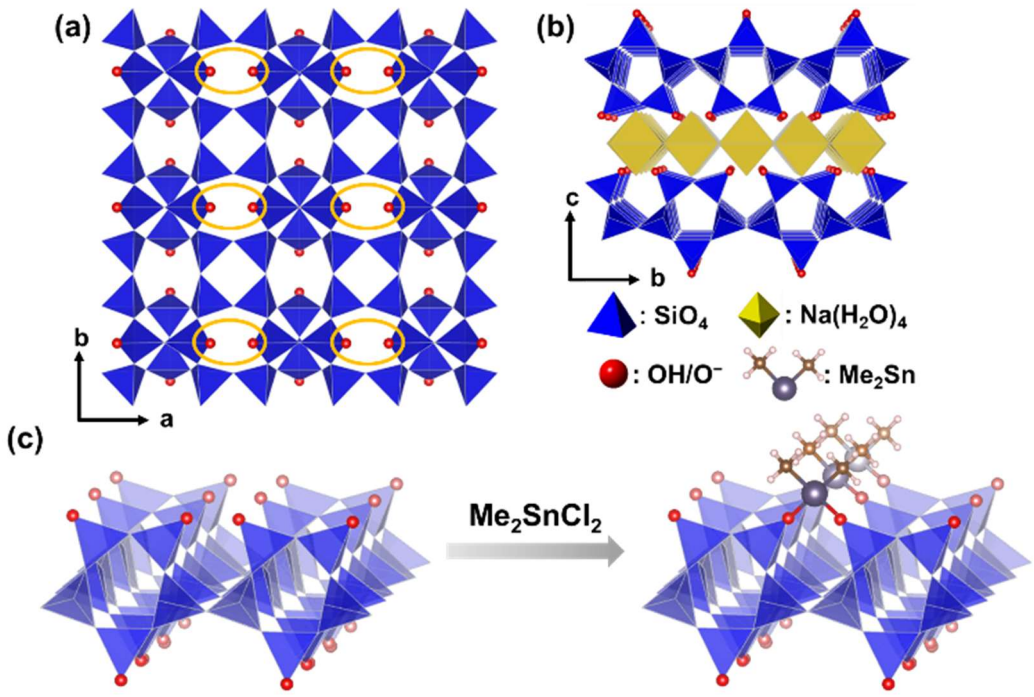

Scheme 2.1 (a)(b) Structural models of Na-type layered octosilicate and (c) bidentate immobilization of dimethyltin dichloride on the surface of octosilicate.

2.2 Experimental Methods

2.2.1 Materials

SiO_2 (fumed silica (S5130)) was purchased from Sigma-Aldrich. NaOH (97%), SnO (97%), SnO_2 (98%), dehydrated pyridine (99.5%), super dehydrated *N,N*-dimethylformamide (DMF, 99.5%), super dehydrated dichloromethane (DCM, 99.5%), dichloromethane (99.5%), and 6 M HCl solution were purchased from FUJIFILM Wako Pure Chemical Corp. Hexadecyltrimethylammonium chloride (C_{16}TMACl, 95% purity), dimethyltin dichloride (Me_2SnCl_2, 99%), dichlorodimethylsilane (Me_2SiCl_2, 98%), and dimethyltin oxide (DMTO, 95%) were purchased from Tokyo Chemical Industry. Co., Ltd. (TCI). Acetone (99.0%) and hexane (99.0%) were purchased from Kanto Chemical Co., Inc. All the reagents were used without further purification.

2.2.2 Preparation of layered Na-octosilicate and ion-exchange with C_{16}TMACl

Na-Oct and hexadecyltrimethylammonium ion-exchanged octosilicate (C_{16}TMA-Oct) were synthesized following the previous reports.[45,46] Fumed silica, NaOH, and deionized water were mixed at a molar ratio of 4:1:25.8 in a Teflon beaker, and the mixture was aged for 1 h. Hydrothermal treatment was conducted in a Teflon-sealed autoclave at 100 °C for 4 w. The product was washed with deionized water and air-dried at 45 °C to obtain Na-Oct. Na-Oct (1.5 g) was dispersed in 100 mL of 0.1 M aqueous solution of C_{16}TMACl and stirred at room temperature for 24 h. After centrifuging the suspension, the precipitate was washed twice with deionized water. Finally, the product was vacuum-dried at room temperature to obtain C_{16}TMA-Oct.

2.2.3 Grafting of dimethyltin dichloride on C_{16}TMA-Oct

C_{16}TMA-Oct (0.2 g) was dried in a Schlenk flask under vacuum heating at 120 °C for 3 h. After cooling to 100 °C and introducing dried N_2, DMF (10 mL) and Me_2SnCl_2 were added, and the mixture was stirred at 100 °C for 2 d. The reaction was performed without adding a base such as pyridine to trap HCl. Me_2SnCl_2 was added at 0.1, 0.25, 0.5, and 10 equivalents (8, 20, 41, and 811 mg, respectively) against a pair of the reaction sites ($SiOH/SiO^-$) on the octosilicate surface. The products were separated by centrifugation (5000 rpm, 5 min), washed three times with acetone, and dried overnight under reduced pressure. The samples were named Me_2Sn-Oct_*X* (*X* = 0.1, 0.25, 0.5, and 10), where *X* represents the equivalents of Me_2SnCl_2.

2.2.4 Silylation of C_{16}TMA-Oct with Me_2SiCl_2

C_{16}TMA-Oct (0.2 g) in a Schlenk flask was dried by vacuum heating at 120 °C for 3 h. Dichloromethane (10 mL), pyridine (5 mL), and Me_2SiCl_2 (0.44 mL) were added under the N_2 atmosphere, and the mixture was stirred at room temperature for 1 d under a nitrogen atmosphere. The silylating agent was 10 equivalents each for the pair of reaction sites ($SiOH/SiO^-$) on the octosilicate surface. The product was separated by centrifugation (5000 rpm, 5 min), washed three times with dichloromethane, and dried overnight under reduced pressure. This sample is denoted as Me_2Si-Oct.

2.2.5 Synthesis of proton exchanged octosilicate and heat treatment in DMF

The following reference samples were prepared for the detailed characterization of the products using solid-state ^{29}Si NMR. According to previous reports,[47,48] protonated octosilicates (H-Oct) can be synthesized by treating Na-Oct with aqueous HCl. Na-Oct

(2.5 g) was dispersed in 0.1 M HCl aq. (250 mL) in a beaker and stirred at room temperature for 2 d. The resulting suspension was centrifuged, and the supernatant was removed. The resulting solid was washed twice with deionized water and dried to obtain H-Oct as a white powder.

For comparison with dimethyltin-modified samples, H-Oct was treated under the same conditions: 0.1 g H-Oct and 10 mL DMF were stirred at 100 °C for 2 d. The samples were washed three times with acetone and dried under reduced pressure. This sample was named H-Oct heat.

2.2.6 Characterization

The X-ray diffraction (XRD) patterns were obtained by a parallel method using a Rigaku RINT-Ultima III powder diffractometer (Cu Kα, $\lambda = 0.15418$ nm, 40 kV, 40 mA). Solid-state NMR spectra were recorded on a JEOL JNM-ECX400 spectrometer. Samples were packed in 4 mm zirconia sample tubes and spun at 6 kHz. ^{13}C cross-polarization (CP)/magic-angle spinning (MAS) NMR was measured at a resonance frequency of 99.6 MHz with a recycle delay of 10 s and contact time of 5 ms. ^{29}Si MAS NMR was measured at a resonance frequency of 78.6 MHz, with a 90° pulse and a recycle delay of 500 s. Solid-state 2D ^{1}H–^{29}Si heteronuclear correlation (HETCOR) spectra were recorded on the same spectrometer at resonance frequencies of 400 MHz for ^{1}H and 78.6 MHz for ^{29}Si with a contact time of 5 ms. Chemical shifts for ^{13}C and ^{29}Si nuclei were referenced to hexamethylbenzene ($\underline{\mathbf{C}}H_3$) at 17.4 ppm and polydimethylsilane at −33.8 ppm, respectively, as external standards. Fourier transform infrared (FT-IR) spectra were obtained using the KBr method on an FT/IR-6100 spectrometer (JASCO). Carbon, hydrogen, and nitrogen contents were measured using a CHN corder-type MT-5 (Yanaco).

The heating and oxidation temperatures (conc. 15% O_2) and temperature at the reduction furnaces were 950, 850, and 550 °C, respectively. The analysis was conducted by A-Rabbit-Science Japan Co., Ltd. The amounts of Si, Na, and Sn were determined using inductively coupled plasma optical emission spectrometry (ICP-OES) (Agilent Technologies, Agilent 5100). Samples were prepared using a melting method with $Li_2B_4O_7$ as the flux. High-resolution scanning electron microscopy (HR-SEM) images were obtained using an S-5500 microscope (Hitachi High Technologies Co.) at an accelerating voltage of 1 kV. Transmission electron microscopy (TEM), high-angle annular dark-field scanning transmission electron microscopy (HAADF-STEM), and STEM-energy dispersive X-ray spectroscopy (EDS) were performed using a JEM-1400Flash microscope (JEOL) at an accelerating voltage of 120 kV. STEM-EDS mapping was performed using a JEOL JED-2300 T detector. XPS spectra were measured using a JPS-9010MX (JEOL) spectrometer using Mg Kα excitation. The C 1p peak at the binding energy of 284.7 eV was used as a reference. Diffuse reflectance (DR) UV–Vis spectra were recorded on a V-660 spectrometer (JASCO) using a $BaSO_4$ plate as the reference. Sn K-edge XAFS analyses were conducted at the public beamline BL01B1 of Spring-8 at the Japan Synchrotron Radiation Research Institute.[49] The incident X-rays were monochromatized using a Si(311) double-crystal monochromator. The photon energy was calibrated at the inflection point of the Sn K-edge X-ray absorption near-edge structure (XANES) spectrum of the Sn metal foil to 29194.99 eV. The powdered samples were diluted with an appropriate amount of boron nitride (BN), pressed into pellets, and used for XAFS measurement. Sn K-edge XAFS spectra were analyzed using xTunes software.[50] After normalization, Fourier-transformation (FT) of k^3-weighted χ spectra in the k range of 3.0–14.0 $Å^{-1}$ was performed to obtain the FT-EXAFS spectra. The curve

fitting analysis for samples was conducted in the range of 1.2–1.9 Å using a FEFF8 program.[51] Density functional theory (DFT) calculations for the structural refinement of Me_2Sn-Oct and DMTO were performed using the BIOVIA Materials Studio software. The CASTEP module was used with the GGA-PBE functional.[52] The energy tolerance was 2.0×10^{-5} eV per atom, force tolerance was 0.05 eV $Å^{-1}$, maximum stress was 0.1 GPa, and displacement tolerance was 0.002 Å. The partial structural model was displayed using the VESTA software.[53]

2.3 Results and Discussion

2.3.1 Preparation of Na-Oct, C_{16}TMA-Oct, and H-Oct

The powder XRD patterns of Na-Oct, C_{16}TMA-Oct, and H-Oct were shown in Fig. 2.1A. The all peaks of Na-Oct are consistent with previous reports, with a basal spacing *d* value of 1.11 nm (2θ = 3.18°). C_{16}TMA-Oct (Fig. 2.1(A)(b)) exhibited a diffraction peak at 2θ = 3.18° corresponding to the basal spacing *d* value of 2.79 nm and the in-plane (400) peak of octosilicate at 2θ = 49.4° (*d* = 0.184 nm). The basal spacing of H-Oct was *d* = 0.75 nm (2θ = 11.74°) and the in-plane (400) peak of octosilicate at 2θ = 49.6° (*d* = 0.184 nm). For ^{29}Si MAS NMR spectra of Na-Oct, C_{16}TMA-Oct, and H-Oct (Fig. 2.1(B) and Table 2.1), signals attributed to Q^3 (**Si**$(OSi)_3OH/O^-$) and Q^4 (**Si**$(OSi)_4$) sites appeared with an integral intensity ratio of 1:1.[45] By the elemental analysis (Table 2.2) for C_{16}TMA-Oct, it was confirmed that Na decreases and N increases due to the progress of ion exchange by C_{16}TMA cations. A decrease in Na caused by the progress of protonation was also confirmed. The FT-IR spectrum of C_{16}TMA-Oct (Fig. 2.2(A) (b)) showed the bands attributed to CH_2 asymmetric and symmetric stretching vibrations and CH_3 asymmetric and symmetric stretching vibrations of the alkyl groups at 2920, 2850, 2950, and 2870 cm^{-1}, respectively.[54] In addition, a band attributed to the Si–OH stretching vibrations on the layer surface was observed at 960 cm^{-1}.[55] The ^{13}C CP/MAS NMR spectra of C_{16}TMA-Oct and the assignments of the signals are shown in Fig. 2.2(B). All signals were assigned according to the previous report.[56] A signal at 33.5 ppm is indicating that the conformation of alkyl chain of C_{16}TMA-Oct is all-*trans* states.

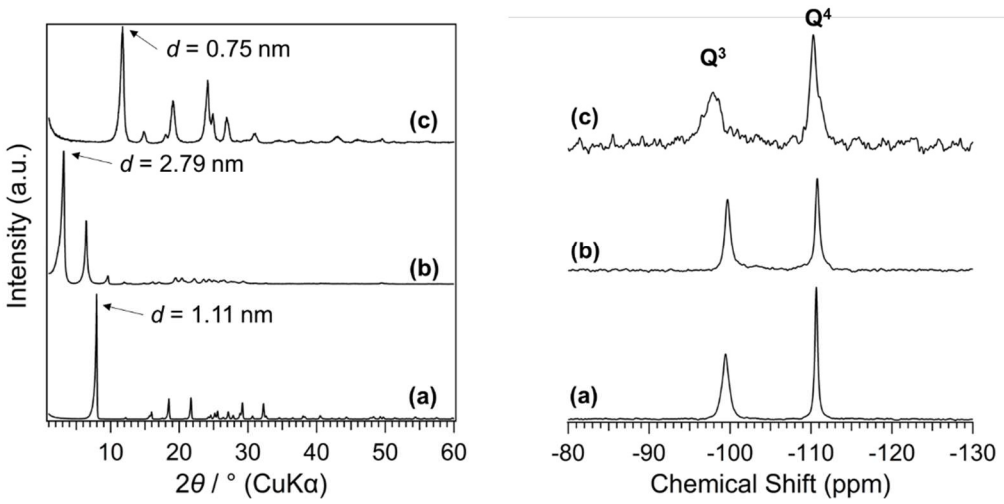

Fig. 2.1 (A) Powder XRD patterns and (B) ^{29}Si MAS NMR spectra of (a) Na-Oct, (b) C_{16}TMA-Oct, and (c) H-Oct.

Table 2.1 Chemical shift and integral intensity ratio of ^{29}Si MAS NMR spectra.

Samples	Chemical Shift (ppm)		Integral intensity ratio
	Q^3	Q^4	Q^3/Q^4
Na-Oct	−100	−111	1.00
C_{16}TMA-Oct	−100	−111	1.00
H-Oct	−98	−110	1.00

Table 2.2 Carbon, nitrogen, silicon, and sodium contents.

Sample name	C / wt%	N / wt%	Si / wt%	Na / wt%
Na-Oct	-	-	30.6	5.4
C_{16}TMA-Oct	36.8	2.4	18.7	0.3
H-Oct	-	-	41.9	0.5

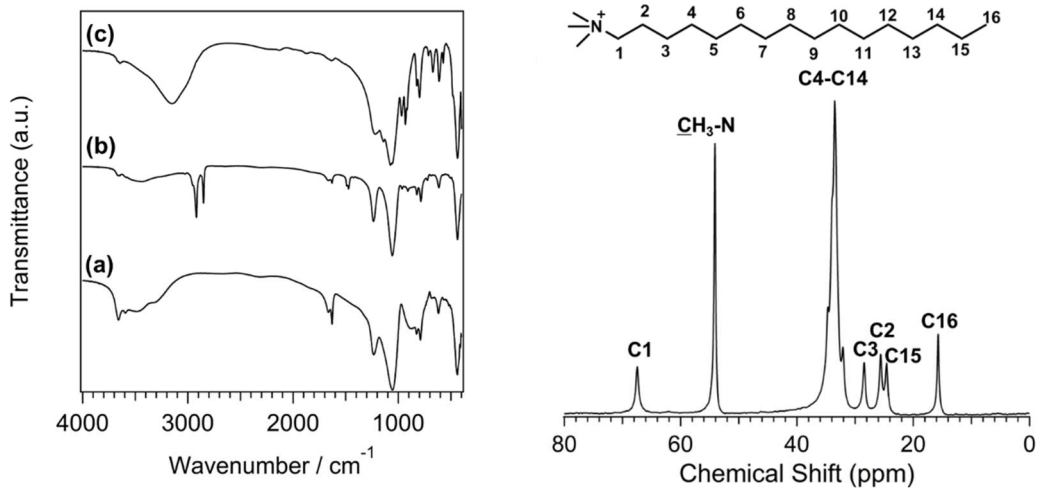

Fig. 2.2 (A) FT-IR spectra of (a) Na-Oct, (b) C_{16}TMA-Oct, and (c) H-Oct and (B) ^{13}C CP/MAS NMR spectrum of C_{16}TMA-Oct.

2.3.2 Preparation of dimethyltin-modified octosilicates

The powder XRD patterns of C_{16}TMA-Oct and Me_2Sn-Oct_*X* (*X* = 0.1, 0.25, 0.5, and 10) samples are shown in Fig. 2.3. The basal spacings of Me_2Sn-Oct_0.1, _0.25, _0.5, and _10 (Figs. 2.3 (b)–(e)) were 2.79, 1.23, 1.08, and 1.18 nm, respectively. Although the *d* value of Me_2Sn-Oct_0.1 was nearly unchanged from that of C_{16}TMA-Oct, the *d* values of Me_2Sn-Oct_0.25, _0.5, and _10 became much smaller, indicating the elimination of $C_{16}TMA^+$, which is consistent with the results of the elemental analysis and solid-state ^{13}C NMR described below. For Me_2Sn-Oct_*X* (*X* = 0.25, 0.5, and 10), the peak probably derived from in-plane crystallinity was observed at 48.5° (*d* = 0.187 nm), suggesting the in-plane lattice expansion of the octosilicate owing to the introduction of dimethyltin groups. This is similar to the shifting of the (302) peak of the dealuminated BEA-type zeolite to a lower angle because of the framework expansion due to the introduction of Sn species into the silanol nest.[57]

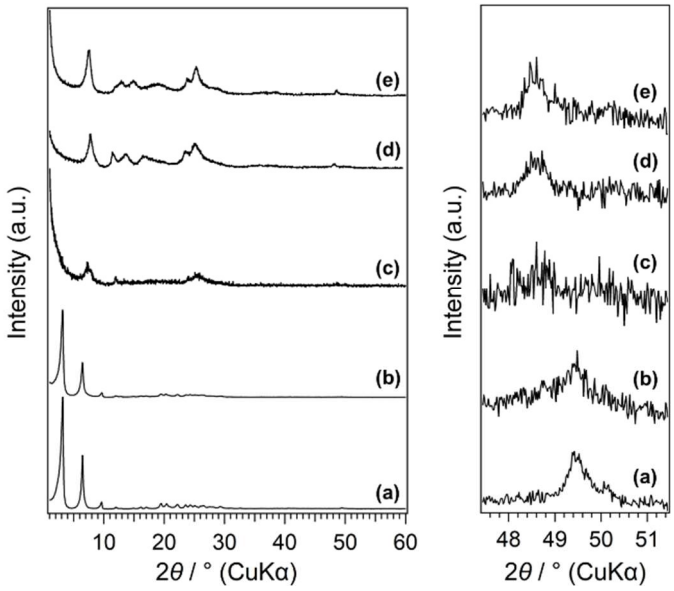

Fig. 2.3 (A) Powder XRD patterns of (a) C_{16}TMA-Oct, (b) Me_2Sn-Oct_0.1, (c) Me_2Sn-Oct_0.25, (d) Me_2Sn-Oct_0.5, and (e) Me_2Sn-Oct_10.

The FT-IR spectra of C_{16}TMA-Oct and Me_2Sn-Oct_*X* are shown in Fig. 2.4(A). For Me_2Sn-Oct_*X* (Figs. 2.4(A)(b)–(e)), the intensities of the C–H stretching vibrations were gradually weakened with increasing *X*, suggesting the elimination of the C_{16}TMA cations. In the spectra of Me_2Sn-Oct_0.5 and Me_2Sn-Oct_10 (Figs. 2.4(A)(d) and (e)), the small bands at 540 and 560 cm^{-1} were attributed to Sn–C stretching vibrations.[58–60] For Me_2Sn-Oct_*X* (Figs. 2.4(A)(b)–(e)), the band of Si–OH groups (960 cm^{-1}) decreased from that of C_{16}TMA-Oct. A similar decrease was observed upon silylation,[46] suggesting that a condensation reaction occurred between the SnCl and SiOH groups. These results suggest the immobilization of methyltin groups on the layer surfaces.

The FT-IR spectra of Me_2Sn-Oct_*X* (*X* = 0.25, 0.5, and 10; Figs. 2.4(A)(c)–(e)) showed an absorption band at ~1700 cm^{-1}, which was attributed to the C=O stretching vibration of acetone. For Me_2Sn-Oct_10 (Fig. 2.4(A)(e)), a sharp absorption band was observed at ~1650 cm^{-1}, which can be attributed to the C=O stretching vibration of DMF.

These results indicated that the solvent used for the reaction and washing remained. Compared with the C=O stretching vibrations of neat acetone and DMF, the C=O bands were observed at lower wavenumbers, suggesting interactions between the carbonyl groups and interlayer silanol groups or immobilized alkyltin groups.[61,62] Although further drying at 120 °C under vacuum was performed for Me_2Sn-Oct_10, these solvent molecules could not be removed.

The ^{13}C CP/MAS NMR spectra of $C_{16}TMA$-Oct and Me_2Sn-Oct_*X* (*X* = 0.1, 0.25, 0.5, and 10) are shown in Fig. 2.4(B). The spectra of Me_2Sn-Oct_*X* (Figs. 2.4(B)(b)–(e)) show that the signals derived from the $C_{16}TMA$ cations gradually decrease with increasing *X*. The $C_{16}TMA$ cations were nearly eliminated by adding 0.5 equivalent of Me_2SnCl_2. This result is reasonable because when Me_2SnCl_2 reacts with a $SiOH/SiO^-(C_{16}TMA^+)$ pair to form two Sn–O–Si bonds, $C_{16}TMACl$ and HCl are generated. The generated HCl converts the unreacted $SiO^-(C_{16}TMA^+)$ site to SiOH and subsequently generates additional $C_{16}TMACl$ (Scheme 2.2). $C_{16}TMACl$ was finally removed by washing with acetone. In addition, the spectra of Me_2Sn-Oct_*X* (*X* = 0.25, 0.5, and 10; Figs. 2.4(B)(c)–(e)) show broad signals at ~10 ppm, attributable to the methyl groups attached to Sn (**C**H_3–Sn).[63] The signal broadening may have been caused by dipole coupling from the Sn atoms. Furthermore, Me_2Sn-Oct_*X* exhibited signals attributed to acetone (**C**H_3: 31.7 ppm, **C**=O: 210 ppm) and DMF (**C**H_3: 39 ppm and 33 ppm, **C**=O: 165 ppm), which agreed with the FT-IR results.

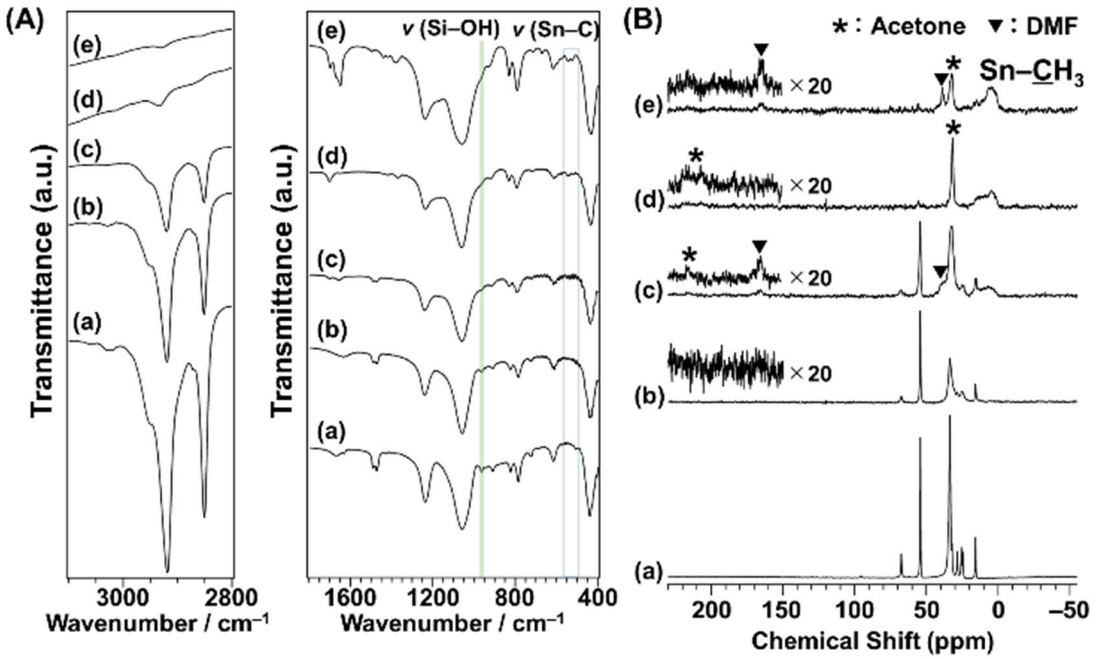

Fig. 2.4 (A) FT-IR spectra and (B) ^{13}C CP/MAS NMR spectra of (a) $C_{16}TMA$-Oct, (b) Me_2Sn-Oct_0.1, (c) Me_2Sn-Oct_0.25, (d) Me_2Sn-Oct_0.5, and (e) Me_2Sn-Oct_10.

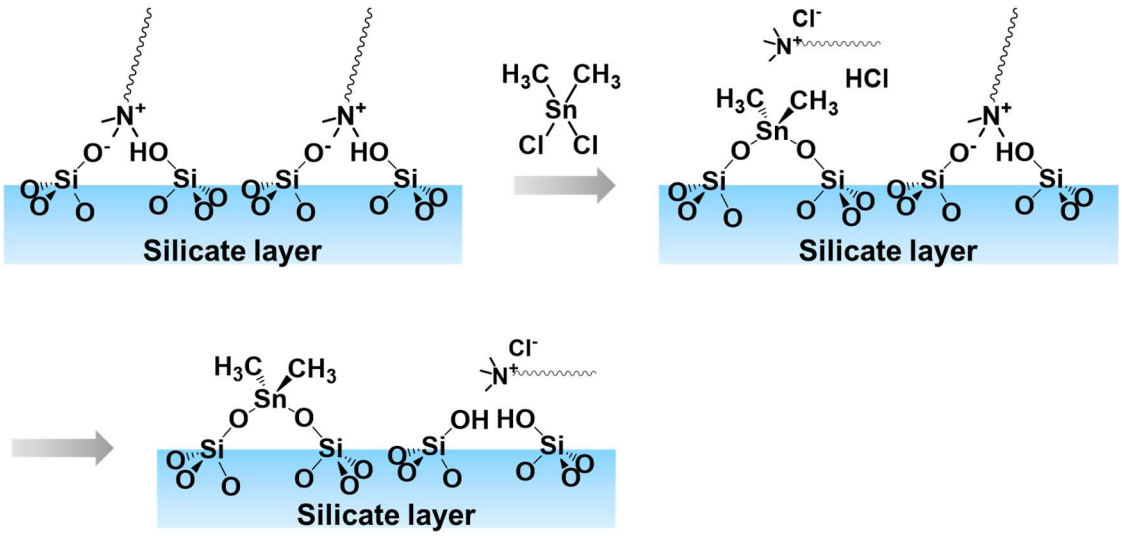

Scheme 2.2 Possible reaction scheme for the elimination of two $C_{16}TMA^+$ cations with one Me_2SnCl_2.

The results of the elemental analyses are listed in Table 2.1. The N/Si ratio of C_{16}TMA-Oct and Me_2Sn-Oct_*X* (*X* = 0.1, 0.25, and 0.5) gradually decreased with increasing *X* (0.26→0.18→0.07→0.01), which was owing to the removal of C_{16}TMA cations. The N/Si ratio of Me_2Sn-Oct_10 (0.08) was higher than that of Me_2Sn-Oct_0.5 (0.01). This was probably owing to the remaining DMF, as indicated by the FT-IR and solid-state ^{13}C NMR analyses. The tin content of Me_2Sn-Oct_*X* gradually increased with increasing *X*, indicating a correlation between the elimination of interlayer C_{16}TMA cations and modification with Sn. The Sn/Si ratios of Me_2Sn-Oct_*X* (*X* = 0.1, 0.25, 0.5, and 10) were 0.03, 0.08, 0.13, and 0.14, respectively (Table 2.1). Assuming the bidentate immobilization of dimethyltin on all octosilicate reaction sites, the Sn/Si ratio should be 0.25. Therefore, the degrees of modification with Sn of Me_2Sn-Oct_*X* (*X* = 0.1, 0.25, 0.5, and 10) were 12%, 32%, 52%, and 56%, respectively.

Table 2.1. Carbon, nitrogen, silicon, and tin contents of the samples.

Sample name	C / wt%	N / wt%	Si / wt%	Sn / wt%	N/Si ratio	Sn/Si ratio
C_{16}TMA-Oct	36.8	2.4	18.7	-	0.26	-
Me_2Sn-Oct_0.1	30.7	2.0	22.1	3.2	0.18	0.03
Me_2Sn-Oct_0.25	13.4	1.0	27.9	9.8	0.07	0.08
Me_2Sn-Oct_0.5	7.1	0.1	30.9	16.6	0.01	0.13
Me_2Sn-Oct_10	7.3	1.1	28.7	17.1	0.08	0.14

SEM, TEM, and EDS mapping images of Me_2Sn-Oct_*X* (*X* = 0.1, 0.25, 0.5, and 10) are shown in Fig. 2.5. All samples exhibited an octosilicate-derived platelet morphology with a uniform distribution of Sn, suggesting the grafting of Sn species on the entire surface of the silicate layers. The EDS mapping image of Me_2Sn-Oct_0.1 also showed that a larger amount of Sn species was present near the edge region of the plate.

EDS quantitative analysis (Fig. 2.5, right) confirmed that the Sn/Si ratio increased with increasing *X* in Me_2Sn-Oct_*X*. This trend in the local observations is consistent with the overall elemental analysis using ICP-OES and CHN described above.

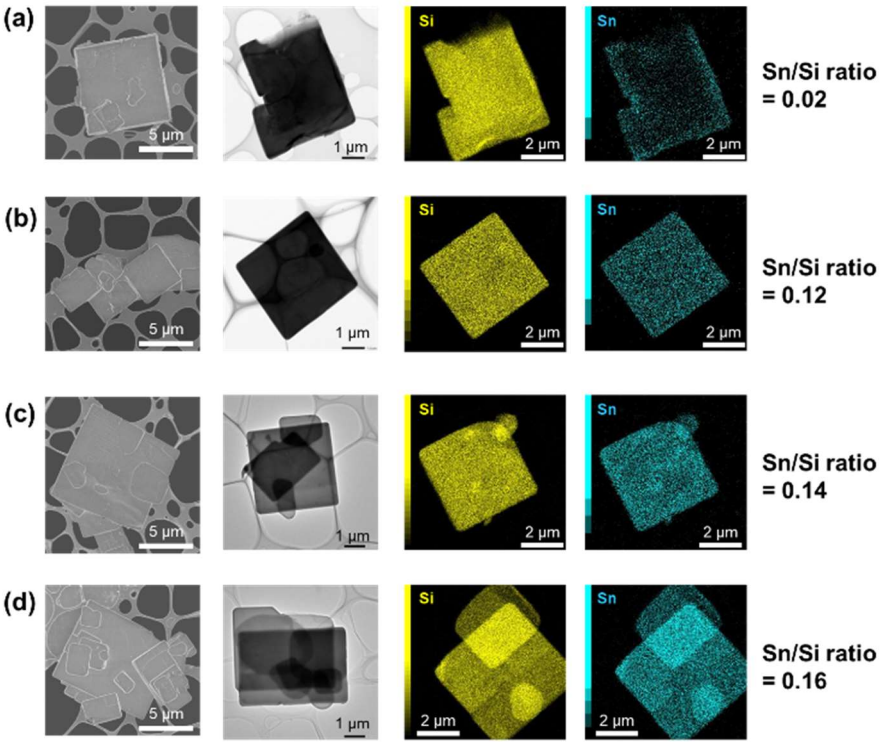

Fig. 2.5 Electron microscopy images of (a) Me_2Sn-Oct_0.1, (b) Me_2Sn-Oct_0.25, (c) Me_2Sn-Oct_0.5, and (d) Me_2Sn-Oct_10. From left to right: SEM images, TEM images, EDS mapping images, and Sn/Si ratios by EDS quantitative analysis.

Fig. 2.6 shows the solid-state ^{29}Si MAS NMR spectra of C_{16}TMA-Oct and Me_2Sn-Oct_*X* (*X* = 0.1, 0.25, or 0.5). For C_{16}TMA-Oct (Fig. 2.6 (a)), signals attributed to Q^3 (**Si**$(OSi)_3OH/O^-$) and Q^4 (**Si**$(OSi)_4$) sites appeared at −100 and −111 ppm, respectively, with an integral intensity ratio of 1:1.[45] For the spectra of Me_2Sn-Oct_*X* (Figs. 2.6 (b)–(d)), the integral intensity ratio of the Q^3 signal to the Q^4 signal decreased, and new signals

appeared at −103 and −107 ppm. For Me_2Sn-Oct_10, the original Q^3 signal disappeared, and signals were observed at −103, −107, and −110 ppm.

Herein, the signals at −103 and −107 ppm were named Q^a and Q^b, respectively. The relative integral intensity ratios of the Q^3, Q^a, and Q^b signals to those of the Q^4 signal are listed in the inset table of Fig. 2.6. For Me_2Sn-Oct_*X* (*X* = 0.1, 0.25, and 0.5), the sum of Q^3, Q^a, and Q^b was approximately equal to Q^4, indicating that the ratio of (Q^a + Q^b) coincided with the decrease in the ratio of the Q^3 signal to that of C_{16}TMA-Oct. Therefore, Q^a and Q^b are related to silicon environments that emerge from the reactions of the original Q^3 environments. As described earlier, the introduction of methyltin groups and the elimination of $C_{16}TMA^+$ were confirmed. Accordingly, these two new environments were assumed to be dimethyltin-modified sites (**Si**$(OSi)_3O$–Sn) and the confronting disilanol sites (**Si**$(OSi)_3OH$/ **Si**$(OSi)_3OH$).

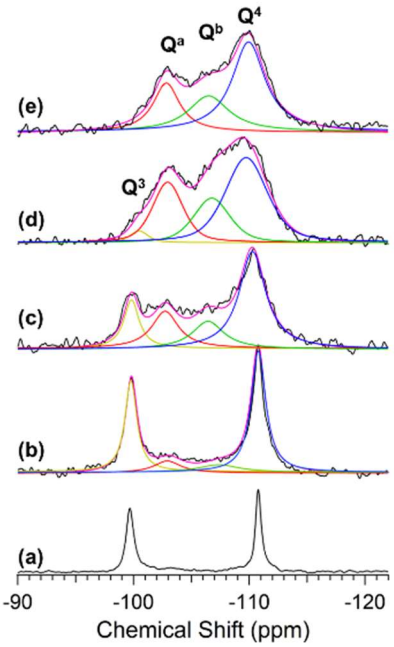

	Integral intensity ratio			
	Q^3	Q^a	Q^b	Q^4
	−100 ppm	−103 ppm	−107 ppm	−110 ppm
(e)	-	0.46	0.53	1.00
(d)	0.05	0.51	0.45	1.00
(c)	0.29	0.38	0.34	1.00
(b)	0.62	0.19	0.18	1.00
(a)	1.00			1.00

Fig. 2.6 ^{29}Si MAS NMR spectra of (a) C_{16}TMA-Oct, (b) Me_2Sn-Oct_0.1, (c) Me_2Sn-Oct_0.25, (d) Me_2Sn-Oct_0.5, and (e) Me_2Sn-Oct_10. Black lines are the original spectra, pink lines are the fitting spectra, yellow lines indicate the Q^3 signals at −100 ppm, red lines indicate the Q^a signal at −103 ppm, green lines indicate the Q^b signal at −107 ppm, and blue lines indicate the Q^4 signal at −110 ppm. The inserted table shows the relative integral intensity ratio of each signal.

The ^{29}Si MAS NMR analysis of the proton-exchanged octosilicate (H-Oct) was performed to obtain information on the chemical shifts of the silanol sites. A Q^3 signal was observed at −98 ppm for H-Oct (Fig. 2.7(A)(a)). H-Oct_heat, obtained by stirring H-Oct in DMF at 100 °C for 2 d followed by washing with acetone (see Experimental Section), showed that the Q^3 signal shifted to −103 ppm (Fig. 2.7(A)(b)). The retention of acetone in the interlayer spaces of H-Oct_heat was confirmed using ^{13}C CP/MAS NMR (Fig. 2.7(B)) and XRD (Fig. 2.7(C)), which was consistent with the literature.[47] The Q^3 signal of H-Oct partially shifts to higher fields by heating.[64] Based on these facts, the Q^a

signal observed at −103 ppm for Me_2Sn-Oct_*X* is attributed to the confronting silanol sites (**Si**$(OSi)_3OH$/**Si**$(OSi)_3OH$). Moreover, the ^1H MAS NMR analysis revealed that the single signal derived from the SiOH group in H-Oct (Fig. 2.7(D)(a)) split into two signals after heating (H-Oct_heat, Fig. 2.7(D)(b)). FT-IR spectra of H-Oct and H-Oct_heat (Fig. 2.7(E)) showed an increase in the intensity of the band at 3650 cm^{-1} assigned to the stretching vibration of isolated SiO–H groups. Therefore, these results might suggest conformational changes of confronting SiOH groups from isotropic hydrogen bonding (Fig. 2.7(F)(a)) to anisotropic one (Fig. 2.7(F)(b)).

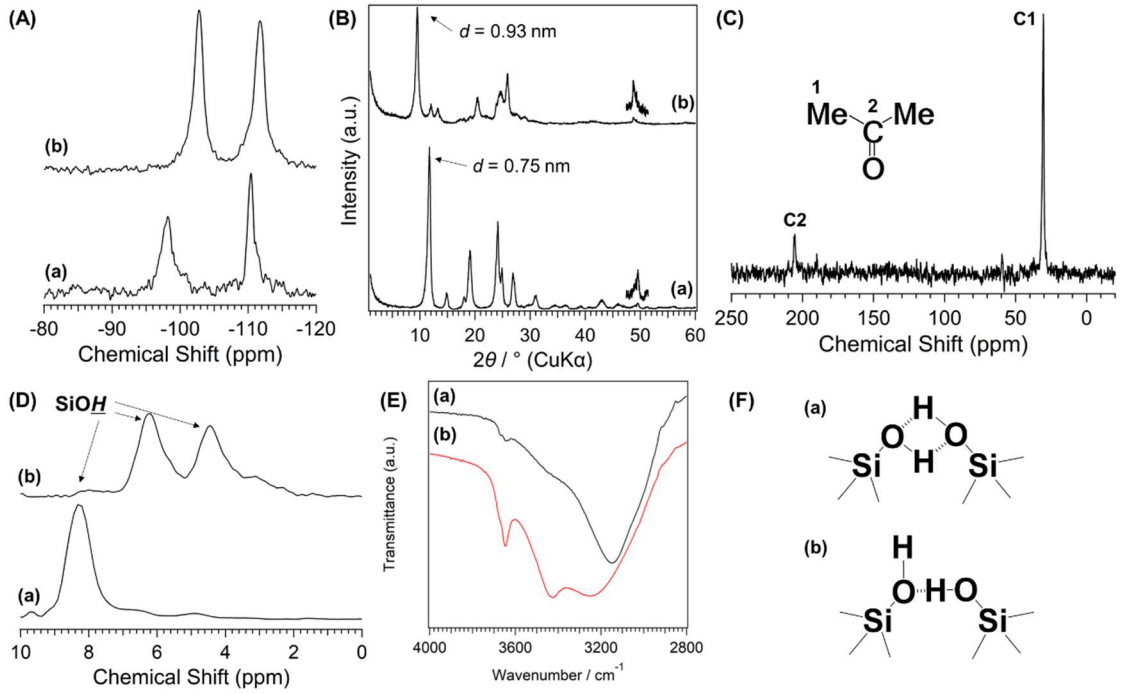

Fig. 2.7 (A) ^{29}Si MAS NMR spectra and (B) powder XRD patterns of (a) H-Oct and (b) H-Oct_heat, (C) ^{13}C CP/MAS NMR spectrum of H-Oct_heat, (D) ^1H projections of the ^1H–^{29}Si HETCOR spectra and (E) FT-IR spectra of (a) H-Oct and (b) H-Oct_heat, and (F) possible conformations of confronting silanol pairs of (a) H-Oct and (b) H-Oct_heat.

The other signal at −107 ppm (Q^b) is attributed to dimethyltin-modified sites (**Si**$(OSi)_3O$–Sn). Such a high-field shift of the ^{29}Si NMR signal owing to bonding with

organotin is consistent with a previous report.[65] Furthermore, because the integral intensity ratio of Q^b corresponds to the amount of Sn-modified Si, the degree of modification with Sn ($Q^b \times 100$) can be estimated. The degrees of Sn modification for Me_2Sn-Oct_*X* (*X* = 0.1, 0.25, 0.5, and 10) were 18%, 34%, 45%, and 53%, respectively, which were in good agreement with those calculated from the Sn/Si ratio by elemental analysis.

With increasing amounts of Me_2SnCl_2, the elimination of nearly all C_{16}TMA cations and a decrease in basal spacing were observed (Figs. 2.3 and 2.4), indicating that the dimethyltin groups were grafted not only on the outer surface of the layer but also between the layers. In the EDS mapping image of Me_2Sn-Oct_0.1 (Fig. 2.5 (a)), the tin species were more clearly visible in the edge region of the octosilicate platelet crystal, suggesting that the dimethyltin immobilization reaction progressed gradually from the edge of the crystal. However, the degree of modification with dimethyltin reached a limit of approximately 50% (Table 2.1 and Fig. 2.6), which was lower than the degree of silylation using silane analogues (88% for Me_2SiCl_2, Fig. 2.8(A)).

The powder XRD data (Fig. 2.3) show that the diffraction angles derived from the in-plane crystallinity decreased to 48.5°. The diffraction angle of the 400 planes of Me_2Si-Oct (Fig. 2.8(B)) was 48.6°, indicating that the lattice expansion was similar to that caused by a lower degree of modification with the dimethyltin species (Me_2Sn-Oct_10). It is assumed that the confronting SiOH/SiO^- groups of octosilicate are distorted by grafting dimethyltin groups because the Sn–O bond is slightly longer than the Si–O bond.[66] The introduction of dimethyltin species into the reaction sites causes in-plane framework expansion, narrowing the distance between the adjacent confronting disilanol groups. This narrowing might be related to the conformational changes in hydrogen

bonding of confronting silanol groups (Fig 2.7(D)). Consequently, the decrease in the reactivity of the narrowed sites prevents the introduction of additional dimethyltin species (Scheme 2.3). Therefore, the silicate layers of Me_2Sn-Oct_10 might consist of alternate dimethyltin-modified and nonmodified confronting disilanol sites.

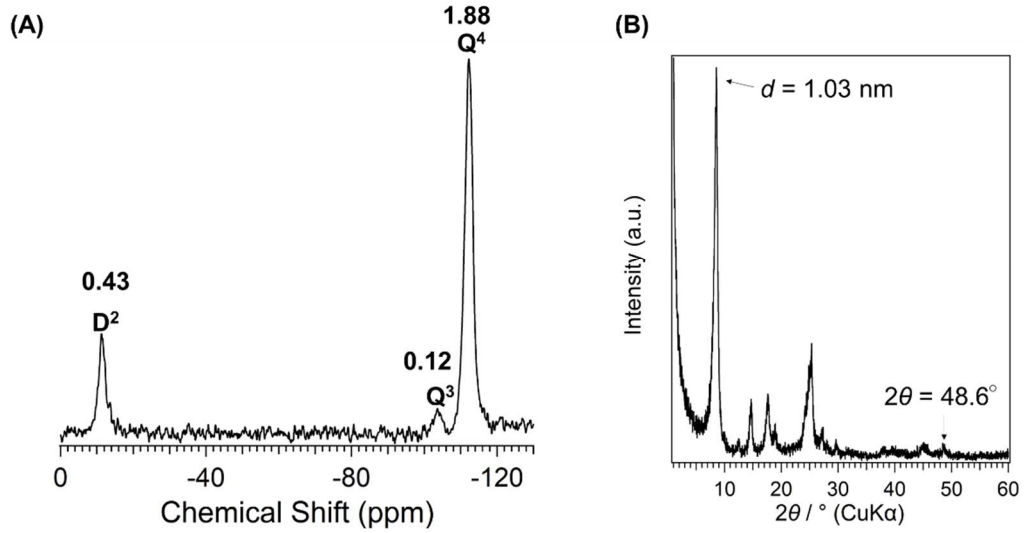

Fig. 2.8 (A) ^{29}Si MAS NMR spectrum and (B) powder XRD pattern of Me_2Si-Oct

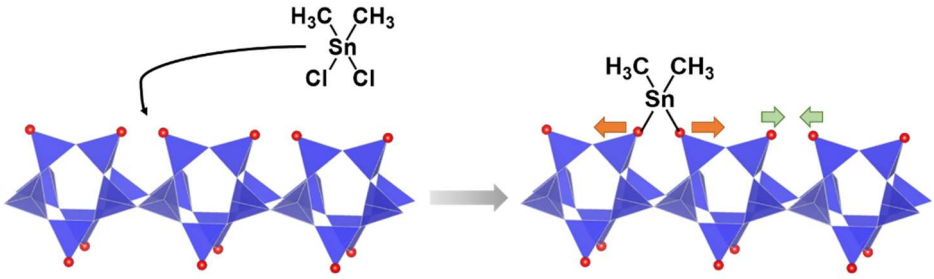

Scheme 2.3 A possible mechanism which explains the limited degree of dimethyltin-modification (approximately 50%).

The UV–Vis (Fig. 2.9(A)) measurements were performed to investigate the local environment of Sn in the samples. For the spectra of Me_2Sn-Oct_*X*, a shoulder band was observed at 220 nm. This absorption band was attributed to O→Sn LMCT (ligand to metal charge transfer), generally observed for tin-containing zeolites and mesoporous silica.[67,68] For the UV–Vis spectrum of dimethyltin oxide (DMTO), some broad

absorption bands were observed at 200–250 nm, whereas a relatively sharp absorption band was observed for Me_2Sn-Oct_*X*. Thus, the extra-framework DMTO derived from the hydrolytic condensation of Me_2SnCl_2, an undesired reaction during the synthesis, was negligible. Me_2Sn-Oct_*X* (*X* = 0.25, 0.5, and 10) and H-Oct_heat exhibited absorption bands at ~255 nm. This band was attributed to the n→π* transition of acetone, although it is typically observed at ~280 nm.[69] The interaction between the carbonyl groups of acetones and surface silanol groups might cause this shift towards a lower wavelength.

The XPS analysis of Me_2Sn-Oct_*X* was also performed (Fig. 2.9(B)). In the spectrum of Me_2Sn-Oct_0.1 (Fig. 2.9(B)(a)), Sn-derived peaks were observed at 486.2 eV (Sn $3d_{5/2}$) and 494.7 eV (Sn $3d_{3/2}$), which gradually shifted towards higher energies up to 487.4 and 495.8 eV with increasing *X* (Figs. 2.9(B)(a)–(d)). The binding energy regions of these peaks correspond to tetravalent Sn. The Sn $3d_{5/2}$ peak of the $Sn(OSi)_4$ species in tin-containing zeolites appears at ~487.5 eV.[70] The Sn $3d_{5/2}$ peak for Me_2Sn-Oct_0.1 appears on the low binding energy side because the central Sn is electron-rich owing to the replacement of two of the four coordinating oxygen atoms with more electron-donating carbon atoms. Shifts in the binding energy towards higher energies for Me_2Sn-Oct_*X* were observed with increasing amounts of tin. This may be associated with the in-plane lattice expansion of the silicate layers, as confirmed by powder XRD. The distortion around Sn became more prominent as grafting was progressed. This distortion may increase the binding energy.[71]

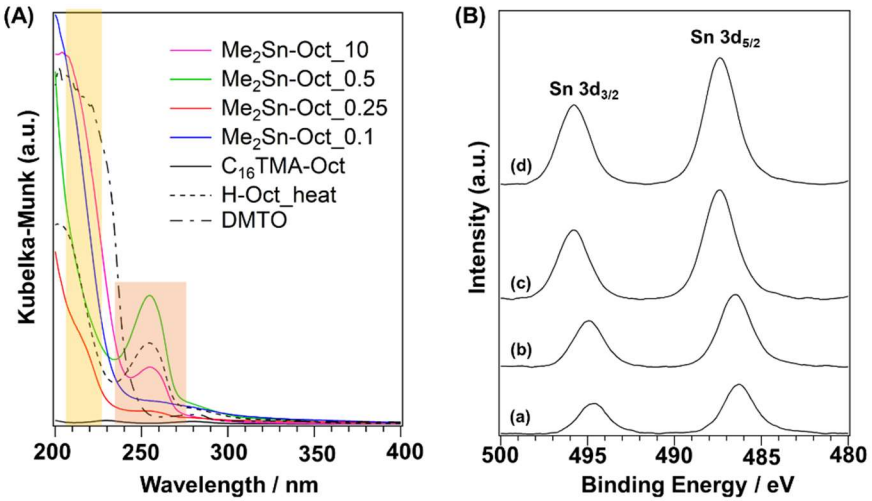

Fig. 2.9 (A) UV–Vis spectra of C_{16}TMA-Oct, Me_2Sn-Oct_0.1, Me_2Sn-Oct_0.25, Me_2Sn-Oct_0.5, Me_2Sn-Oct_10, and H-Oct_heat. (B) XPS profiles of (a) Me_2Sn-Oct_0.1, (b) Me_2Sn-Oct_0.25, (c) Me_2Sn-Oct_0.5, and (d) Me_2Sn-Oct_10.

Further detailed information on the local structure of Sn in the samples was obtained using Sn K-edge XAFS analysis. The XANES spectra are shown in Fig. 2.10(A). The values of absorption edge in each spectrum are listed in Table 2.2. Sn foil, SnO, SnO_2, and DMTO were used as the reference samples. DMTO is a five-coordinate organotin compound consisting of Sn bonded to two methyl groups and three oxygen atoms. The two Sn–O–Sn chains interact with each other. Thus, DMTO has a ladder-like structure.[72,73] DMTO was used as a reference sample for dimethyltin compounds. The absorption edges of SnO and SnO_2 were at 29196.8 and 29200.6 eV, respectively. The absorption edge of DMTO was at 29198.6 eV, indicating a shift in the absorption edge towards lower energies than that of SnO_2. This shift was owing to the partial substitution of the Sn^{4+} surroundings from oxygen atoms to carbon atoms with lower electronegativity, which was consistent with the XPS results. The absorption edges of Me_2Sn-Oct_*X* were shifted to lower energy compared to those of DMTO, suggesting lower coordination numbers. In addition, the values of the absorption edges remained unchanged regardless

of the value of *X*, that is, the degree of dimethyltin modification. This suggested that the local environments of the dimethyltin species were similar.

The k^3-weighted Sn K-edge EXAFS spectra and FT-EXAFS spectra obtained in the range k = 3–14 $Å^{-1}$ are shown in Figs. 2.10(B) and (C). The coordination atoms, coordination numbers, and bond distances around Sn were estimated by curve-fitting the FT-EXAFS spectra. For the reference samples (Sn foil, SnO, SnO_2, and DMTO; Figs. 2.10(C)(a)–(d)), the second coordination sphere peaks attributed to Sn–Sn scattering were observed between 2.2 and 3.9 Å. By contrast, no peaks are observed for Me_2Sn-Oct_*X* (Figs. 2.10(C)(e)–(h)). Elements with different backscattering factors in EXAFS vibrations are less likely to scatter at longer distances. Therefore, the Sn–Si scattering of Sn-containing zeolites with isolated Sn(IV) in the silica framework is very small.[74,75] In the current system, Sn–Si scattering was reasonably absent. In addition, the absence of peaks in this region indicates that only a few Sn–O–Sn bonds were present, indicating that condensation of dimethyltin dichloride did not occur.

The data calculated by curve fitting the FT-EXAFS data are provided in Table 2.3. The parameters for Sn foil, SnO, and SnO_2 were in good agreement with the previous report.[76] The model of DMTO (Figs. 2.11 (a) and (b)) was prepared following the previously proposed double-stranded ladder-like structures.[72,73] Although the first coordination sphere consists of oxygen and carbon bonded to Sn, each peak was curve-fitted as Sn–O bonds because these elements have indistinguishable backscattering factors. Therefore, the scattering path is described as Sn–O (C). The first coordination sphere for DMTO had 4.7 coordinating atoms (oxygen or carbon) with distances of 2.08 Å, respectively. Moreover, the peak appearing in the second coordination sphere was the scattering derived from Sn–Sn at a distance of 3.27 Å. Thus, the double-chain ladder

structure of dimethyltin oxide proposed in a previous report[72,73] was verified. The Sn–O (C) bond distances for Me_2Sn-Oct_*X* were 2.03 or 2.04 Å, which was shorter than that of DMTO. The Sn–O bond distance in isolated SnO_4 in zeolites is shorter than that in SnO_2 because the coordination number is reduced from 6 to 4.[74] The shorter Sn–O (C) bonds for the dimethyltin-modified octosilicate than that for DMTO with five-coordinated Sn can be explained by the four-coordinated state of the dimethyltin species on the silicate layers. Because the presence of dimethyltin species on the interlayer surfaces has been confirmed by other analyses above, the four-coordinated Sn species suggest the dipodally grafted dimethyltin species. Therefore, the curve fitting results for Me_2Sn-Oct_*X* are consistent with a dimethyltin-grafted octosilicate structure model (Fig. 2.11 (c)). Thus, the Sn K-edge XAFS measurements of Me_2Sn-Oct_*X* revealed the local structure of the dimethyltin groups.

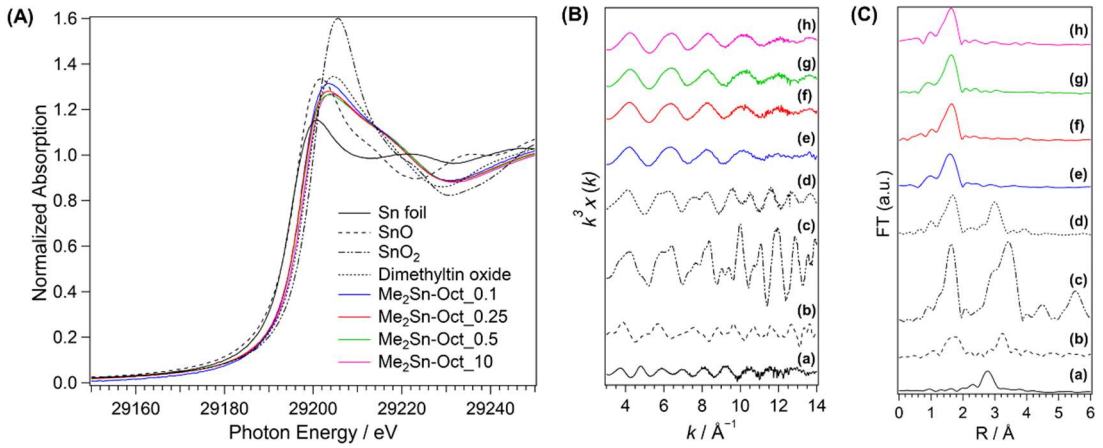

Fig. 2.10 (A) XANES spectra, (B) EXAFS spectra, and (C) FT-EXAFS spectra of (a) Sn foil, (b) SnO, (c) SnO_2, (d) dimethyltin oxide (DMTO), (e) Me_2Sn-Oct_0.1, (f) Me_2Sn-Oct_0.25, (g) Me_2Sn-Oct_0.5, and (h) Me_2Sn-Oct_10.

Table 2.2 The values of the adsorption edge for each spectrum.

Sample name	absorption edges / eV
Sn foil	29195.0
SnO	29196.8
SnO_2	29200.6
DMTO	29198.6
Me_2Sn-Oct_0.1	29197.2
Me_2Sn-Oct_0.25	29197.1
Me_2Sn-Oct_0.5	29197.2
Me_2Sn-Oct_10	29197.2

Table 2.3 Structural parameters of the sample and values from the curve-fitting analysis.

Sample names	Path [a]	N [b]	R (Å) [c]	σ^2 (Å^2) [d]	R factor [e]
Sn foil	Sn–Sn	4.0 (3)	3.00 (4)	0.011 (5)	8.0
SnO	Sn–O	4.3 (4)	2.17 (5)	0.009 (6)	10.8
	Sn–Sn	3.0 (3)	3.51 (4)	0.006 (4)	6.4
SnO_2	Sn–O	5.6 (2)	2.04 (2)	0.003 (2)	8.7
	Sn–Sn	2.3 (1)	3.18 (2)	0.003 (2)	10.5
	Sn–Sn	7.6 (2)	3.74 (2)	0.004 (2)	
DMTO	Sn–O (C)	4.7 (2)	2.08 (3)	0.006 (3)	7.3
	Sn–Sn	2.6 (2)	3.27 (3)	0.005 (2)	8.7
Me_2Sn-Oct_0.1	Sn–O (C)	4.4 (3)	2.04 (4)	0.006 (4)	9.7
Me_2Sn-Oct_0.25	Sn–O (C)	4.0 (2)	2.04 (3)	0.005 (3)	10.6
Me_2Sn-Oct_0.5	Sn–O (C)	4.0 (2)	2.03 (3)	0.005 (3)	10.6
Me_2Sn-Oct_10	Sn–O (C)	4.0 (2)	2.03 (3)	0.005 (3)	10.4

[a] Path denotes the scattering path of the photoelectrons included in the model. [b] N denotes the coordination number corresponding to the scattering path. [c] R denotes bond length. [d] σ^2 denotes the Debye-Waller factor. [e] R factor = $(\Sigma(k^3\chi^{data}(k) - k^3\chi^{fit}(k))^2)^{1/2}/(\Sigma(k^3\chi^{data}(k))^2)^{1/2}$.

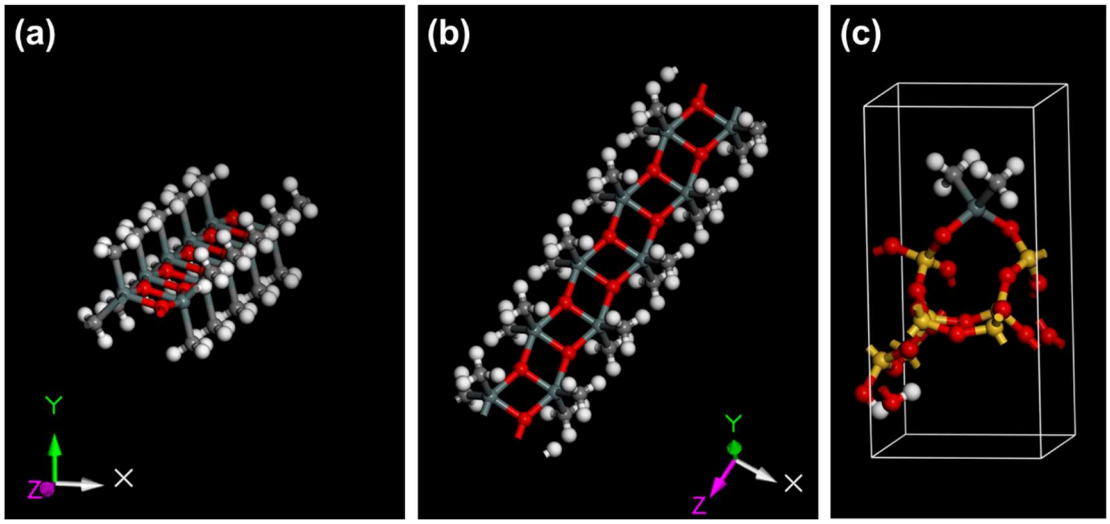

Fig. 2.11 Structural models of (a)(b) DMTO and (c) Me_2Sn-Oct_*X*

2.4 Conclusion

The interlayer silanol groups of the layered octosilicate were modified with Me_2SnCl_2, and the isolated dimethyltin species were grafted onto the surface. The degree of modification increased with increasing amounts of dimethyltin dichloride. When 10 equivalents of Me_2SnCl_2 were added to the reaction sites, approximately 50% of the total silanol sites of the octosilicate were modified. It was assumed that the larger Sn relative to the confronting silanol site caused the expansion of the framework. Accordingly, a possible structure was proposed in which every other silanol site is modified with dimethyltin groups. This report shows that well-defined metal species can be immobilized on regularly arranged reaction sites on the surfaces of crystalline layered silicates. Furthermore, it is notable that the arrangement of the immobilized dimethyltin groups was distinctly different from that of the dimethylsilyl groups when silane analogues were used. The use of layered silicates as crystalline silica supports for isolated alkyltin catalysts will become more promising.

2.5 References

1 M. K. Samantaray, E. Pump, A. Bendjeriou-Sedjerari, V. D'Elia, J. D. A. Pelletier, M. Guidotti, R. Psaro and J.-M. Basset, *Chem. Soc. Rev.*, 2018, **47**, 8403–8437.

2 C. Copéret, A. Comas-Vives, M. P. Conley, D. P. Estes, A. Fedorov, V. Mougel, H. Nagae, F. Núnez-Zarur and P. A. Zhizhko, *Chem. Rev.*, 2016, **116**, 323–421.

3 C. Copéret, F. Allouche, K. W. Chan, M. P. Conley, M. F. Delley, A. Fedorov, I. B. Moroz, V. Mougel, M. Pucino, K. Searles, K. Yamamoto and P. A. Zhizhko, *Angew. Chemie - Int. Ed. Ed.*, 2018, **57**, 6398–6440.

4 J. M. Thomas, R. Raja and D. W. Lewis, *Angew. Chemie - Int. Ed.*, 2005, **44**, 6456–6482.

5 B. Zhang, T. Fan, N. Xie, G. Nie and H. Zhang, *Adv. Sci.*, 2019, **6**, 1901787.

6 S. L. Suib, J. Přech, E. Szaniawska and J. Čejka, *Chem. Rev.*, 2023, **123**, 877–917.

7 M. Shamzhy, M. Opanasenko, P. Concepción and A. Martínez, *Chem. Soc. Rev.*, 2019, **48**, 1095–1149.

8 L. T. Zhuravlev, *Colloids Surfaces A Physicochem. Eng. Asp.*, 2000, **173**, 1–38.

9 A. Rimola, D. Costa, M. Sodupe, J. F. Lambert and P. Ugliengo, *Chem. Rev.*, 2013, **113**, 4216–4313.

10 Y. Ishizaka, N. Arai, K. Matsumoto, H. Nagashima, K. Takeuchi, N. Fukaya, H. Yasuda, K. Sato and J. Choi, *Chem. - A Eur. J.*, 2021, **27**, 12069–12077.

11 P. Li, G. Liu, H. Wu, Y. Liu, J. G. Jiang and P. Wu, *J. Phys. Chem. C*, 2011, **115**, 3663–3670.

12 W. N. P. Van Der Graaff, G. Li, B. Mezari, E. A. Pidko and E. J. M. Hensen, *ChemCatChem*, 2015, **7**, 1152–1160.

13 P. Peng, X.-H. Gao, Z.-F. Yan and S. Mintova, *Natl. Sci. Rev.*, 2020, **7**, 1726–1742.

14 N. Takahashi and K. Kuroda, *J. Mater. Chem.*, 2011, **21**, 14336–14353.

15 D. Sangian, Y. Ide, Y. Bando, A. E. Rowan and Y. Yamauchi, *Small*, 2018, **14**, 1800551.

16 N. Tsunoji, Y. Ide, Y. Yagenji, M. Sadakane and T. Sano, *ACS Appl. Mater. Interfaces*, 2014, **6**, 4616–4621.

17 E. Doustkhah, S. Rostamnia, N. Tsunoji, J. Henzie, T. Takei, Y. Yamauchi and Y. Ide, *Chem. Commun.*, 2018, **54**, 4402–4405.

18 M. Ogawa, S. Okutomo and K. Kuroda, *J. Am. Chem. Soc.*, 1998, **120**, 7361–7362.

19 Y. Ide, N. Kagawa, M. Sadakane and T. Sano, *Chem. Commun.*, 2013, **49**, 9027–9029.

20 Y. Asakura, Y. Sakamoto and K. Kuroda, *Chem. Mater.*, 2014, **26**, 3796–3803.

21 T. Yanagisawa, K. Kuroda and C. Kato, *Bull. Chem. Soc. Jpn.*, 1988, **61**, 3743–3745.

22 A. Shimojima, D. Mochizuki and K. Kuroda, *Chem. Mater.*, 2001, **13**, 3603–3609.

23 D. Mochizuki, A. Shimojima, T. Imagawa and K. Kuroda, *J. Am. Chem. Soc.*, 2005, **127**,

7183–7191.

24 Y. Asakura, Y. Matsuo, N. Takahashi and K. Kuroda, *Bull. Chem. Soc. Jpn.*, 2011, **84**, 968–975.

25 Y. Ide, G. Ozaki and M. Ogawa, *Langmuir*, 2009, **25**, 5276–5281.

26 T. Selvam, A. Inayat and W. Schwieger, *Dalton Trans.*, 2014, **43**, 10365–10387.

27 S. Osada, A. Iribe and K. Kuroda, *Chem. Lett.*, 2013, **42**, 80–82.

28 P. Loch, D. Schuchardt, G. Algara-Siller, P. Markus, K. Ottermann, S. Rosenfeldt, T. Lunkenbein, W. Schwieger, G. Papastavrou and J. Breu, *Sci. Adv.*, 2022, **8**, eabn9084.

29 N. Tsunoji, M. V. Opanasenko, M. Kubů, J. Čejka, H. Nishida, S. Hayakawa, Y. Ide, M. Sadakane and T. Sano, *ChemCatChem*, 2018, **10**, 2536–2540.

30 N. Tsunoji, H. Nishida, Y. Ide, K. Komaguchi, S. Hayakawa, Y. Yagenji, M. Sadakane and T. Sano, *ACS Catal.*, 2019, **9**, 5742–5751.

31 A. Corma, U. Díaz, V. Fornés, J. L. Jordá, M. Domine and F. Rey, *Chem. Commun.*, 1999, 779–780.

32 N. A. Grosso-Giordano, C. Schroeder, A. Okrut, A. Solovyov, C. Schöttle, W. Chassé, N. Marinković, H. Koller, S. I. Zones and A. Katz, *J. Am. Chem. Soc.*, 2018, **140**, 4956–4960.

33 C. Nédez, A. Theolier, F. Lefebvre, A. Choplin, J. M. Basset and J. F. Joly, *J. Am. Chem. Soc.*, 1993, **115**, 722–729.

34 A. Corma, M. T. Navarro and M. Renz, *J. Catal.*, 2003, **219**, 242–246.

35 L. Wang, J. Zhang, X. Wang, B. Zhang, W. Ji, X. Meng, J. Li, D. S. Su, X. Bao and F. S. Xiao, *J. Mater. Chem. A*, 2014, **2**, 3725–3729.

36 R. A. De Jesus, P. Da Conceição, J. P. V. Da Silva, N. S. Brainer, S. M. P. Meneghetti and M. R. Meneghetti, *J. Braz. Chem. Soc.*, 2019, **30**, 1976–1987.

37 X. X. Wang, L. Veyre, F. Lefebvre, J. Patarin and J. M. Basset, *Microporous Mesoporous Mater.*, 2003, **66**, 169–179.

38 A. Saidi, W. Al Maksoud, M. K. Samantaray, E. Abou-Hamad and J. M. Basset, *Chem. Commun.*, 2020, **56**, 13401–13404.

39 P. Ferrini, J. Dijkmans, R. De Clercq, S. Van de Vyver, M. Dusselier, P. A. Jacobs and B. F. Sels, *Coord. Chem. Rev.*, 2017, **343**, 220–255.

40 J. Cervantes, R. Zárraga and C. Salazar-Hernández, *Appl. Organomet. Chem.*, 2012, **26**, 157–163.

41 M. Aresta, A. Dibenedetto, F. Nocito and C. Pastore, *J. Mol. Catal. A Chem.*, 2006, **257**, 149–153.

42 J. George, Y. Patel, S. M. Pillai and P. Munshi, *J. Mol. Catal. A Chem.*, 2009, **304**, 1–7.

43 N. Rabiee, M. Safarkhani and M. M. Amini, *Rev. Inorg. Chem.*, 2019, **39**, 13–45.

44 B. Tang, W. Dai, G. Wu, N. Guan, L. Li and M. Hunger, *ACS Catal.*, 2014, **4**, 2801–2810.

45 D. Mochizuki, S. Kowata and K. Kuroda, *Chem. Mater.*, 2006, **18**, 5223–5229.

46 M. Yatomi, M. Koike, N. Rey, Y. Murakami, S. Saito, H. Wada, A. Shimojima, D. Portehault, S. Carenco, C. Sanchez, C. Carcel, M. Wong Chi Man and K. Kuroda, *Eur. J. Inorg. Chem.*, 2021, **2021**, 1836–1845.

47 M. Borowski, O. Kovalev and H. Gies, *Microporous Mesoporous Mater.*, 2008, **107**, 71–80.

48 S. Kiba, T. Itagaki, T. Nakato and K. Kuroda, *J. Mater. Chem.*, 2010, **20**, 3202–3210.

49 T. Uruga, H. Tanida, Y. Yoneda, K. Takeshita, S. Emura, M. Takahashi, M. Harada, Y. Nishihata, Y. Kubozono, T. Tanaka, T. Yamamoto, H. Maeda, O. Kamishima, Y. Takabayashi, Y. Nakata, H. Kimura, S. Goto and T. Ishikawa, *J. Synchrotron Radiat.*, 1999, **6**, 143–145.

50 H. Asakura, S. Yamazoe, T. Misumi, A. Fujita, T. Tsukuda and T. Tanaka, *Radiat. Phys. Chem.*, 2020, **175**, 108270.

51 A. L. Ankudinov, B. Ravel, J. J. Rehr and S. D. Conradson, *Phys. Rev. B*, 1998, **58**, 7565–7576.

52 J. P. Perdew, K. Burke and M. Ernzerhof, *Phys. Rev. Lett.*, 1996, **77**, 3865–3868.

53 K. Momma and F. Izumi, *J. Appl. Crystallogr.*, 2011, **44**, 1272–1276.

54 C. Bisio, F. Carniato, G. Paul, G. Gatti, E. Boccaleri and L. Marchese, *Langmuir*, 2011, **27**, 7250–7257.

55 T. D. Courtney, C. C. Chang, R. J. Gorte, R. F. Lobo, W. Fan and V. Nikolakis, *Microporous Mesoporous Mater.*, 2015, **210**, 69–76.

56 B. B. Kharkov and S. V. Dvinskikh, *J. Phys. Chem. C*, 2013, **117**, 24511–24517.

57 W. Dai, Q. Lei, G. Wu, N. Guan, M. Hunger and L. Li, *ACS Catal.*, 2020, **10**, 14135–14146.

58 T. Tanaka, Y. Matsumura, R. Okawara, Y. Musya and S. Kinumaki, *Bull. Chem. Soc. Jpn.*, 1968, **41**, 1497–1501.

59 L. Pellerito, G. Dia, A. Gianguzza, M. A. Girasolo, E. Rizzarelli and R. Purrello, *Polyhedron*, 1987, **6**, 1639–1645.

60 M. C. Tobin, *J. Mol. Spectrosc.*, 1961, **5**, 65–71.

61 C. Zhang, Z. Ren, Z. Yin, L. Jiang and S. Fang, *Spectrochim. Acta Part A Mol. Biomol. Spectrosc.*, 2011, **81**, 598–603.

62 M. Koike, Y. Asakura, Y. Kuroda, H. Wada, A. Shimojima and K. Kuroda, *Clay Sci.*, 2018, **22**, 1–11.

63 M. Gopalakrishnan and N. Palanisami, *RSC Adv.*, 2016, **6**, 1760–1768.

64 G. Borbély, H. G. Karge, W. Schwieger, A. Brandt and K.-H. Bergk, *Clays Clay Miner.*, 1991, **39**, 490–497.

65 Y. Matsubara, W. Konishi, T. Sugizaki and O. Moriya, *J. Polym. Sci. Part A Polym. Chem.*, 2001, **39**, 2125–2133.

66 J. Beckmann and K. Jurkschat, *Coord. Chem. Rev.*, 2001, **215**, 267–300.

67 J. Dijkmans, M. Dusselier, W. Janssens, M. Trekels, A. Vantomme, E. Breynaert, C. Kirschhock and B. F. Sels, *ACS Catal.*, 2016, **6**, 31–46.

68 J. Dijkmans, J. Demol, K. Houthoofd, S. Huang, Y. Pontikes and B. Sels, *J. Catal.*, 2015, **330**, 545–557.

69 J. D. Koch, J. Gronki and R. K. Hanson, *J. Quant. Spectrosc. Radiat. Transf.*, 2008, **109**, 2037–2044.

70 J. Dijkmans, M. Dusselier, D. Gabriëls, K. Houthoofd, P. C. M. M. Magusin, S. Huang, Y. Pontikes, M. Trekels, A. Vantomme, L. Giebeler, S. Oswald and B. F. Sels, *ACS Catal.*, 2015, **5**, 928–940.

71 M. Sun, Y. Su, C. Du, Q. Zhao and Z. Liu, *RSC Adv.*, 2014, **4**, 30820–30827.

72 R. Okawara, *Proc. Chem. Soc.*, 1964, 383.

73 R. K. Harris and A. Sebald, *J. Organomet. Chem.*, 1987, **331**, C9–C12.

74 S. R. Bare, S. D. Kelly, W. Sinkler, J. J. Low, F. S. Modica, S. Valencia, A. Corma and L. T. Nemeth, *J. Am. Chem. Soc.*, 2005, **127**, 12924–12932.

75 A. Al-Nayili, K. Yakabi and C. Hammond, *J. Mater. Chem. A*, 2016, **4**, 1373–1382.

76 T. Hara, M. Hatakeyama, A. Kim, N. Ichikuni and S. Shimazu, *Green Chem.*, 2012, **14**, 771–777.

Chapter 3

Swelling Ability and Lewis Acidity of Layered Octosilicate Modified with Isolated Dialkyltin Species

The major part of this chapter was adapted with permission from M. Yatomi, K. Kuroda, A. Shimojima, “Swelling Ability and Lewis Acidity of Layered Octosilicate Modified with Isolated Dialkyltin Species”, *Chem. Lett.*, **2024**, in press (doi:10.1093/chemle/upae020).

3.1 Introduction

Silica-supported isolated metal species are attractive materials as catalysts for various reactions.[1–4] Precise control of the local structure and distribution of metal species, as well as an increase in their loading amounts, are required to improve the catalytic activity.[5,6] The silanol (SiOH) groups on silica surfaces react with metallic reagents such as metal alkoxides, metal chlorides, and transition metal alkyl complexes, leading to the immobilization of isolated metal species via Si–O–M (M = metal) bonds. High silanol density and high specific surface area of silica supports contribute to the increase in the metal content per weight. Furthermore, the crystallinity defines the structure and arrangement of the surface SiOH groups, resulting in controlling the local structure and distribution of immobilized metal species on the supports.

Layered silicates are promising materials as a support of single metal catalysts owing to the crystalline two-dimensional (2D) nanosheets consisting of SiO_4 tetrahedral units. The SiOH and silanolate (SiO^-) groups are regularly arranged on the layer surfaces, and exchangeable cationic species are present between the layers. The interlayer SiOH/SiO^- groups of layered silicates can be functionalized through silylation reactions.[7–14] The utilization of layered silicates as a support for isolated metal species has also been reported.[15–18] Ensuring interlayer accessibility is a significant issue for applications in adsorption and catalysis. Tsunoji *et al.* incorporated Ti species into interlayer-expanded layered silicates HUS-2 and HUS-7 with alkyltrimethylammonium cations and investigated their catalytic activity.[15–17] The interlayer accessibility of the substrates was improved by remaining alkylammonium cations after reacting HUS-7 with titanium(IV) acetylacetonate.[16] However, the layer spacing decreased after the catalytic reaction, indicating desorption of the interlayer alkylammonium cations.

Recently, the immobilization of dimethyltin species on the layer surfaces of layered octosilicate was reported to demonstrate the controllable reactivity of organotin species as a metal precursor.[18] Na-type layered octosilicate (RUB-18, Ilerite, $Na_8Si_{32}O_{64}(OH)_8 \cdot 32H_2O$, named as Na-Oct) is a type of layered silicate with confronting SiOH/SiO^- groups on the surfaces.[19,20] Alkyltin chlorides have highly reactive Sn–Cl groups and relatively stable Sn–R (R = alkyl) groups; therefore, bidentate dimethyltin groups were successfully formed on the layer surfaces using dimethyltin dichloride. The products are potentially used as a solid acid catalyst because tetravalent alkyltin compounds exhibit Lewis acidity upon introducing electron-withdrawing substituents on Sn.[21,22] However, the interlayer spaces modified with dimethyltin groups are very narrow, limiting the interlayer accessibility of the substrates and the assessment of the acidity of the Sn sites.

In this study, the interlayer accessibility and the acidity of layered octosilicate immobilized with well-defined isolated longer dialkyltin species are investigated. Dibutyltin dichloride (Bu_2SnCl_2) is a bifunctional alkyltin compound similar to dimethyltin dichloride. The longer alkyl groups bonded to Sn are expected to play a role in expanding the interlayer spacing. First, layered octosilicate modified with dibutyltin species (Bu_2Sn-Oct) was synthesized by the reaction between Bu_2SnCl_2 and layered octosilicate interlayer-expanded with cetyltrimethylammonium (C_{16}TMA) cations (C_{16}TMA-Oct, Scheme 3.1). Next, the difference in the interlayer swelling ability between Bu_2Sn-Oct and the previously reported dimethyltin-modified octosilicate[18] was investigated. Furthermore, the interlayer acidity was investigated by solid-state ^{31}P NMR measurements using trimethylphosphine oxide (TMPO) as a probe molecule.

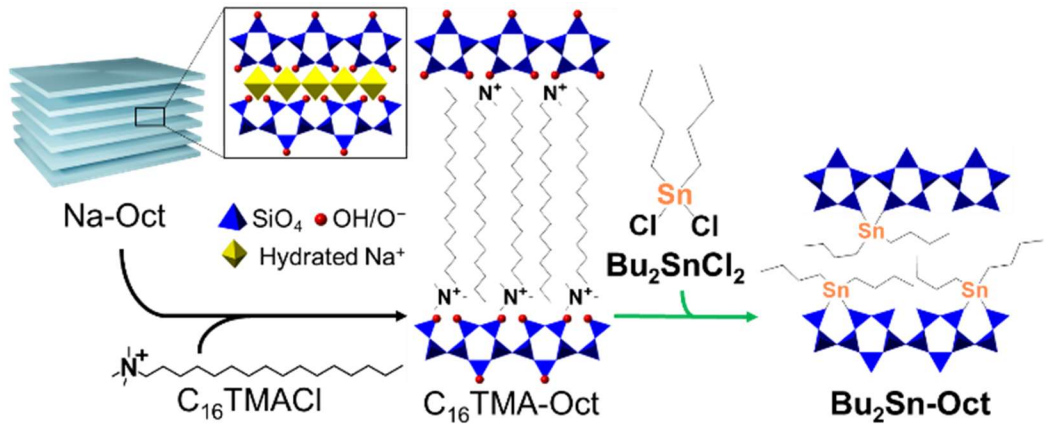

Scheme 3.1 Interlayer modification of layered octosilicate using dibutyltin dichloride.

3.2 Experimental Methods

3.2.1 Materials

SiO_2 (fumed silica (S5130)) was purchased from Sigma Aldrich. NaOH (97%), trimethylphosphine oxide (TMPO, 97%), *N,N*-dimethylformamide (DMF, super dehydrated, 99.5%), dichloromethane (DCM, super dehydrated, 99.5%), and *N*-methylformamide (NMF, 99.0%) were purchased from FUJIFILM Wako Pure Chemical Corp. Hexadecyltrimethylammonium chloride (C_{16}TMACl, 95%), dibutyltin dichloride (Bu_2SnCl_2, 97%), and dimethyltin oxide (DMTO, 95%) were purchased from Tokyo Chemical Ind. Co., Ltd. Acetone (99.0%) was purchased from Kanto Chemical Co., Inc. All the reagents were used without further purification.

A DMF solution of Bu_2SnCl_2 (0.82 M in super dehydrated DMF) was prepared in a glove box filled with nitrogen gas and was used for the reaction with C_{16}TMA-Oct. A DCM solution of TMPO (0.1 M in super dehydrated DCM) was also prepared in a glove box filled with nitrogen gas.

3.2.2 Preparation of layered Na-octosilicate and ion-exchange with C_{16}TMACl

Na-Oct and hexadecyltrimethylammonium ion-exchanged octosilicate (C_{16}TMA-Oct) were synthesized following the previous reports.[14,23] Fumed silica, NaOH, and deionized water were mixed at a molar ratio of 4:1:25.8 in a Teflon beaker, and the mixture was aged at room temperature for 1 h. Hydrothermal treatment was conducted in a Teflon-sealed autoclave at 100 °C for 4 w. The product was washed with deionized water and air-dried at 45 °C to obtain Na-Oct. Na-Oct (1.5 g) was dispersed in 100 mL of 0.1 M aqueous solution of C_{16}TMACl and stirred at room temperature for 24 h. After

centrifuging the suspension, the precipitate was washed twice with deionized water. Finally, the product was vacuum-dried at room temperature to obtain C_{16}TMA-Oct.

3.2.3 Immobilization of dibutyltin dichloride on C_{16}TMA-Oct

C_{16}TMA-Oct (0.2 g) was dried in a Schlenk flask by vacuum heating at 120 °C for 3 h. After cooling to 100 °C and introducing dried N_2, DMF (5.5 mL) and a 0.82 M DMF solution of Bu_2SnCl_2 (4.5 mL) were added, and the mixture was stirred at 100 °C for 2 d. Bu_2SnCl_2 was added in an amount of 10 molar equivalents relative to a pair of reaction sites ($SiOH/SiO^-$) on the octosilicate surface. The product was separated by centrifugation (5000 rpm, 5 min), washed three times with acetone, and dried overnight under reduced pressure. The sample was named Bu_2Sn-Oct.

3.2.4 NMF-treatment of the dialkyltin-grafted octosilicate.

Dialkyltin-grafted octosilicate, Me_2Sn-Oct and Bu_2Sn-Oct, were treated with NMF under ultrasonication for 30 min. After aging for 2 d, the precipitated slurry was collected, and the X-ray diffraction (XRD) measurements were performed without drying.

3.2.5 Adsorption of TMPO to the dialkyltin-grafted octosilicate.

Me_2Sn-Oct and Bu_2Sn-Oct were dehydrated at 100 °C for 2 d under vacuum in Schlenk flasks. After placing the flasks in a glove box under a nitrogen atmosphere, 0.1 M DCM solution of TMPO (an equivalent amount to Sn) was added. After ultrasonication for 30 min, the solvent was removed under vacuum. The resulting powder was packed into a solid-state NMR sample tube in a glove box. The powder XRD measurements were performed immediately after the ^{31}P MAS NMR measurements.

3.2.6 Characterization

XRD patterns were performed by a parallel method using a Rigaku RINT-Ultima III powder diffractometer (Cu Kα, λ = 0.15418 nm, 40 kV, 40 mA), a Rigaku Ultima IV diffractometer (Fe Kα, λ = 0.19373 nm, 40 kV, 30 mA), and a Rigaku SmartLab (Cu Kα, λ = 0.15418 nm, 40 kV, 30 mA). Fourier transform infrared (FT-IR) spectra were recorded by a KBr method on a JASCO FT/IR-6100 spectrometer. Solid-state NMR spectra were obtained using a JEOL ECX-400 spectrometer. Samples were packed in 4 mm zirconia sample tubes and spun at 6 kHz (^{13}C and ^{29}Si) and 10 kHz (^{31}P). ^{13}C cross-polarization (CP)/magic-angle spinning (MAS) NMR was measured at a resonance frequency of 99.6 MHz with a recycle delay of 10 s and contact time of 5 ms. ^{29}Si MAS NMR was measured at a resonance frequency of 78.6 MHz, with a 90° pulse and a recycle delay of 500 s. ^{31}P MAS NMR was measured at a resonance frequency of 160.3 MHz, with a 45° pulse and a recycle delay of 10 s. Chemical shifts for ^{13}C, ^{29}Si, and ^{31}P nuclei were referenced to hexamethylbenzene ($\underline{\mathbf{C}}H_3$) at 17.4 ppm, polydimethylsilane at −33.8 ppm, and triphenylphosphine at −8.4 ppm, respectively, as external standards. Carbon, hydrogen, and nitrogen (CHN) contents were obtained using a Yanaco CHN Corder (MT-5). The heating and oxidation temperatures (conc. 15% O_2) and temperature at the reduction furnaces were 950, 850, and 550 °C, respectively. CHN analysis was conducted by A-Rabbit-Science Japan Co., Ltd. Silicon and tin contents were obtained using inductively coupled plasma optical emission spectrometry (ICP-OES) (Agilent Technologies, Agilent 5100). Samples were prepared by a melting method with $Li_2B_4O_7$ as the flux. High-resolution scanning electron microscopy (HR-SEM) images were obtained using an S-5500 microscope (Hitachi High Technologies Co.) at an accelerating voltage of 1 kV.

Transmission electron microscopy (TEM), high-angle annular dark-field scanning transmission electron microscopy (HAADF-STEM), and energy dispersive X-ray spectroscopy (EDS) analyses were performed on a JEOL JEM-1400Flash microscope at an accelerating voltage of 120 kV. STEM-EDS mapping images were observed on a JEOL JED-2300T detector. The diffuse reflectance (DR) UV–Vis spectra were measured using a V-660 spectrometer (JASCO) with a $BaSO_4$ plate as the reference. Sn K-edge X-ray absorption fine structure (XAFS) analyses were conducted at the public beamline BL01B1 of SPring-8 at JASRI.[24] The incident X-rays were monochromatized using a Si(311) double-crystal monochromator. The photon energy was calibrated at the inflection point of the Sn K-edge X-ray absorption near-edge structure (XANES) spectrum of the Sn metal foil to 29194.99 eV. The samples were diluted with an appropriate amount of boron nitride (BN), pressed into pellets, and used for XAFS measurement. Sn K-edge XAFS spectra were analyzed using xTunes software.[25] After normalization, Fourier-transformation of k^3-weighted χ spectra in the k range of 3.0–14.0 $Å^{-1}$ was performed to obtain the FT-EXAFS spectra. The curve fitting analysis was conducted in the 1.2–1.9 Å range using a FEFF8 program.[26] The partial structural models were displayed using the VESTA software.[27]

3.3 Results and Discussion

3.3.1 Characterization of Bu_2Sn-Oct.

The powder XRD pattern of Bu_2Sn-Oct (Fig. 3.1(A)(b)) exhibited a diffraction peak corresponding to the basal spacing of d = 1.26 nm (2θ = 7.02°), which is shifted from that for C_{16}TMA-Oct (d = 2.79 nm, 2θ = 3.18°) (Fig. 3.1(A)(a)). The basal spacing of Bu_2Sn-Oct was slightly larger than that of dimethyltin-modified octosilicate (d = 1.18 nm),[18] which can be attributed to the longer but lying butyl groups. The in-plane peak for Bu_2Sn-Oct (Fig. 3.1(B)) was observed at 48.5° (d = 0.187 nm). The slightly larger d spacing than that for C_{16}TMA-Oct (2θ = 49.4°, d = 0.184 nm) suggested that in-plane lattice expansion of octosilicate occurred by the modification with the Sn species. Such a lattice expansion was observed upon grafting dimethyltin dichloride on layered octosilicate.[18]

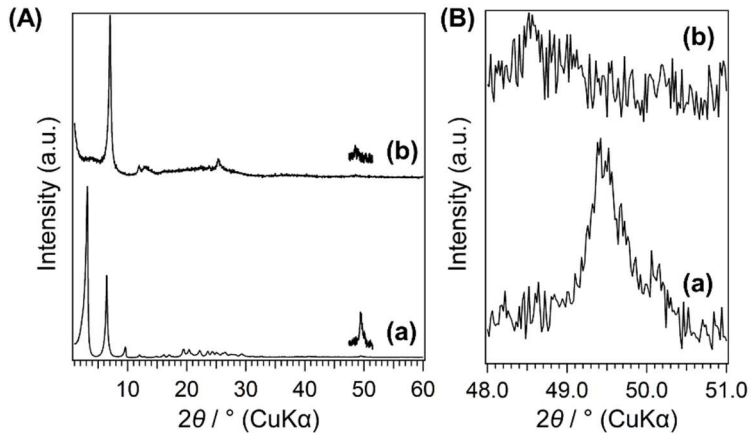

Fig. 3.1 Powder XRD patterns of (a) C_{16}TMA-Oct and (b) Bu_2Sn-Oct.

The FT-IR spectra of C_{16}TMA-Oct and Bu_2Sn-Oct were shown in Fig. 3.2(A). For C_{16}TMA-Oct (Fig. 3.2(A)(a)), the bands at 2950, 2920, 2870, and 2850 cm^{-1} were attributed to CH_3 asymmetric, CH_2 asymmetric, CH_3 symmetric, and CH_2 symmetric stretching vibrations of the alkyl groups, respectively.[28] A band at 960 cm^{-1} was attributed

to Si–OH stretching vibrations on the layer surface.[29] For Bu_2Sn-Oct (Fig. 3.2(A)(b)), the relative intensity of the C–H stretching vibration of the CH_2 groups to CH_3 groups decreased from that of $C_{16}TMA$-Oct, suggesting the elimination of $C_{16}TMA^+$ and introduction of a butyl group. Moreover, an absorption band at 560 cm^{-1} appeared, which was attributed to Sn–C stretching vibrations.[30–32] Furthermore, the band of Si–OH groups (960 cm^{-1}) decreased, suggesting that the reaction between SnCl and the SiOH groups occurred.

The ^{13}C CP/MAS NMR spectra of $C_{16}TMA$-Oct and Bu_2Sn-Oct were shown in Fig. 3.2(B). The signals observed for $C_{16}TMA$-Oct (Fig. 3.2(B)(a)) are consistent with the previous report.[14] For Bu_2Sn-Oct (Fig. 3.2(B)(b)), the signal at 14.8 ppm is asigned to the terminal methyl group of the dibutyltin group and the signal at 27.5 ppm is asigned to the methylene groups at the β- and γ-positions.[33] The methylene group at the α-position (–**C**H_2–Sn) corresponds to a shoulder signal around 22 ppm.[33] These results indicate the immobilization of butyltin groups on the layer surfaces.

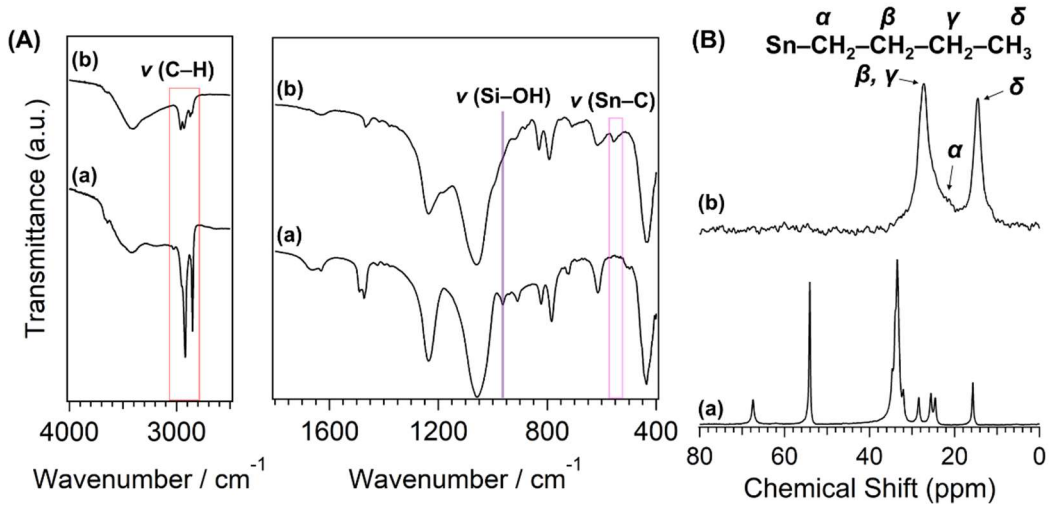

Fig. 3.2 (A) FT-IR spectra and (B) ^{13}C CP/MAS NMR spectra of (a) $C_{16}TMA$-Oct and (b) Bu_2Sn-Oct.

The elemental analysis (Table 3.1) quantitatively indicated the above reaction. The N/Si ratios of C_{16}TMA-Oct and Bu_2Sn-Oct were 0.26 to 0.01, indicating the elimination of C_{16}TMA cations by the reaction. In our previous report,[18] the dimethyltin-grafted octosilicate intercalated the reaction solvent (DMF) and the washing solvent (acetone), and removal of these solvents was difficult. In contrast, for Bu_2Sn-Oct, these solvent molecules were not observed by FT-IR and ^{13}C CP/MAS NMR. It is likely that the larger expansion of the layers by the butyl groups facilitated solvent removal from the interlayer by reduced pressure drying. The C/Sn ratio for Bu_2Sn-Oct was 8.2. Because residual organic solvents need not be considered, the organic contents of Bu_2Sn-Oct were derived from dibutyltin species. Therefore, the C/Sn ratio (8.2) is in good agreement with the two butyl groups bonded to one Sn species. The Sn/Si ratio of Bu_2Sn-Oct was 0.13, meaning that the degree of modification of confronting SiOH/SiO^- sites with Sn is 52% because the theoretical maximum Sn/Si ratio is 0.25.

Table 3.1 The contents of carbon, nitrogen, silicon, and tin.

Sample name	C / wt%	N / wt%	Si / wt%	Sn / wt%	N/Si ratio	Sn/Si ratio
C_{16}TMA-Oct	36.8	2.4	18.7	-	0.26	-
Bu_2Sn-Oct_10	12.9	0.1	27.7	15.6	0.01	0.13

The SEM, TEM, and HAADF-STEM images of Bu_2Sn-Oct (Figs. 3.3 (a)–(d)) exhibited a platelet morphology originating from octosilicate. HAADF-STEM-EDS analysis revealed the uniform distribution of Sn on Si (Figs. 3.3 (e) and (f)), suggesting that Sn species were grafted throughout the interlayer surfaces of the silicate layers. In addition, a small amount of extra-framework species was observed in some parts (pink

circles in Fig. 3.3), which was probably due to hydrolytic polycondensation of Bu_2SnCl_2 by moisture in the air.

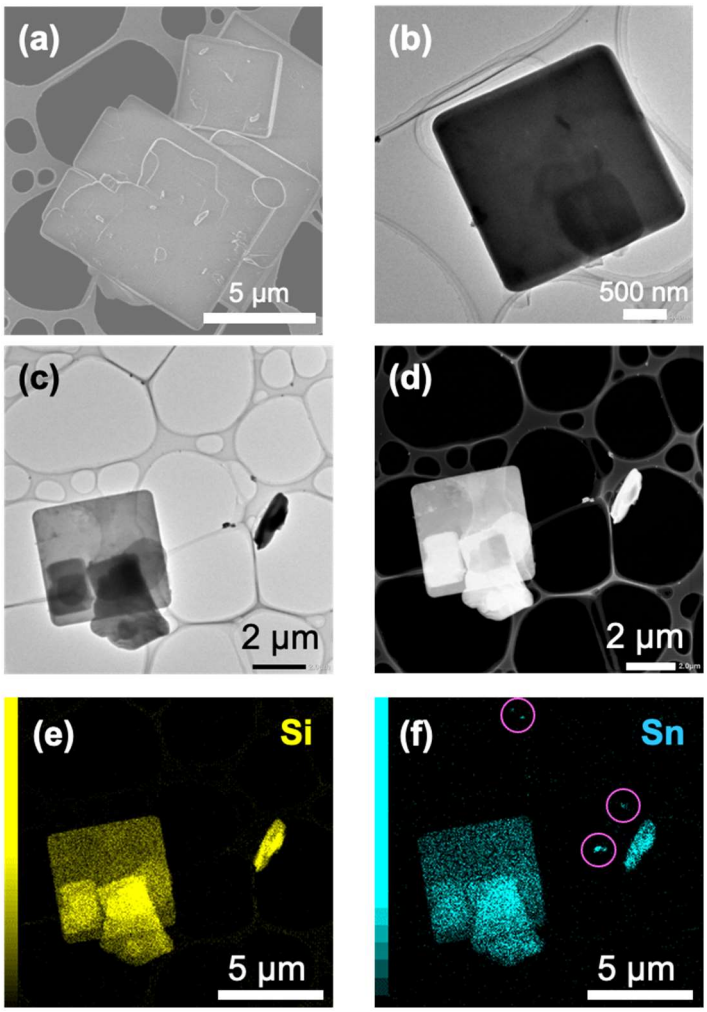

Fig. 3.3 Electron microscopy images of Bu_2Sn-Oct. (a) TEM image, (b)HAADF-STEM image, and (c)(d) EDS mapping images (Si is colored yellow, and Sn is colored blue.). The pink circled areas are condensed Bu_2SnCl_2 because only Sn is observed.

The ^{29}Si MAS NMR spectra of $C_{16}TMA$-Oct and Bu_2Sn-Oct were shown in Fig. 3.4(C). $C_{16}TMA$-Oct exhibited two signals at −100 ppm and −111 ppm with an integral intensity ratio of 1 : 1 (Fig. 3.4 (C)(a)), which are attributed to Q^3 ($\underline{\mathbf{Si}}(OSi)_3OH/O^-$) and Q^4 ($\underline{\mathbf{Si}}(OSi)_4$) sites, respectively.[23] For Bu_2Sn-Oct (Fig.3.4(C)(b)), the original Q^3 signal disappeared, and signals were observed at −103 ppm, −107 ppm, and −110 ppm with the

integral intensity ratio of 0.50 : 0.51 : 1.00. The signals at −103 ppm and −107 ppm were assigned to the confronting disilanol sites (**Si**$(OSi)_3OH$) and the dibutyltin-modified sites (**Si**$(OSi)_3OSn$), respectively.[18] Therefore, because the integral intensity ratio (0.51) of the signal at −107 ppm corresponds to the ratio of Si forming Sn–O–Si bonds out of Q^3 sites, the degree of modification with Sn for Bu_2Sn-Oct can be calculated to be 51%. Combining the solid-state ^{29}Si NMR results and the Sn/Si ratio (0.13) based on elemental analysis, the ratio of Sn, disilanol sites, dibutyltin-modified sites, and Q^4 unit is 0.26 : 0.50 : 0.51 : 1.00. Therefore, the ratio of the Sn to Si bonded with Sn is approximately 1 : 2, suggesting the bidentate immobilization of the dibutyltin groups.

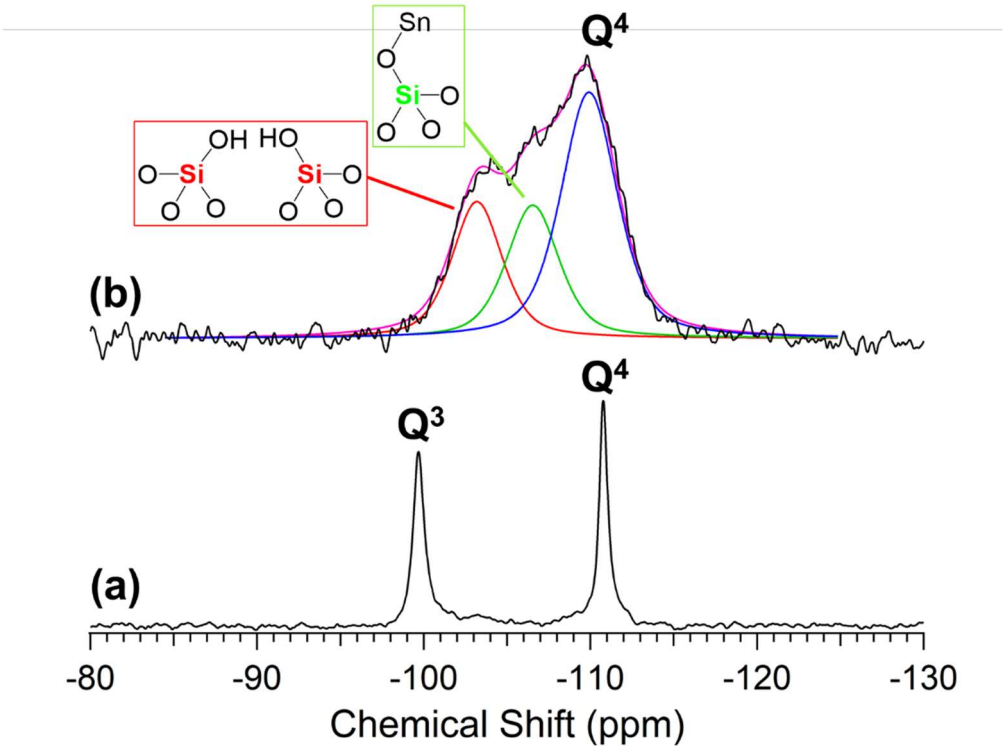

Fig. 3.4 ^{29}Si MAS NMR spectra of (a) C_{16}TMA-Oct and (b) Bu_2Sn-Oct. Black lines are original spectra, pink lines are fitting spectra, red lines indicate Q^a signal at −103 ppm, green lines indicate Q^b signal at −107 ppm, and blue lines indicate Q^4 signal at −110 ppm.

For the determination of the local structure of Sn in Bu_2Sn-Oct, DR UV–Vis and XAFS measurements were performed. The DR UV–Vis spectrum (Fig. 3.5(A)) showed a shoulder band at 220 nm, which was attributed to O→Sn LMCT (ligand to metal charge transfer), also observed for dimethyltin-modified octosilicate and tin-containing silica-based materials.[34–37] The absorption band at nearly 300 nm suggested the presence of extra-framework dibutyltin oxide species. This is considered to correspond to the externally precipitated Sn species observed by the electron microscopy. The degree of Sn-modification calculated from elemental analysis and solid-state ^{29}Si NMR are in good agreement, which indicates that the externally precipitated Sn species are present in only a small amount.

The Sn K-edge FT-EXAFS spectrum of Bu_2Sn-Oct (Fig. 3.5(B)) exhibited two peaks derived from the first and second coordination spheres. The curve fitting of these peaks gave the coordination number, bond distances, and Debye-Waller factor (Table 3.2). The curve fitting results for Sn–O (C) scattering of Bu_2Sn-Oct showed the presence of four-coordinated Sn species with a distance of 2.01 Å. Because the presence of two butyl groups for Sn was confirmed by the elemental analysis, the formation of bidentate dibutyltin groups on the surface of octosilicate is strongly suggested. Moreover, a slight Sn–Sn scattering peak also appeared in the second coordination sphere, which probably originated from the extra-framework species observed by electron microscopy (Fig. 3.3). Thus, the bidentate dibutyltin groups grafted to the interlayer surface of layered octosilicate were identified.

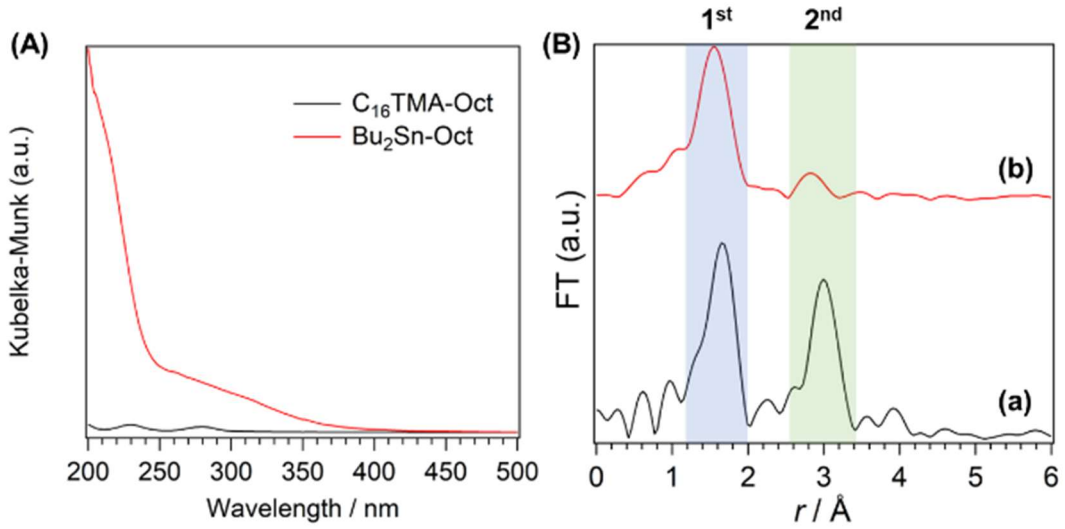

Fig. 3.5 (A) DR UV–Vis spectra of C_{16}TMA-Oct and Bu_2Sn-Oct. (B) FT-EXAFS spectra of (a) DMTO and (b) Bu_2Sn-Oct.

Table 3.2 Structural parameters of DMTO and Bu_2Sn-Oct obtained by curve-fitting analysis.

Samples	Path [a]	N [b]	*r* (Å) [c]	σ^2 (Å^2) [d]	R factor [e]
DMTO	Sn–O (C)	4.7 (2)	2.08 (3)	0.006 (3)	7.3
	Sn–Sn	2.6 (2)	3.27 (3)	0.005 (2)	8.7
Bu_2Sn-Oct	Sn–O (C)	3.9 (2)	2.01 (3)	0.007 (4)	8.1
	Sn–Sn	3.3 (6)	3.16 (8)	0.018 (12)	8.7

[a] Path denotes the scattering path of the photoelectrons included in the model. [b] N denotes the coordination number corresponding to the scattering path. [c] *r* denotes bond length. [d] σ^2 denotes the Debye-Waller factor. [e] R factor = $(\Sigma(k^3\chi^{data}(k) - k^3\chi^{fit}(k))^2)^{1/2}/(\Sigma(k^3\chi^{data}(k))^2)^{1/2}$.

3.3.2 Assessment of interlayer accessibility and acidity

To investigate the interlayer swelling ability of Me_2Sn-Oct and Bu_2Sn-Oct, ultrasonic treatment in NMF was performed. NMF is known to strongly interact with silanol groups on the layer surface because of its high polarity.[38] Fig. 3.6 shows the XRD patterns of the slurry obtained by the NMF treatment. For Me_2Sn-Oct, the basal spacing slightly increased from d = 1.11 nm to 1.15 nm, confirming that Me_2Sn-Oct could be slightly swelled by NMF. On the other hand, for Bu_2Sn-Oct, the d value significantly

increased from 1.28 nm to 1.73 nm, indicating its higher swelling ability. Thus, the swelling ability appears to be controlled by differences in the length of alkyl groups.

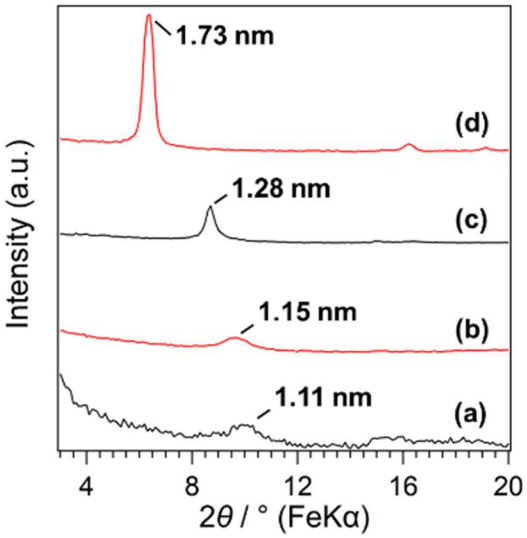

Fig. 3.6 XRD patterns of (a) Me_2Sn-Oct, (b) NMF-treated Me_2Sn-Oct, (c) Bu_2Sn-Oct, and (d) NMF-treated Bu_2Sn-Oct.

Trimethylphosphine oxide (TMPO) is a probe molecule used to evaluate the acidity of solid acid catalysts.[39,40] TMPO is adsorbed on the solid surface through the interaction between the oxygen of the P=O bond and the acid site. The acid sites can be characterized by investigating the phosphorus environment by ^{31}P MAS NMR measurements. Fig. 3.7(A) shows the ^{31}P MAS NMR spectra of TMPO-adsorbed Me_2Sn-Oct and Bu_2Sn-Oct. For Me_2Sn-Oct, a signal is observed at 46.1 ppm, which can be attributed to physisorbed TMPO.[41] On the other hand, for Bu_2Sn-Oct, three signals were observed at 46.2 ppm, 48.9 ppm, and 59.9 ppm. The former two signals are attributed to physisorbed TMPO,[41] suggesting two types of physisorption in two different environments: on the outer surface and between the layers. The latter signal (59.9 ppm) is generally interpreted as TMPO interacting with a Lewis acid site,[42] suggesting that the dibutyltin groups work as Lewis acid sites. Furthermore, in the powder XRD patterns of

TMPO-adsorbed samples (Fig. 3.7(B)), the basal spacing of Bu_2Sn-Oct partly increased by 0.3 nm after TMPO adsorption, whereas that of Me_2Sn-Oct was unchanged. Therefore, TMPO was intercalated between the layers of Bu_2Sn-Oct, indicating that the ^{31}P MAS NMR results reflect the interlayer environment. TMPO-adsorbed Bu_2Sn-Oct also exhibited the diffraction peak at $2\theta = 6.86°$ ($d = 1.29$ nm), suggesting that a part of layers was not expanded because of the low amount of TMPO. In summary, because Bu_2Sn-Oct has longer alkyl groups than Me_2Sn-Oct, the accessibility to the interlayer spaces increased, and the presence of Lewis acid sites on the layer surfaces was confirmed.

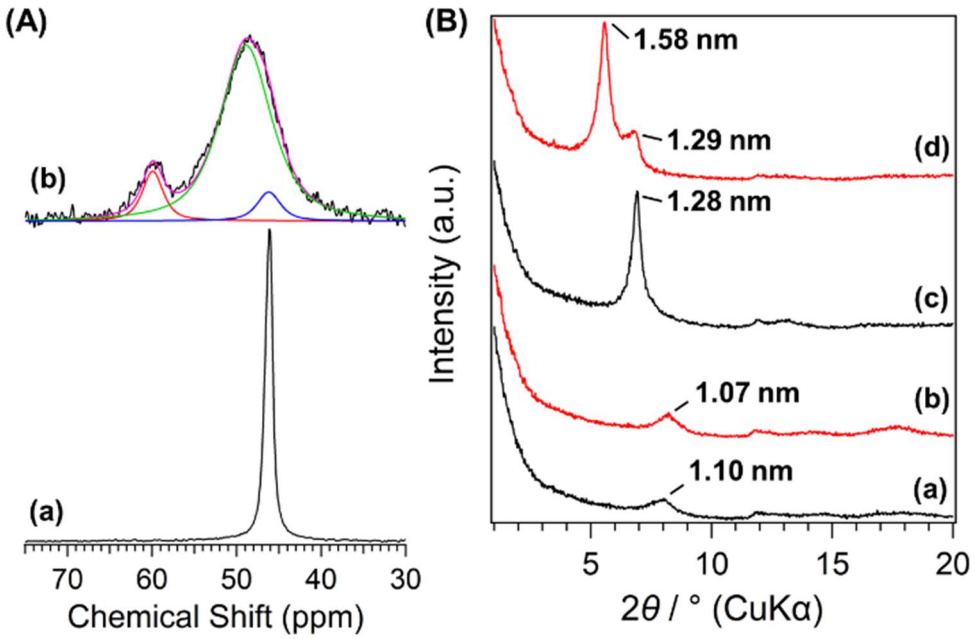

Fig. 3.7 (A) ^{31}P MAS NMR spectra of (a) TMPO-adsorbed Me_2Sn-Oct and (b) TMPO-adsorbed Bu_2Sn-Oct. (B) Powder XRD patterns of (a) Me_2Sn-Oct, (b) TMPO-adsorbed Me_2Sn-Oct, (c) Bu_2Sn-Oct, and (d) TMPO-adsorbed Bu_2Sn-Oct.

3.4 Conclusion

The interlayer modification of layered octosilicate with dibutyltin dichloride was performed. The dibutyltin groups were dipodally grafted to the surface confronting SiOH/SiO$^-$ groups, which was similar to dimethyltin-grafted octosilicate. Bu_2Sn-Oct exhibited the higher swelling ability with NMF compared with Me_2Sn-Oct. Furthermore, the presence of Lewis acid sites on the interlayer surfaces was indicated by the solid-state ^{31}P NMR of Bu_2Sn-Oct intercalated with TMPO. Overall, the dialkyltin compounds can be precisely immobilized on the interlayer surfaces of layered octosilicate. It is crucial to select the alkyl chain length to control the accessibility of the substrate to the interlayer spaces for catalytic reactions.

3.5 References

1 M. K. Samantaray, E. Pump, A. Bendjeriou-Sedjerari, V. D'Elia, J. D. A. Pelletier, M. Guidotti, R. Psaro and J.-M. Basset, *Chem. Soc. Rev.*, 2018, **47**, 8403–8437.

2 C. Copéret, A. Comas-Vives, M. P. Conley, D. P. Estes, A. Fedorov, V. Mougel, H. Nagae, F. Núnez-Zarur and P. A. Zhizhko, *Chem. Rev.*, 2016, **116**, 323–421.

3 L. Liu and A. Corma, *Chem. Rev.*, 2018, **118**, 4981–5079.

4 S. L. Suib, J. Přech, E. Szaniawska and J. Čejka, *Chem. Rev.*, 2023, **123**, 877–917.

5 J. M. Thomas, R. Raja and D. W. Lewis, *Angew. Chemie - Int. Ed.*, 2005, **44**, 6456–6482.

6 B. Zhang, T. Fan, N. Xie, G. Nie and H. Zhang, *Adv. Sci.*, 2019, **6**, 1901787.

7 N. Takahashi and K. Kuroda, *J. Mater. Chem.*, 2011, **21**, 14336–14353.

8 E. Ruiz-Hitzky and J. M. Rojo, *Nature*, 1980, **287**, 28–30.

9 T. Yanagisawa, K. Kuroda and C. Kato, *Bull. Chem. Soc. Jpn.*, 1988, **61**, 3743–3745.

10 D. Mochizuki, A. Shimojima and K. Kuroda, *J. Am. Chem. Soc.*, 2002, **124**, 12082–12083.

11 I. Fujita, K. Kuroda and M. Ogawa, *Chem. Mater.*, 2003, **15**, 3134–3141.

12 Y. Ide and M. Ogawa, *Bull. Chem. Soc. Jpn.*, 2007, **80**, 1624–1629.

13 K. Park, J. Hwa, S. Kim and O. Kwon, *Appl. Clay Sci.*, 2009, **46**, 251–254.

14 M. Yatomi, M. Koike, N. Rey, Y. Murakami, S. Saito, H. Wada, A. Shimojima, D. Portehault, S. Carenco, C. Sanchez, C. Carcel, M. Wong Chi Man and K. Kuroda, *Eur. J.*

Inorg. Chem., 2021, **2021**, 1836–1845.

15 N. Tsunoji, Y. Ide, Y. Yagenji, M. Sadakane and T. Sano, *ACS Appl. Mater. Interfaces*, 2014, **6**, 4616–4621.

16 N. Tsunoji, M. V. Opanasenko, M. Kubů, J. Čejka, H. Nishida, S. Hayakawa, Y. Ide, M. Sadakane and T. Sano, *ChemCatChem*, 2018, **10**, 2536–2540.

17 N. Tsunoji, H. Nishida, Y. Ide, K. Komaguchi, S. Hayakawa, Y. Yagenji, M. Sadakane and T. Sano, *ACS Catal.*, 2019, **9**, 5742–5751.

18 M. Yatomi, T. Hikino, S. Yamazoe, K. Kuroda and A. Shimojima, *Dalton Trans.*, 2023, **52**, 18158–18167.

19 S. Vortmann, J. Rius, S. Siegmann and H. Gies, *J. Phys. Chem. B*, 1997, **101**, 1292–1297.

20 I. Wolf, H. Gies and C. A. Fyfe, *J. Phys. Chem. B*, 1999, **103**, 5933–5938.

21 J. Cervantes, R. Zárraga and C. Salazar-Hernández, *Appl. Organomet. Chem.*, 2012, **26**, 157–163.

22 N. Rabiee, M. Safarkhani and M. M. Amini, *Rev. Inorg. Chem.*, 2019, **39**, 13–45.

23 D. Mochizuki, S. Kowata and K. Kuroda, *Chem. Mater.*, 2006, **18**, 5223–5229.

24 T. Uruga, H. Tanida, Y. Yoneda, K. Takeshita, S. Emura, M. Takahashi, M. Harada, Y. Nishihata, Y. Kubozono, T. Tanaka, T. Yamamoto, H. Maeda, O. Kamishima, Y. Takabayashi, Y. Nakata, H. Kimura, S. Goto and T. Ishikawa, *J. Synchrotron Radiat.*, 1999, **6**, 143–145.

25 H. Asakura, S. Yamazoe, T. Misumi, A. Fujita, T. Tsukuda and T. Tanaka, *Radiat. Phys. Chem.*, 2020, **175**, 108270.

26 A. L. Ankudinov, B. Ravel, J. J. Rehr and S. D. Conradson, *Phys. Rev. B*, 1998, **58**, 7565–7576.

27 K. Momma and F. Izumi, *J. Appl. Crystallogr.*, 2011, **44**, 1272–1276.

28 C. Bisio, F. Carniato, G. Paul, G. Gatti, E. Boccaleri and L. Marchese, *Langmuir*, 2011, **27**, 7250–7257.

29 T. D. Courtney, C. C. Chang, R. J. Gorte, R. F. Lobo, W. Fan and V. Nikolakis, *Microporous Mesoporous Mater.*, 2015, **210**, 69–76.

30 T. Tanaka, Y. Matsumura, R. Okawara, Y. Musya and S. Kinumaki, *Bull. Chem. Soc. Jpn.*, 1968, **41**, 1497–1501.

31 L. Pellerito, G. Dia, A. Gianguzza, M. A. Girasolo, E. Rizzarelli and R. Purrello, *Polyhedron*, 1987, **6**, 1639–1645.

32 M. C. Tobin, *J. Mol. Spectrosc.*, 1961, **5**, 65–71.

33 P. G. Sutton, C. F. Harrington, B. Fairman, E. Hywel Evans, L. Ebdon and T. Catterick, *Appl. Organomet. Chem.*, 2000, **14**, 691–700.

34 J. Dijkmans, M. Dusselier, W. Janssens, M. Trekels, A. Vantomme, E. Breynaert, C. Kirschhock and B. F. Sels, *ACS Catal.*, 2016, **6**, 31–46.

35 H. Joshi, C. Ochoa-Hernández, E. Nürenberg, L. Kang, F. R. Wang, C. Weidenthaler, W. Schmidt and F. Schüth, *Microporous Mesoporous Mater.*, 2020, **309**, 110566.

36 J. Dijkmans, M. Dusselier, D. Gabriëls, K. Houthoofd, P. C. M. M. Magusin, S. Huang, Y. Pontikes, M. Trekels, A. Vantomme, L. Giebeler, S. Oswald and B. F. Sels, *ACS Catal.*, 2015, **5**, 928–940.

37 S.-Q. He, J. Wang, D.-D. Wu, X.-J. Sang, F. Su, Z.-M. Zhu and L.-C. Zhang, *J. Mater. Sci.*, 2019, **54**, 4601–4618.

38 Y. Asakura, S. Osada, N. Hosaka, T. Terasawa and K. Kuroda, *Dalton Trans.*, 2014, **43**, 10392–10395.

39 E. F. Rakiewicz, A. W. Peters, R. F. Wormsbecher, K. J. Sutovich and K. T. Mueller, *J. Phys. Chem. B*, 1998, **102**, 2890–2896.

40 A. Zheng, S. Bin Liu and F. Deng, *Chem. Rev.*, 2017, **117**, 12475–12531.

41 P. V. Wiper, J. Amelse and L. Mafra, *J. Catal.*, 2014, **316**, 240–250.

42 J. D. Lewis, M. Ha, H. Luo, A. Faucher, V. K. Michaelis and Y. Román-Leshkov, *ACS Catal.*, 2018, **8**, 3076–3086.

Chapter 4

Interlayer Silylation of Layered Octosilicate with Organoalkoxysilanes: Effects of Tetrabutylammonium Fluoride as a Catalyst and Functional Groups of Silanes

The major part of this chapter was adapted with permission from M. Yatomi, M. Koike, N. Rey, Y. Murakami, S. Saito, H. Wada, A. Shimojima, D. Portehault, S. Carenco, C. Sanchez, C. Carcel, M. Wong Chi Man, and K. Kuroda, "Interlayer Silylation of Layered Octosilicate with Organoalkoxysilanes: Effects of Tetrabutylammonium Fluoride as a Catalyst and the Functional Groups of Silanes", *Eur. J. Inorg. Chem.* **2021**, *2021*, 1836.

4.1 Introduction

Layered silicates, composed of 2D crystalline silicate layers, are promising inorganic materials with high versatility in terms of design.[1–6] They possess interlayer exchangeable cations and reactive SiO^-/SiOH groups. The ion-exchange property and reactivity of the interlayer surfaces provide a variety of silica-organic hybrid materials that can find various applications, such as ion exchange, adsorption, and catalysis.[1,7–9] The effective use of interlayer space is also important for designing layered silicates as 2D nanomaterials.[1,10,11] The interlayer modification of layered silicates with silylating agents is a practical method for increasing the chemical functionality of layered silicates. Indeed, various functional groups can be regularly grafted onto the surfaces of layered silicates by interlayer modification. Furthermore, this method enables the possibility to implement catalytic active sites, polymer growth sites, and porosity to layered silicates.[12–16] Thus, the regular interlayer modification of layered silicates with organic groups can maximize the advantages of silica-organic hybridization.[3]

The silylation of layered octosilicate, one of the layered silicates have been developed.[1] Layered octosilicate (Na-Oct (RUB-18): $Na_8[Si_{32}O_{64}(OH)_8]\cdot 32H_2O$)[17] possesses a pair of SiO^-/SiOH groups on the layer surfaces, as shown in Scheme 4.1 (a) and (b). In addition, the interlayer of octosilicate can be expanded by the introduction of organic species, such as alkyltrimethylammonium cations, between the layers. These expanded octosilicate can subsequently be reacted with di- or tri-functional organosilylating agents dipodally (bidentate silylation), resulting in the formation of silica-organic hybrid compounds with an ordered arrangement of organic groups.[1]

Organochlorosilanes and organoalkoxysilanes are two major silylating agents for layered silicates. Organochlorosilanes are highly reactive; they react with sufficiently

high yield with SiOH groups on the surfaces of silicate layers, affording a dense modification of the interlayer surfaces. However, the types of organic groups of organochlorosilanes are limited owing to the high reactivity of the Si–Cl bond towards organic functional groups. Furthermore, the generation of HCl produced by the reaction of chlorosilanes with silanol groups makes the reaction hard to control,[10,18] though this side effect is often reduced by using an HCl trapping agent (e.g., pyridine). In contrast, there is a greater variety of alkoxysilanes, and a wider range of organic modifications is possible. However, their reactivity towards silylation compared with organochlorosilanes is much lower. Therefore, the reactivity of organoalkoxysilanes for the silylation of silica and silicates must be substantially improved. The crucial factors affecting silylation reactions of layered silicates are thought to be the amount of silylating agent and the interlayer expansion with some intercalated species. Although these factors have been determined empirically from only few case studies,[18–20] a catalyst has scarcely been used for the silylation of layered silicates with organoalkoxysilanes. Kwon *et al.* reported the organosilylation of magadiite with octyltriethoxysilane[21] and that of kenyaite with 3-aminopropyltriethoxysilane[22] using a mixture of dodecylamine and ethanol. Although the catalytic action of dodecylamine was suggested, no details on the reaction mechanism were presented.

In this study, the effect of tetrabutylammonium fluoride (TBAF) on the silylation reactions of layered octosilicate with various organotriethoxysilanes (octyltriethoxysilane (C_8TES), propyltriethoxysilane (C_3TES), octadecyltriethoxysilane (C_{18}TES), and 3-mercaptopropyltriethoxysilane (MPTES)) was investigated (Scheme 4.1 (c) and Table 4.1). TBAF is often used as a catalyst of sol-gel reactions namely to favor condensation of alkoxysilanes. Indeed the fluoride ion of TBAF attacks the Si atom of alkoxysilanes,

forming hypervalent silicon intermediates, which increases the nucleophilicity of Si and hence the reactivity.[23–26] The degree of silylation of layered silicate using C_8TES was found to be increased in the presence of TBAF for the first time. The catalytic effect of TBAF on the silylation reaction was verified with other organoalkoxysilanes, confirming the superiority of this method. The accessibility of organosilylating agents between layers strongly influenced the degree of silylation of layered silicates with or without TBAF. Interestingly, the addition of TBAF was found to improve the degree of silylation for less accessible silylating agents.

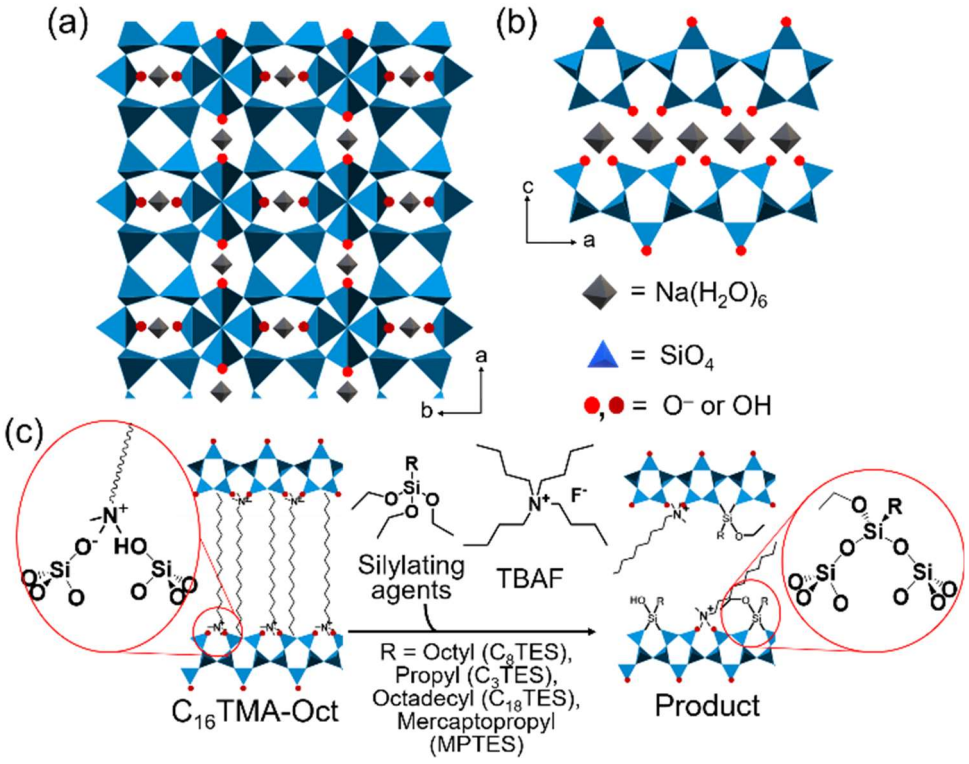

Scheme 4.1 (a) In-plane and (b) stacked structures of Na-Oct, and (c) dipodal silylation of C_{16}TMA-Oct.

Table 4.1 Experimental conditions

Sample name	Silylating agent	Solvent	Reaction temp. / °C	Reaction time / d	Molar ratio		
					$SiOH/SiO^{-}$ [a]	Silylating agent	TBAF
C_8-Oct	C_8TES	DMF	100	4	1	10	0
C_8-Oct_0.027F	C_8TES	DMF	100	4	1	10	0.027
C_8-Oct_0.27F	C_8TES	DMF	100	4	1	10	0.27
C_8-Oct_0.54F	C_8TES	DMF	100	4	1	10	0.54
C_3-Oct	C_3TES	DMF	100	4	1	10	0
C_3-Oct_0.27F	C_3TES	DMF	100	4	1	10	0.27
C_{18}-Oct	C_{18}TES	Toluene	80	4	1	10	0
C_{18}-Oct_0.27F	C_{18}TES	Toluene	80	4	1	10	0.27
MP-Oct	MPTES	DMF	100	4	1	10	0
MP-Oct_0.27F	MPTES	DMF	100	4	1	10	0.27

[a] A pair of $SiOH/SiO^{-}$ of C_{16}TMA-Oct corresponds to one reaction site because of dipodal silylation.

4.2 Experimental Methods

4.2.1 Materials

SiO_2 (fumed silica (S5130)), triblock copolymer EO20PO70EO20 (Pluronic 123), and tetrabutylammonium fluoride in tetrahydrofuran (1.0 M TBAF in THF) were purchased from Sigma Aldrich. NaOH (97%), hydrochloric acid (6 M), super dehydrated *N, N*-dimethylformamide (DMF, 99.5%), super dehydrated toluene (99.5%), and super dehydrated THF with stabilizer free (THF, 99.5%) were purchased from FUJIFILM Wako Pure Chemical Corporation. Hexadecyltrimethylammonium chloride (C_{16}TMACl, 95%), octyltriethoxysilane (97%), propyltriethoxysilane (98%), octadecyltriethoxysilane (85%), 3-mercaptopropyltriethoxysilane (96%), tetraethoxysilane (TEOS)were purchased from Tokyo Chemical Industry Co., Ltd. Acetone (99.0%) was purchased from Kanto Chemical Co., Inc. These agents were used without further purification. The liquid state

^{1}H NMR spectrum of 1.0 M TBAF in THF showed the presence of 5.7 wt% water, which is consistent with the analysis conducted by Sigma Aldrich.

4.2.2 Preparation of Na-Oct, C_{16}TMA-Oct, and mesoporous silica SBA-15

Layered Na-octosilicate was synthesized according to a previously reported method with some modification.[27] SiO_2, NaOH, and deionized water were mixed at a ratio of 4 : 1 : 25.8. The mixture was hydrothermally treated in an autoclave at 100 °C for 4 weeks. The product was washed with deionized water three times, vacuum filtered with a filter paper (ADVANTEC 5C), and dried at 45 °C to obtain Na-Oct. C_{16}TMA-Oct was also obtained following the procedure reported previously.[10,27] Na-Oct (1.5 g) was dispersed in an aqueous solution of C_{16}TMACl (0.1 M, 100 mL); the mixture was stirred at room temperature for 24 h, and the supernatant was removed by centrifugation. This ion exchange step was repeated twice. Finally, the product was washed with deionized water twice and dried under reduced pressure at room temperature to obtain C_{16}TMA-Oct.

Mesoporous silica SBA-15 was prepared according to a previously reported method.[28,29] To investigate the effect of inorganic support on silylation, a silylation reaction was performed on mesoporous silica SBA-15 instead of layered octosilicate. Hydrochloric acid (0.6 M, 40 g), water (110 g), and surfactant (P123, 4 g) were mixed in an eggplant flask and the mixture was stirred until the P123 was dissolved. TEOS (8.5 g) was added to the mixture, and the resulting mixture was stirred at 45 °C for 8 h first and then at 80 °C for 15 min. The product was separated by filtration, washed with water, dried at room temperature, and then treated thermally at a rate of 1 °C/min and calcined at 550 °C for 6 h to obtain SBA-15.

4.2.3 Silylation of C_{16}TMA-Oct

The reaction of C_{16}TMA-Oct with C_8TES as a silylating agent is described below as a typical example. C_{16}TMA-Oct (0.2 g) was dried in a Schlenk flask under reduced pressure at 120 °C for 2 h. Then, the sample was heated at 100 °C and the atmosphere was changed from air to dry N_2. After this treatment, DMF (4 mL), C_8TES (1.15 mL), and a THF solution of TBAF (variable amounts) were added to C_{16}TMA-Oct and the mixture was stirred for 4 d. The amount of C_8TES was ten times greater than necessary for the quantitative capping of the reaction sites ($SiOH/SiO^-$) of C_{16}TMA-Oct supposing dipodal silylation with diethoxy groups. The amount of added TBAF in THF was varied from 0.1 mL of 0.1 M solution and 1 mL of 0.1 M solution to 0.2 mL of 1 M solution; these correspond to 0.027, 0.27, or 0.54, equivalent to the one reaction site of the layer surfaces of the octosilicate. After cooling to room temperature, the reaction product was centrifuged, washed with DMF and acetone, and further dried under reduced pressure. To investigate the effect of fluoride ions on the silylation reaction, a sample was prepared without adding a TBAF solution. The sample were names as follows: C_8-Oct (no TBAF added) and C_8-Oct_xF (x = 0.027, 0.27, or 0.54).

The effect of other silylating agents on the degree of silylation was also investigated. C_3TES (0.85 mL), C_{18}TES (1.76 mL), or MPTES (0.88 mL) was reacted with C_{16}TMA-Oct with a constant amount of TBAF (x = 0.27); these samples are denoted as C_3-Oct_0.27F, C_{18}-Oct_0.27F, and MP-Oct_0.27F, respectively. Samples without TBAF were also prepared (sample names: C_3-Oct, C_{18}-Oct, and MP-Oct). Because C_{18}TES is not soluble in DMF, silylation was performed in toluene at 80 °C.

4.2.4 Silylation of SBA-15

SBA-15 (0.1 g) was dried under reduced pressure at 120 °C for 2 h. Then, the sample was heated at 100 °C, and the atmosphere was changed from air to dry N_2. After this treatment, DMF (4 mL) and a silylating agent (C_3TES (0.85 mL), C_8TES (1.15 mL), or MPTES (0.88 mL)) were added to SBA-15, and the mixture was stirred for 4 d. After cooling to room temperature, the reaction product was centrifuged, washed with DMF and acetone, and further dried under reduced pressure. The samples silylated with C_3TES, C_8TES, and MPTES were denoted as C_3-SBA, C_8-SBA, and MP-SBA, respectively. Samples with a TBAF solution (0.1 M, 1 mL) and C_8TES or MPTES were also prepared and were denoted as C_8-SBA_F and MP-SBA_F, respectively.

4.2.4 Characterization

Powder X-ray diffraction (XRD) patterns were obtained by a parallel method using a Rigaku Ultima-III powder diffractometer (Cu Kα, λ = 0.15418 nm, 40 kV, 40 mA) and a Rigaku Ultima IV diffractometer (Fe Kα, λ = 0.19373 nm, 40 kV, 30 mA). Solid-state ^{29}Si MAS NMR spectra were recorded on a JEOL ECX-400 spectrometer at a resonance frequency of 78.6 MHz, a recycle delay of 500 s, and a 90° pulse. Samples were packed in 4 mm zirconia sample tubes and spun at 6 kHz. Solid-state ^{13}C CP/MAS NMR spectra were recorded on a JEOL ECX-400 spectrometer at a resonance frequency of 99.55 MHz, recycle delay of 10 s, and contact time of 5 ms. Samples were packed in a 4 mm silicon nitride sample tube and spun at 6 kHz. Each chemical shift was corrected using −33.8 ppm of polydimethylsilane (PDMS) and 17.4 ppm (CH_3) of hexamethylbenzene (HMB) as external standards. Liquid-state ^{1}H and ^{29}Si NMR spectra were measured using a JEOL ECZ-500 spectrometer at a resonance frequency of 500.16

MHz (^{1}H) and 99.36 MHz (^{29}Si), a 45° pulse (Si), and a recycle delay of 5 s (^{1}H) and 10 s (^{29}Si). In a 5 mm glass sample tube, $CDCl_3$ was used as a deuterated solvent, and tetramethylsilane (TMS) was used as an internal standard with a chemical shift of 0 ppm. Fourier transform infrared (FT-IR) spectra were measured in KBr pellets using a FT/IR-6100 (JASCO) spectrometer. Microscopic Raman spectra were measured using an in-Via Reflex (Renishaw) spectrometer at an excitation wavelength of 532 nm. The contents of carbon, hydrogen, and nitrogen were measured using a CHN analysis instrument (PerkinElmer, 2400 Series II). The C, H, and N contents of some samples were analyzed using a Yanaco CHN corder Type MT-5. The temperatures of heating and oxidation (conc. 15% O_2) and the reduction furnaces were 950, 850, and 550 °C, respectively. The sulfur contents were analyzed by ion chromatography using an Organic Halogen/Sulfur Analysis System with a Yanaco SQ-10 instrument. Both chemical analyses were conducted by A-Rabbit-Science Japan Co. Ltd. The amounts of silicon and sodium were determined by inductively coupled plasma optical emission spectrometry (ICP-OES) (Agilent Technologies, Agilent 5100). A sample was prepared by a melting method using $Li_2B_4O_7$ as a flux. XPS spectra were measured with a PHI 5000 VersaProbe II (ULVAC-PHI, Inc.) spectrometer using AlKα. TEM images were obtained using a JEM-2010 (JEOL) microscope at an accelerating voltage of 200 kV, and HR-SEM images were obtained using an S-5500 microscope (Hitachi High-Technologies Co.) at an accelerating voltage of 1 kV.

4.3 Results and Discussion

4.3.1 Effect of the presence of TBAF on the silylation of layered octosilicate with C_8TES

C_8TES presenting a medium-length alkyl chain was used as a model compound to investigate the effect of the addition of TBAF on the degree of silylation. Figs. 4.1 (a)–(c) shows the powder X-Ray diffraction (XRD) patterns of C_{16}TMA-Oct, C_8-Oct, and C_8-Oct_0.27F. The diffraction peak at $2\theta = 49°$, attributable to the (400) plane of the layered silicate structure, was observed for all the samples, indicating the retention of the crystal structure of octosilicate. The profile of C_8-Oct obtained in the absence of TBAF (Fig. 4.1 (b)) shows that the basal spacing (d = 2.47 nm) decreased from that of the starting compound, C_{16}TMA-Oct (d = 2.79 nm, Fig. 4.1 (a)). When C_{16}TMA-Oct was modified with C_8TES in the presence of TBAF, the basal spacing was further reduced to d = 2.23 nm, as shown in Fig. 4.1 (c). This decrease in basal spacing is consistent with the decrease in the amount of remaining C_{16}TMA in the sample obtained in the presence of TBAF, as determined from the elemental analysis and ^{13}C CP/MAS NMR data reported below.

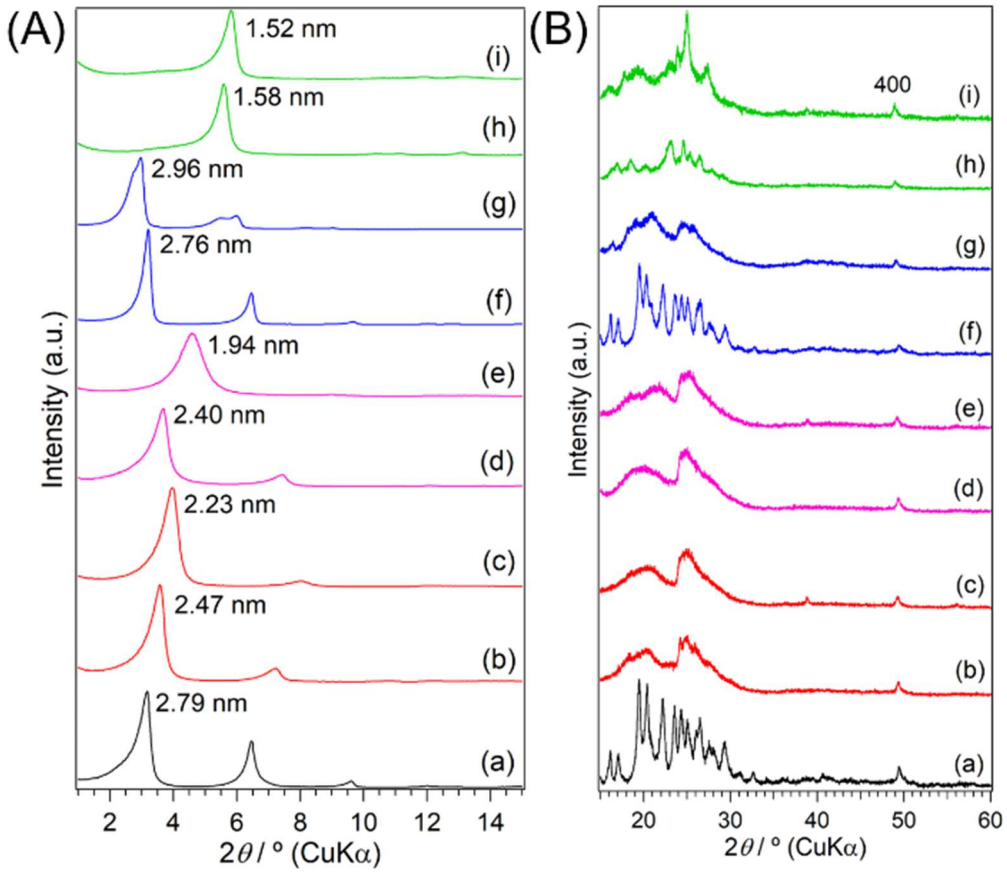

Fig. 4.1 Powder XRD patterns of (a) C_{16}TMA-Oct, (b) C_8-Oct, (c) C_8-Oct_0.27F, (d) C_3-Oct, (e) C_3-Oct_0.27F, (f) C_{18}-Oct, (g) C_{18}-Oct_0.27F, (h) MP-Oct, and (i) MP-Oct_0.27F. **(A)** Profiles in the low angle region and **(B)** profiles with magnified intensities in the high angle region.

Figs. 4.2 (a)–(c) shows the ^{29}Si MAS NMR spectra of C_{16}TMA-Oct, C_8-Oct, and C_8-Oct_0.27F. The ^{29}Si MAS NMR spectrum of C_{16}TMA-Oct (Fig. 4.2(a)) shows the signals attributable to Q^3 (**Si**$(OSi)_3OH/O^-$) and Q^4 (**Si**$(OSi)_4$) units at −100 ppm and −111 ppm, respectively, with an integral intensity ratio of 1 : 1. These chemical shifts and peak intensities are consistent with those reported in previous studies.[7,9,10,17] The spectrum of C_8-Oct (Fig. 4.2 (b)) shows the signals arising from T^2 (C_8H_{17}**Si**$(OSi)_2OH/OEt$), Q^3, and Q^4 units at the integral intensity ratio of 0.18 : 0.67 : 1.33 (Table 4.2). Because the Q^3 unit is converted to Q^4 by the silylation reaction and a T^2 environment appears, the degree of

silylation of C_8-Oct (the ratio of the modified silylating agent to all the reaction sites on the octosilicate surfaces; one pair of $SiOH/SiO^-$ corresponding to one reaction site) was calculated to be 33% ($(1 - Q^3) \times 100$). The spectrum of C_8-Oct_0.27F (Fig. 4.2 (c)) displays the signals arising from the T^2, Q^3, and Q^4 units at an integration ratio of 0.26 : 0.40 : 1.60. The degree of silylation, calculated in the same manner, was 60%. The broadening of the signal due to Q^4 (Fig. 4.2 (c)) is consistent with the increased formation of new Q^4 silicons by enhanced silylation. In addition, the ratios of the T^2 units to the decreases in the Q^3 units ($T^2/(1 - Q^3)$) were approximately 1 : 2 for both of samples after silylation, suggesting dipodal silylation of the octosilicate surfaces.

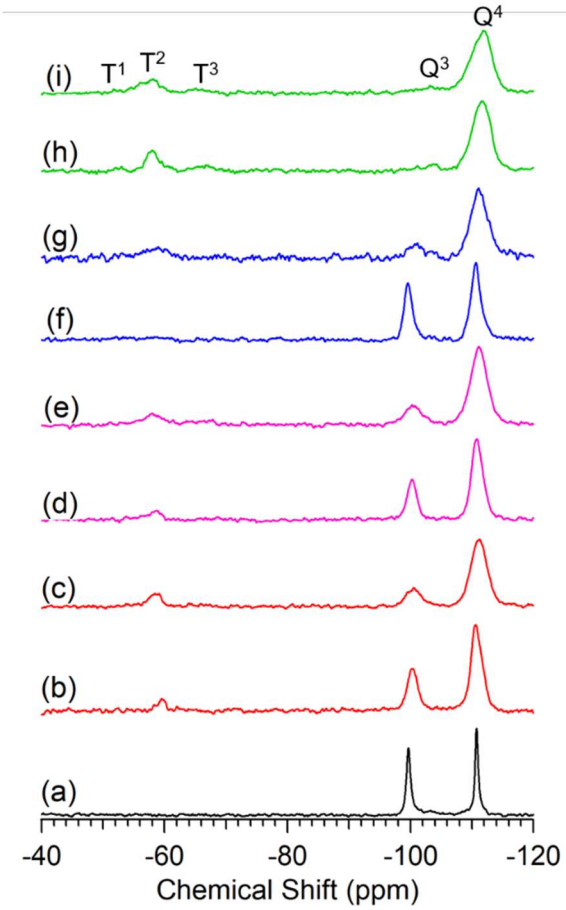

Fig. 4.2 ^{29}Si MAS NMR spectra of (a) C_{16}TMA-Oct, (b) C_8-Oct, and (c) C_8-Oct_0.27F, (d) C_3-Oct, (e) C_3-Oct_0.27F, (f) C_{18}-Oct, (g) C_{18}-Oct_0.27F, (h) MP-Oct, and (i) MP-Oct_0.27F.

Table 4.2 Integrated intensity ratios of ^{29}Si MAS NMR spectra of silylated samples.

Sample name	Integral intensity ratio				Degree of silylation / %
	T^2	T^3	Q^3	Q^4	
C_8-Oct	0.18	-	0.67	1.33	33
C_8-Oct_0.27F	0.26	-	0.40	1.60	60
C_3-Oct	0.18	-	0.59	1.41	41
C_3-Oct_0.27F	0.25	0.10	0.41	1.59	59
C_{18}-Oct	0.12	-	0.77	1.23	23
C_{18}-Oct_0.27F	0.34	0.10	0.32	1.68	68
MP-Oct	0.48[a]		0.11	1.89	89
MP-Oct_0.27F	0.51[a]		0.20	1.80	80

[a] Integrated intensity ratio of T^1 toT^3

Figs. 4.3(A)(a)–(c) shows the ^{13}C CP/MAS NMR spectra of C_{16}TMA-Oct, C_8-Oct, and C_8-Oct_0.27F; more details (enlarged profiles and peak assignments) are provided in Fig. 4.3(B). When C_{16}TMA-Oct was modified with C_8TES with and without the addition of TBAF, a broad signal at 12.8 ppm attributable to Si–**C**H_2 (C'1), signals at 33.0 ppm, 30.4 ppm, and 23.6 ppm attributable to methylene groups ((C'3, C'6), (C'4, C'5), and (C'2, C'7), respectively) of octylsilyl group, and signals at 19.0 ppm and 59.7 ppm attributable to the methyl and methylene groups of ethoxysilyl group appeared in the spectra of both C_8-Oct and C_8-Oct_0.27F. In particular, the signals of the octylsilyl and ethoxysilyl groups are more intense in the spectrum of C_8-Oct_0.27F, indicating the idea

that the addition of TBAF improves the silylation yield. The enlarged profiles of C_{16}TMA-Oct, C_8-Oct, and C_8-Oct_0.27F (Figs. 4.3(B)(a)–(c)) show that the signal at 33.5 ppm, attributable to the methylene group (C5 to C13) of the all-*trans* alkyl chain (Fig. 4.3(B)(a)), shifts to 30.7 ppm (Figs. 4.3(B)(b) and (c)), indicating the disordering in the all-*trans* methylene chain of the remaining C_{16}TMA.[30]

The FT-IR spectrum of C_{16}TMA-Oct (Fig. 4.3(C)(a)) indicates the presence of a band at 3030 cm^{-1}, attributable to the C–H stretching vibration of the NCH_3 group, the bands at 2919 cm^{-1} and 2850 cm^{-1}, attributable to the asymmetric and symmetric C–H stretching of CH_2, and the peaks at 2950 cm^{-1} and 2870 cm^{-1}, attributable to the asymmetric and symmetric C–H stretching of the terminal CH_3 group of the alkyl chain, respectively.[31] The FT-IR spectra of both C_8-Oct and C_8-Oct_0.27F (Figs. 4.3(C)(b) and (c)) indicate that the intensities of these bands were weakened, which is consistent with the ^{13}C CP/MAS NMR results. In addition, the intensity of the band at 960 cm^{-1} due to the Si–OH stretching vibration of the silanol group[16,32] decreased, which also indicates the introduction of the octylethoxysilyl group, as schematically shown in the diagram of the dipodal grafting in Scheme 4.1; however, the difference in the degree of decrease between C_8-Oct and C_8-Oct_0.27F is not so clear from the FT-IR data.

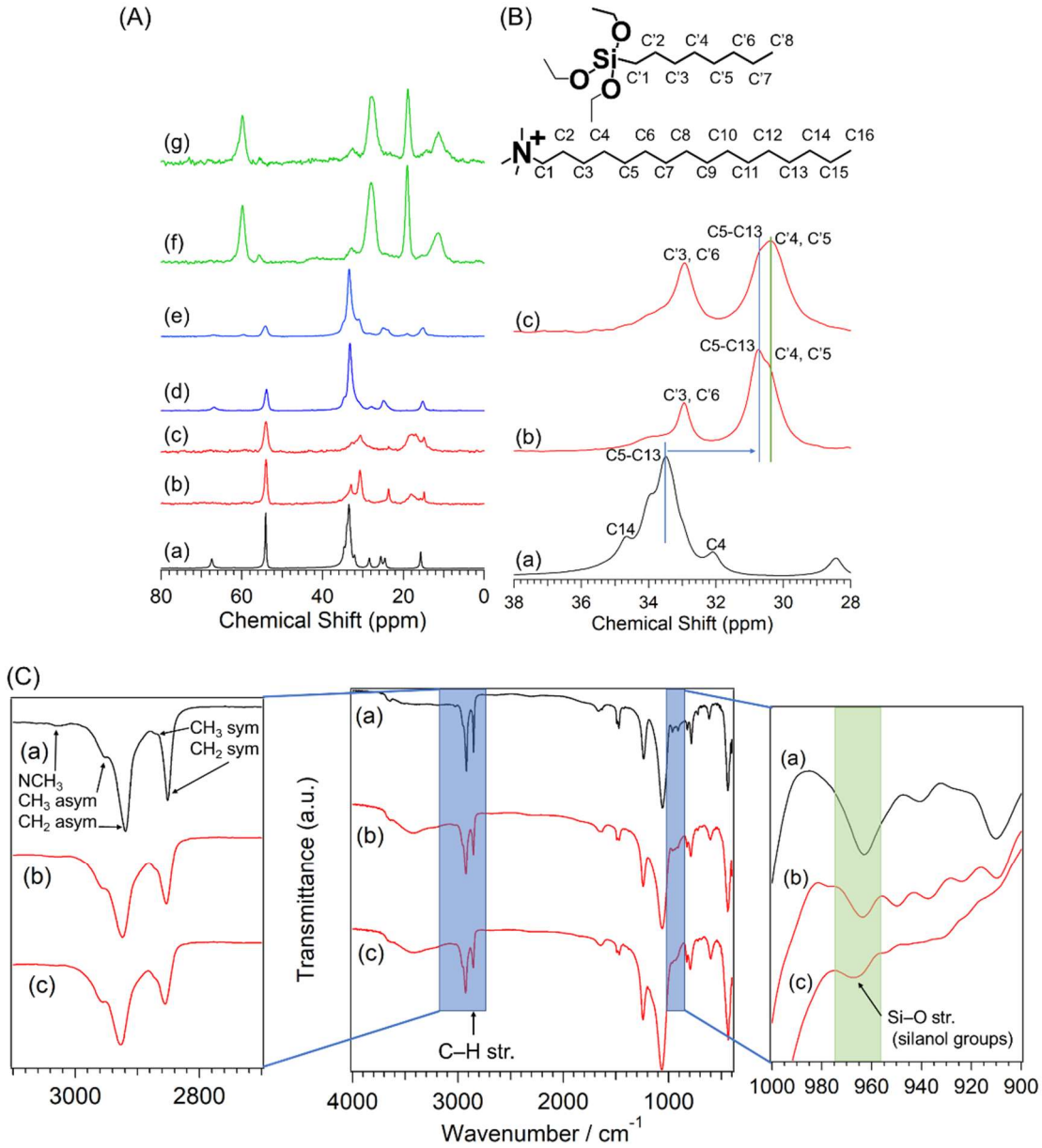

Fig. 4.3 (A) ^{13}C CP/MAS NMR spectra of (a) C_{16}TMA-Oct, (b) C_8-Oct, (c) C_8-Oct_0.27F, (d) C_3-Oct, (e) C_3-Oct_0.27F, (f) C_{18}-Oct, (g) C_{18}-Oct_0.27F, (h) MP-Oct, and (i) MP-Oct_0.27F. (B) The magnified profiles of ^{13}C CP/MAS NMR spectra of (a) C_{16}TMA-Oct, (b) C_8-Oct, (c) C_8-Oct_0.27F. (C) FT-IR spectra of (a) C_{16}TMA-Oct, (b) C_8-Oct, (c) C_8-Oct_0.27F

The elemental analysis of the samples (Table 4.3) also support the above results. The amount of nitrogen was reduced from 2.4 wt% of C_{16}TMA-Oct to 1.5 wt% and 1.0 wt% for C_8-Oct and C_8-Oct_0.27F, respectively, due to the grafting of C_8TES. Because the observed contents of nitrogen were relatively low (1.0 wt% and 1.5 wt%), the calculated values presented here should be treated as semi-quantitative estimates. By multiplying each Si content (18.7 wt%, 21.9 wt%, and 24.6 wt%) by the ^{29}Si MAS NMR intensity ratio $(Q^3 + Q^4)/(T^2 + Q^3 + Q^4)$ (1.00, 0.92, and 0.88, respectively), the octosilicate-derived content Si(Si(Q)) was calculated to be 18.7 wt%, 20.0 wt%, and 21.8 wt% for C_{16}TMA-Oct, C_8-Oct, and C_8-Oct_0.27F, respectively. Accordingly, the N/Si(Q) ratios for C_{16}TMA-Oct, C_8-Oct, and C_8-Oct_0.27F were 0.26, 0.15, and 0.09, respectively, suggesting that the C_{16}TMA cations were desorbed. The amounts of carbon arising from C_8TES in C_8-Oct and C_8-Oct_0.27F were 5.5 wt% and 12.5 wt%, respectively. These values were obtained by subtracting the amount of C arising from C_{16}TMA cation, which was calculated from the amount of nitrogen, from the total amount of carbon. The ratio of C_8TES-derived C to Si(Q) content (C(C_8TES)/Si(Q)) was calculated to be 0.64 and 1.34, indicating that the degree of silylation of layered octosilicate with C_8TES is significantly improved by the catalytic amounts of TBAF.

Table 4.3 Carbon, nitrogen, and silicon contents of silylated samples.

Sample name	C / wt%	N / wt%	Si / wt%
C_{16}TMA-Oct	36.8	2.4	18.7
C_8-Oct	30.4	1.5	21.9
C_8-Oct_0.027F	28.9	1.1	25.0
C_8-Oct_0.27F	28.6	1.0	24.6
C_8-Oct_0.54F	31.1	0.8	23.8

The ^{29}Si MAS NMR spectra of C_8-Oct_0.27F reacted for different reaction times (1, 2, and 4 d) were shown in Fig. 4.4 (b), (c), and (d), respectively. These spectra exhibited the signals assigned to the T^2, Q^3, and Q^4 units. The integral intensity ratios are 0.23 : 0.46 : 1.54, 0.19 : 0.41 : 1.59, and 0.26 : 0.40 : 1.60 for (b), (c), and (d), respectively. The degree of silylation increased with the reaction time and almost reached a plateau after 2 d (1 d ; 54 %, 2 d ; 59 %, and 4 d ; 60 %). The incomplete silylation is probably due to the steric hindrance of long alkyl chains and alkoxy groups. In the absence of TBAF, the degree of silylation was much lower (33%) even after 4 d (Table 4.2); therefore, much longer time will be required to achieve the maximum degree of silylation.

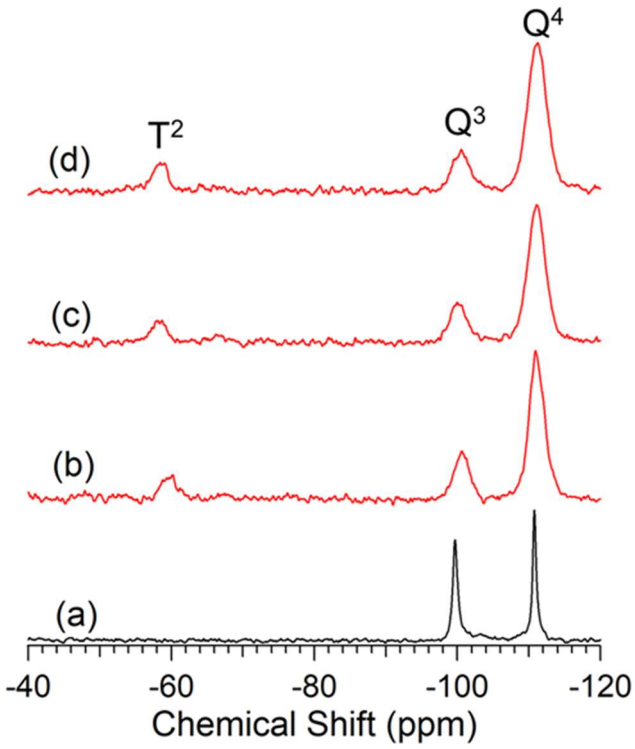

Fig. 4.4 ^{29}Si MAS NMR spectra of (a) C_{16}TMA-Oct and (b–d) C8-Oct_0.27F silylated for (b) 1 d, (c) 2 d, and (d) 4 d.

4.3.2 Effect of the amount of TBAF on the silylation with C_8TES and plausible silylation reaction mechanism

The powder XRD patterns of C_8-Oct and C_8-Oct_xF (x = 0.027, 0.27, or 0.54) are shown in Fig. 4.5. The diffraction peak at $2\theta = 49°$ was observed for all the samples, suggesting the retention of the crystallinity in the in-plane direction. The d values of the basal spacing gradually decreased (d = 2.47 nm → 2.39 nm → 2.26 nm → 2.23 nm) with the increase in the amount of TBAF added. The CHN analysis and solid-state ^{13}C NMR data of the samples, as described later, show that the amount of C_{16}TMA continuously decreased with the increasing amount of TBAF. Consequently, the decrease in the basal spacing indicates the progress of the desorption of C_{16}TMA cations, which is consistent with the above-mentioned results.

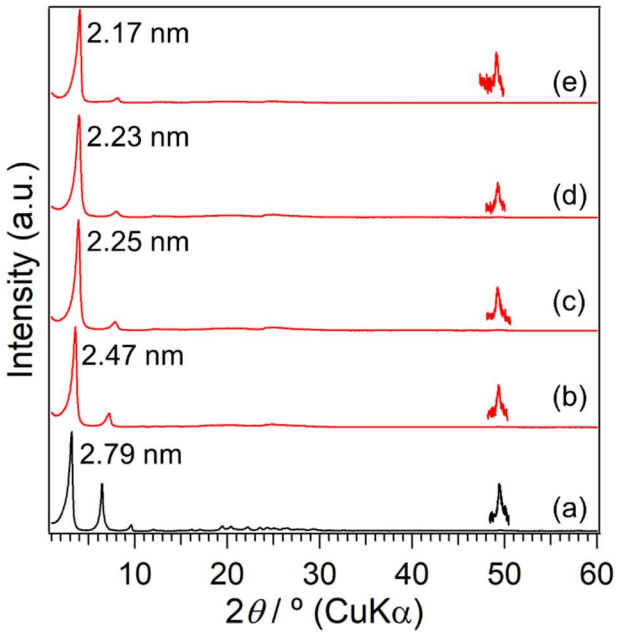

Fig. 4.5 Powder XRD patterns of (a) C_{16}TMA-Oct, (b) C_8-Oct, (c) C_8-Oct_0.027F, (d) C_8-Oct_0.27F, and (e) C_8-Oct_0.54F.

The ^{29}Si MAS NMR spectra of C_8-Oct and C_8-Oct_*x*F are shown in Fig. 4.6. The Q^3 and Q^4 signals were observed at −100 ppm and −111 ppm, respectively, for both C_8-Oct_0.027F and C_8-Oct_0.54F, which are consistent with those of C_8-Oct_0.27F mentioned in the section above. The degrees of silylation calculated from the integral intensity ratios of the signals were 54%, 60%, and 71% for C_8-Oct_0.027F, C_8-Oct_0.27F, and C_8-Oct_0.54F, respectively (Table 4.4). This indicates that the silylation reactivity of layered octosilicate with C_8TES is enhanced with increasing amounts of TBAF. Only the T^2 peak appeared as a signal arising from C_8TES in the spectrum of C_8-Oct_0.027F. The ratio of the T^2 signal intensity over the reduced intensity in the Q^3 signals before and after the silylation was 1 : 2, which supports the observation that the dipodal silylation proceeds in a manner similar to that of C_8-Oct_0.27F. In addition, the amount of the added catalyst corresponds to 2.7% of the reaction sites of layered octosilicate, but the degree of

silylation proceeds by 21%, which suggests that F^- acts as a catalyst. On the other hand, both T^2 and T^3 ($R\mathbf{Si}(OSi)_3$) signals were observed for C_8-Oct_0.54F. This is probably due to the condensation between proximal silylating agents by hydrolysis and condensation of ethoxy groups because the amount of water increased with increasing amount of added TBAF (knowing that TBAF contains 5.7 wt% water, as stated in the Materials in the Experimental Section).

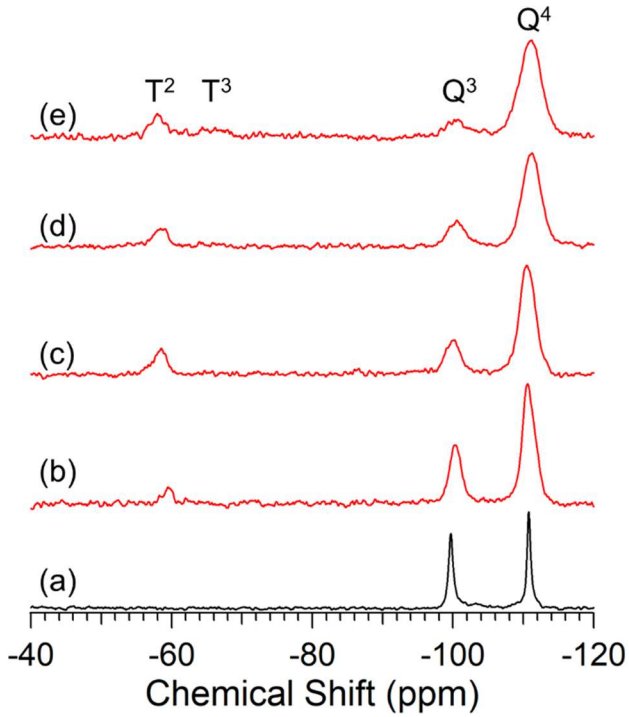

Fig. 4.6 ^{29}Si MAS NMR spectra of (a) C_{16}TMA-Oct, (b) C_8-Oct, (c) C_8-Oct_0.027F, (d) C_8-Oct_0.27F, and (e) C_8-Oct_0.54F.

Table 4.4 Integrated intensity ratios of ^{29}Si MAS NMR spectra of silylated samples.

Sample name	Integral intensity ratio				Degree of silylation
	T^2	T^3	Q^3	Q^4	/ %
C_8-Oct	0.18	-	0.67	1.33	33
C_8-Oct_0.027F	0.29	-	0.46	1.54	54
C_8-Oct_0.27F	0.26	-	0.40	1.60	60
C_8-Oct_0.54F	0.27	0.13	0.29	1.71	71

Fig. 4.7 shows the ^{13}C CP/MAS NMR spectra of C_8-Oct and C_8-Oct_*x*F. The relative intensity ratio of the signal at 54.1 ppm, attributed to N–**C**H$_3$ of C_{16}TMA cations over the other signals due to the octyl group,[30] decreased with increasing amount of TBAF. The relative intensity ratio of the broad signal at 12.8 ppm, attributed to Si–**C**H$_2$, the signals at 19.0 ppm and 59.7 ppm, attributed to the methyl and methylene groups of the ethoxysilyl group, and the signal at 23.6 ppm, attributed to the methylene group (C'2, C'7) of octylsilyl group, also increased with increasing amounts of TBAF by comparison with the intensity of the signals due to C_{16}TMA cations.

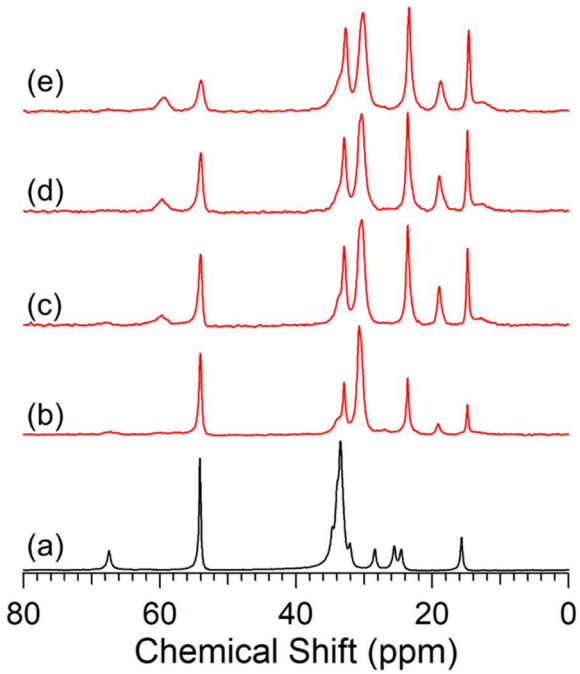

Fig. 4.7 ^{13}C CP/MAS NMR spectra of (a) C_{16}TMA-Oct, (b) C_8-Oct, (c) C_8-Oct_0.027F, (d) C_8-Oct_0.27F, and (e) C_8-Oct_0.54F.

The contents of nitrogen gradually decreased (1.5 wt% → 1.1 wt% → 1.0 wt% → 0.8 wt%) with increasing amounts of TBAF added, while the carbon content arising from C_8TES, calculated by subtracting the amount of carbon arising from $C_{16}TMA^+$, gradually increased (5.4 wt% → 11.8 wt% → 12.5 wt% → 17.4 wt%). The value of N/Si(Q) decreased from 0.15 to 0.10, 0.09, and finally 0.09, and the ratio of C(C_8TES)/Si(Q) increased from 0.63 to 1.26, 1.34, and finally 2.06. These results also show that increasing amounts of TBAF results in increasing amounts of eliminated C_{16}TMA cations and introduced octylethoxysilyl groups.

The mechanism of the silylation without the addition of fluoride ions can be explained as follows. The reaction was conducted at 100 °C, and EtOH was generated each time alkoxysilane reacted with SiOH, accompanied by the generation of water by the reaction of EtOH with surface silanol groups.[13,33,34] Consequently, C_{16}TMA cations

may be eliminated as hydroxide.[13] The reaction mechanism of the promotion of silylation by the addition of fluoride ion (TBAF) was discussed on the basis of the sol-gel reaction of alkoxysilanes catalyzed by fluoride ions as follows (Scheme 4.2).[23–26]

A) An XPS peak due to the F 1s orbital at 687 eV, attributed to the Si–F bond,[35] was observed (Fig. 4.8), indicating the formation of unidentified Si species with an Si–F bond; this, in turn, indicates the nucleophilic attack on the silylating agent.

B) It is plausible that the oxygen atom of the Si–OH group at the surfaces of the layers undergoes nucleophilic attack on the Si atom that has become electrophilic due to the formation of Si–F bonds, resulting in the formation of a hexacoordinated state with Si–O–Si.

C) Then, a tetracoordinated state can form by the elimination of EtOH and F^- from the hexacoordinated silicon; this process generally occurs in sol-gel reactions catalyzed by fluoride ions. Then, the silylation is completed by processes D) to G), as in the case where there are no fluoride ions.

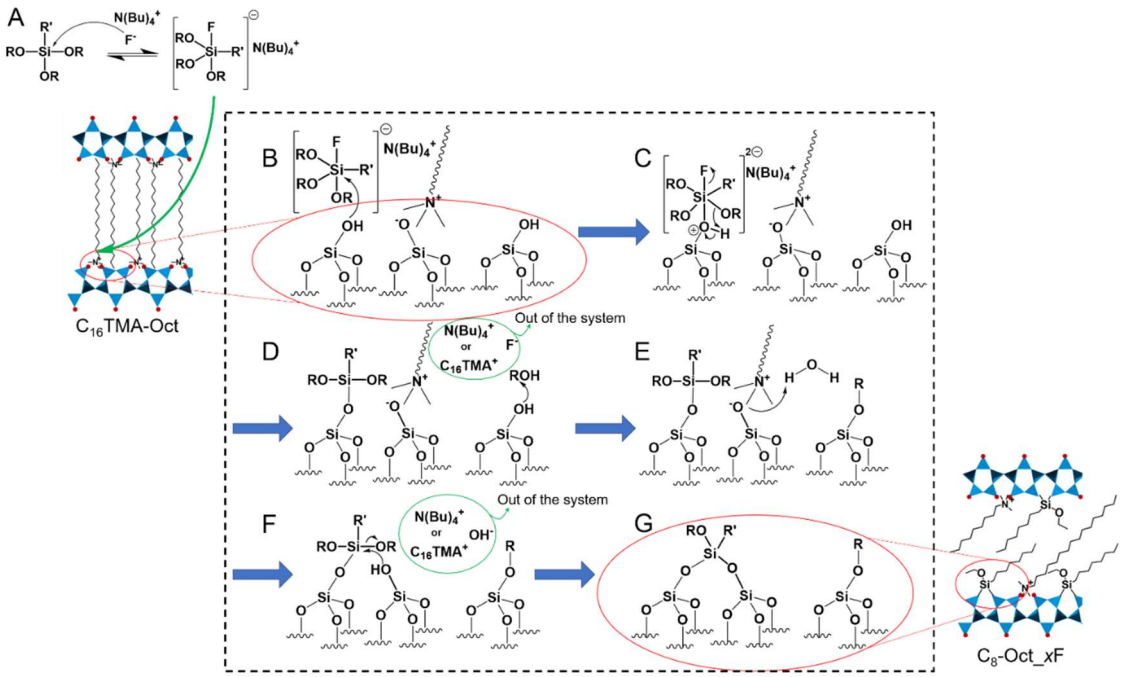

Scheme 4.2 Plausible reaction mechanism of silylation of layer surfaces of layered octosilicate by the addition of fluoride ions.

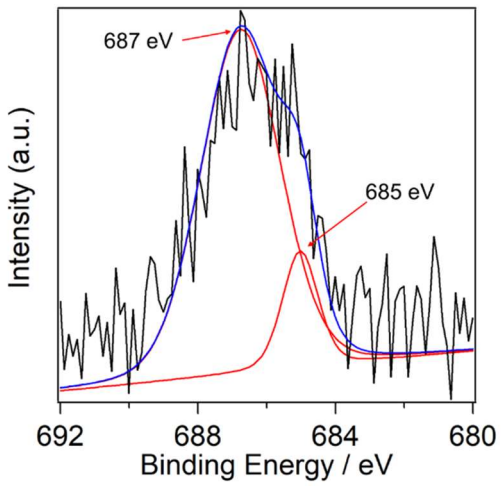

Fig. 4.8 XPS spectrum of C_8-Oct_0.27F.

4.3.3 Silylation of C_{16}TMA-Oct with silylating agents possessing different alkyl chain lengths

To investigate the effect of the alkyl chain length of silylating agents on the degree of silylation, reactions using C_3TES and C_{18}TES were conducted to compare the results with those obtained using C_8TES. Hereafter, the ratio of TBAF per the reaction site of layered octosilicate was fixed at 0.27 because T^3 units, showing unfavorable condensation between organoalkoxysilanes, appeared for the case of C_8-Oct_0.54F.

Figs. 4.1 (d)–(g) shows powder XRD patterns of C_3-Oct, C_3-Oct_0.27F, C_{18}-Oct, and C_{18}-Oct_0.27F. As described above, the diffraction peak at $2\theta = 49°$, attributed to the in-plane (400) plane of the octosilicate, was observed for all the samples. When C_3TES was used as the silylating agent, as shown in the profiles of Figs. 4.1 (d) and (e), the basal spacing decreased from d = 2.79 nm for C_{16}TMA-Oct to d = 2.40 nm (C_3-Oct) and 1.94 nm (C_3-Oct_0.27F), respectively. The gallery heights (1.66 and 1.20 nm for C_3-Oct and C_3-Oct_0.27F, respectively), which were calculated by subtracting the layer thickness (0.74 nm)[27] from the basal spacings, do not correspond to the length of propyl group (0.37 nm) grafted on the layers, which suggests partial removal of C_{16}TMA cations, as supported by the decrease in the amount of nitrogen (described below). When C_{18}TES was modified (Figs. 4.1 (f) and (g)), the basal spacings were d = 2.76 nm and 2.96 nm for C_{18}-Oct and C_{18}-Oct_0.27F, respectively. The larger d value of the basal spacing of C_{18}-Oct_0.27F compared to that of C_{16}TMA-Oct suggests the introduction of C_{18}TES owing to the longer alkyl chain of C_{18}TES compared to that of the C_{16}TMA cation. On the other hand, the basal spacing of C_{18}-Oct remained similar to that of C_{16}TMA-Oct, suggesting that the amount of grafted silylating agent between layers was small, as supported by the ^{29}Si MAS NMR data described below.

Interestingly, there is a linear relationship between the number of carbon atoms in the alkyl chain and the *d* value of the basal spacing (Fig. 4.9). The increase in the basal spacing per CH_2 of the silylating agent was 0.0247 and 0.0687 nm for the three samples prepared without and with TBAF, respectively. Note that the R^2 values, i.e., the degree of data dispersion, are close to 1. In general, the increase per CH_2 in the length of the all-*trans* alkyl chain is calculated to be 0.125 nm (0.154 nm (C–C bond length) × sin(54.75°)). The increase of 0.125 nm per CH_2 unit indicates a monolayer arrangement of alkyl groups oriented perpendicular to the layer. If the increase is twice the value, the arrangement should be bilayered perpendicularly to the layers. The observed data are much smaller than the values calculated from the perpendicularly oriented alkyl chain lengths of silylating agents. Accordingly, the relatively small inclination of the relationships between the basal spacings and the carbon chain lengths (Fig. 4.9) for all the samples should be influenced by tilted alkyl groups on silyl groups to the layer and the co-presence of remaining C_{16}TMA cations between the layers. The inclination of the line for the samples prepared without TBAF is smaller than that prepared with TBAF, which is in accordance with the lower amounts of eliminated C_{16}TMA ions in the samples prepared without TBAF, as described below.

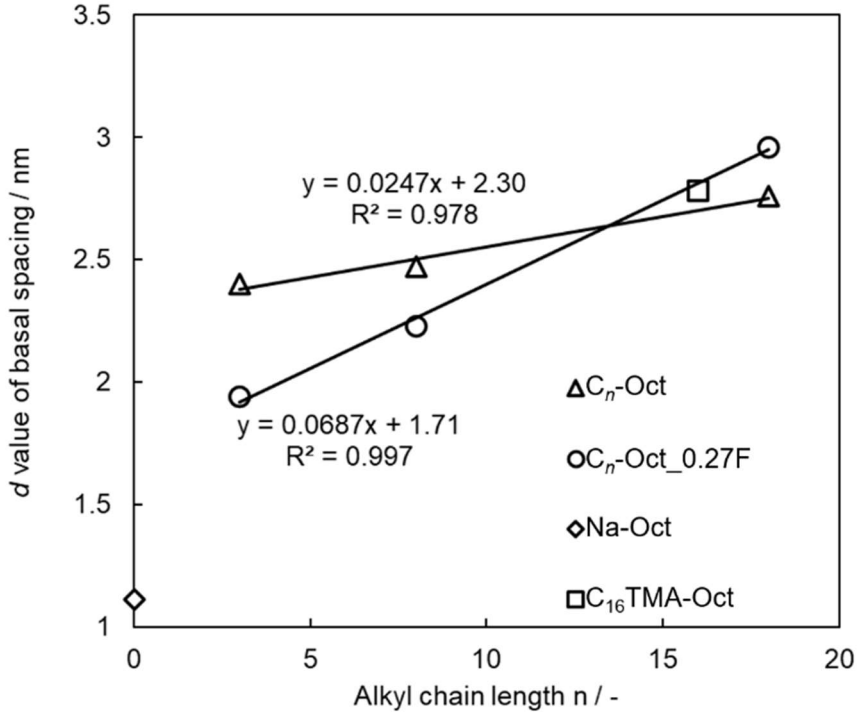

Fig. 4.9 Relationships between the number of carbon atoms in alkyl chain and *d* values of basal spacing of C_n-Oct and C_n-Oct_0.27F.

Figs. 4.2 (d)–(g) shows the ^{29}Si MAS NMR spectra of C_3-Oct, C_3-Oct_0.27F, C_{18}-Oct, and C_{18}-Oct_0.27F. The signals attributed to the T^2, Q^3, and Q^4 sites were observed for the spectrum of C_3-Oct. On the other hand, in the spectrum of C_3-Oct_0.27F (Fig. 4.2 (e)), T^2, T^3, Q^3, and Q^4 sites were observed. The integral intensity ratio (T^2 (: T^3): Q^3: Q^4) was 0.18:0.59:1.41 and 0.25:0.10:0.41:1.59 for C_3-Oct and C_3-Oct_0.27F, respectively. In the spectra of C_{18}-Oct and C_{18}-Oct_0.27F (Figs. 4.2 (f) and (g)), the signals belonging to the T^2, Q^3, and Q^4 sites were observed for the sample without the addition of TBAF, and the T^2, T^3, Q^3, and Q^4 were observed for the sample with the addition of TBAF. The integral intensity ratios (T^2 (: T^3): Q^3: Q^4) of these signals were 0.12:0.77:1.23 and 0.34:0.10:0.32:1.68 for C_{18}-Oct and C_{18}-Oct_0.27F, respectively. The degree of silylation using C_3TES was calculated to be 41% and 59% for the samples

prepared with and without TBAF, respectively. Similarly, the degree of silylation of C_{18}TES was 23% and 68%, respectively. The degree of silylation of C_{18}-Oct without the addition of TBAF was lower than those of C_8-Oct and C_3-Oct. The solvent for the reaction using C_{18}TES was changed from DMF to toluene because C_{18}TES does not dissolve in DMF. Because C_{16}TMA-Oct does not swell as much in toluene, it is likely that C_{18}TES, which is longer than C_{16}TMA, has lower accessibility to the interlayer spaces, which reduces the degree of silylation. However, our preliminary study on the use of toluene for the C_8TES case showed that the difference in the silylation reactivities was not large.

The degree of silylation was higher for the silylating agents with shorter alkyl chains (C_3-Oct: 41%, C_8-Oct: 33%, C_{18}-Oct: 23%) when TBAF was not added (Fig. 4.2). This can be explained by the accessibility of the silylating agent between the layers. It was also confirmed that the addition of TBAF improves the degree of silylation for all the cases using a silylating agent with an alkyl chain. In particular, the degree of silylation was significantly improved for the case of C_{18}-Oct_0.27F, which is in good agreement with Scheme 4.2, showing that the added TBAF contributes to the increase in the reactivity of the organotriethoxysilyl group. This should be effective in overcoming the limitation of the accessibility of the silylating agent between layers.

Figs. 4.3 (d)–(g) shows the ^{13}C CP/MAS NMR spectra of C_3-Oct, C_3-Oct_0.27F, C_{18}-Oct, and C_{18}-Oct_0.27F. A relative decrease in the signal attributed to N–CH_3 at 54.1 ppm was observed for all the samples after silylation, suggesting a partial elimination of the C_{16}TMA cations. The spectra of C_3-Oct and C_3-Oct_0.27F (Figs. 4.3 (d) and (e)) show the appearance of signals attributed to Si–**C**H_2 at 14.9 ppm, methyl group and methylene group of propyl group (Si–CH_2–**C**H_2–**C**H_3) at 16 ppm to 20 ppm. The spectra of C_{18}-Oct and C_{18}-Oct_0.27F (Figs. 4.3 (f) and (g)) show the appearance of the signal at 15.1 ppm

attributed to Si–**C**H_2. The signals assigned to the alkyl chains of C_{18}TES could not be distinguished from those of $C_{16}TMA^+$ because their overlapping of signals. These results indicate the introduction of the respective silylating agents and the partial elimination of C_{16}TMA cations. As in the case of C_8TES, the amounts of the silylating agents introduced were increased by the presence of TBAF, and the amounts of C_{16}TMA cations decreased accordingly (see Table 4.3 for details). These results support the increase in the degree of silylation with C_3TES and C_{18}TES by the addition of TBAF.

4.3.4 Effect of mercapto group of the silylating agent on the degree of silylation

C_{16}TMA-Oct was silylated with MPTES possessing a mercapto (thiol) group that can be developed for further applications. Compared to the case when using alkyltriethoxysilanes, the degree of silylation was very high when using MPTES with or without TBAF (Fig. 4.2). Below, the factors that play an important role in the silylation of C_{16}TMA-Oct is discussed.

Figs. 4.1 (h) and (i) shows the powder XRD patterns of MP-Oct and MP-Oct_0.27F. The basal spacings were d = 1.52 nm (MP-Oct) and 1.58 nm (MP-Oct_0.27F). The relatively large amount of introduced silyl groups and the small amount of residual C_{16}TMA ions, as described below, can explain the relatively small basal spacings of the products using MPTES, when compared with the cases using C_3TES. A lamellar structure with mercaptopropyl groups bonded onto the siloxane layer can be fabricated by hydrolysis and condensation of α, ω-bis(trimethoxysilyl)propyldisulfide and the subsequent reduction of the disulfide bond.[36] However, the d value in the stacking direction of the lamellar phase was about 1.2 nm and the value is different from those of MP-Oct and MP-Oct_0.27F because the two samples have thicker octosilicate layers.

Figs. 4.2 (h) and (i) shows the ^{29}Si MAS NMR spectra of MP-Oct and MP-Oct_0.27F. The signals attributed to the T^1 to T^3, Q^3, and Q^4 environments were observed. The integral intensity ratios of $T : Q^3 : Q^4$ were 0.48:0.11:1.89 and 0.51:0.20:1.80 for MP-Oct and MP-Oct_0.27F, respectively. The degree of silylation of MP-Oct and MP-Oct_0.27F was calculated to be 89% and 80%, respectively, indicating a higher degree of silylation even in the case of MPTES without the addition of TBAF. Fig. 4.3 (h) and (i) shows the ^{13}C CP/MAS NMR spectra of MP-Oct and MP-Oct_0.27F, respectively. In these spectra, a relatively large decrease in the signal attributed to N–CH_3 at 54.1 ppm was observed, suggesting a significant elimination of C_{16}TMA cations. The signals attributable to the second and third methylene groups from Si (HS–**C**H_2–**C**H_2–CH_2–Si) at 27.7 ppm (broad), Si–**C**H_2 at 11.3 ppm, and the methylene and methyl groups of the ethoxysilyl group at 59.9 ppm and 18.9 ppm were observed. Therefore, the introduction of 3-mercaptopropylethoxysilyl groups was also confirmed. The Raman spectra of MP-Oct and MP-Oct_0.27F (Fig. 4.10) show peaks attributable to S–H stretching at 2570 cm^{-1}, confirming the presence of mercapto groups,[37,38] which supports the ^{13}C CP/MAS NMR results. A very small peak at 510 cm^{-1} was also observed, suggesting the formation of a disulfide bond.[39]

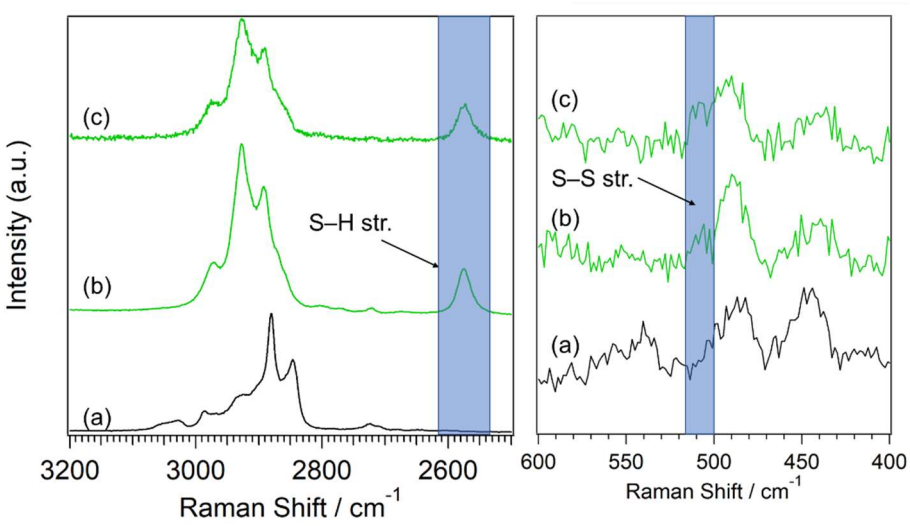

Fig. 4.10 Raman spectra of (a) C_{16}TMA-Oct, (b) MP-Oct, and (c) MP-Oct_0.27F.

The N contents of MP-Oct and MP-Oct_0.27F were 0.0 wt% and 0.2 wt%, respectively. The amounts of carbon arising from MPTES in MP-Oct and MP-Oct_0.27F were 11.1 wt% and 9.1 wt%, respectively. The calculated amounts of carbon of MP-Oct and MP-Oct_0.27F based on the respective silylation rates (89% and 80%) were 12.7 wt% and 12.0 wt%, respectively, if all ethoxy groups remained after the dipodal silylation; when all ethoxysilyl groups were hydrolyzed to silanol groups, the carbon content was calculated to be 8.5 wt% and 7.9 wt%, respectively. In all cases, the measured values (11.1 wt% and 9.1 wt%) are within the range of these calculated values. Thus, some ethoxy groups in both samples should be eliminated. The contents of S of both samples were same as 7.1 wt%. The equal amounts of S, despite the difference in the degree of silylation is probably due to the variation in the amount of ethoxy groups remaining after the silylation. The residual ratios of ethoxy groups were calculated to be approximately 60% for MP-Oct and approximately 20% for MP-Oct_0.27F from the C/S ratios (4.2 and 3.4, respectively). Therefore, in both MP-Oct and MP-Oct_0.27F, the ethoxy groups were

partially eliminated, and it was confirmed that the amounts of carbon and sulfur were within a reasonable range.

The reason why silylation of C_{16}TMA-Oct with MPTES proceeds in a higher degree than those with alkyltrialkoxysilanes (C_nTES, where C_n accounts for the number of carbon atoms in the alkyl chain (n = 3, 8, and 18)) is discussed here. Two possible differences between C_nTES and MPTES can be highlighted. (1) The first one is the fact that the electron density of Si of the silylating agents varies depending on the functional group,[40] which may affect the reactivity. However, the following paragraph shows that this does not explain the high degree of silylation with MPTES. (2) The second difference between C_nTES and MPTES lies in the polar S–H groups of MPTES, which may provide a higher accessibility to polar reaction sites (organoammonium cations on Si–OH/Si–O^- groups) between layers than for C_nTES with non-polar alkyl groups.

The reason why point (1) above cannot account for the observed difference in silylation degree between MPTES and CnTES is shown below. The solution ^{29}Si NMR spectra of C_3TES and MPTES are shown in Fig. 4.11. The signals due to the T^0 unit (R**Si**$(OEt)_3$) were observed for both spectra at the chemical shifts of −44.95 ppm for C_3TES and −45.88 ppm for MPTES.[41] The chemical shift of Si in C_3TES is located at a slightly lower magnetic field, indicating that Si in C_3TES has a lower electron density.[40] Therefore, C_3TES should be relatively more susceptible to nucleophilic attacks by silanol groups on the layer surfaces, and the degree of silylation should be higher. In practice, however, C_3TES had a lower degree of silylation. According to a report on the hydrolysis rates of alkyltriethoxysilanes by Echeverria *et al.*,[40] alkoxysilanes, in which the chemical shift of Si appears on the lower magnetic field owing to the difference in the functional groups of the alkyl moiety, have more electrophilic Si and consequently, higher hydrolysis

rate of the alkoxysilanes. Therefore, it is suggested that the reaction rate of silylation using C_3TES is higher than that using MPTES. However, the actual high and low degrees of silylation were opposite to the expected trend. This is presumably because the reaction time was sufficiently long, and the relatively higher reaction rate did not affect the degree of silylation.

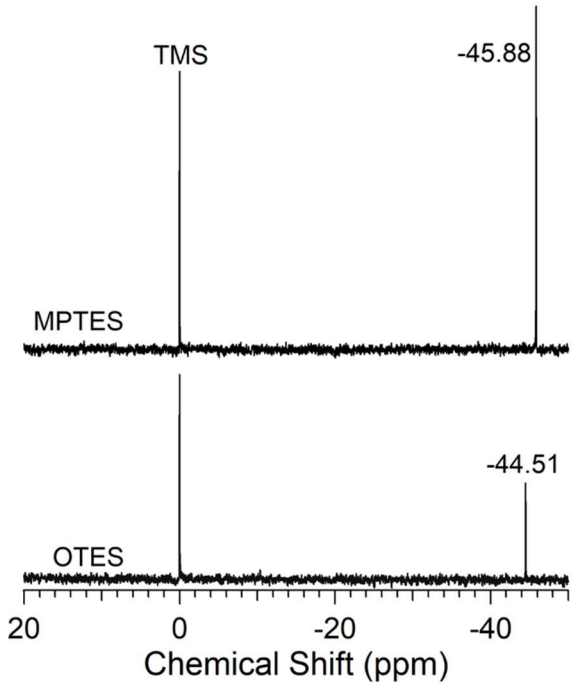

Fig. 4.11 Solution ^{29}Si NMR spectra of C_3TES and MPTES.

The reason why point (2) is a reasonable explanation is as follows. The silylation reaction of mesoporous silica SBA-15 composed of amorphous silica pore walls was performed. Since the surfactant used in the preparation of SBA-15 was removed by calcination, all the reaction sites are silanol groups. Fig. 4.12(A) shows the ^{29}Si MAS NMR spectra of SBA-15, C_3-SBA, C_8-SBA, C_8-SBA_F, MP-SBA, and MP-SBA_F (the deconvoluted spectra are shown in Fig. 4.12(B)). In the spectrum of SBA-15 (Fig. 4.12(B)(a)), the signals assigned to the Q^2 ($Si(OSi)_2(OH)_2$), Q^3, and Q^4 units were

observed at −90 ppm, −101 ppm, and −110 ppm, respectively; the integral intensity ratio of the three signals was 0.03 : 0.31 : 0.66. In the spectra of C_3-SBA and MP-SBA (Figs. 4.12(B)(b) and (e)), the signals attributed to the Q^2, Q^3, and Q^4 units were observed at the same positions. The integral intensity ratios (Q^2 : Q^3 : Q^4) were 0.02 : 0.31 : 0.67 for C_3-SBA and 0.03 : 0.27 : 0.70 for MP-SBA. The spectra of C_8-SBA, C_8-SBA_F, and MP-SBA_F (Figs. 4.12(B)(c), (d), and (f)) showed signals arising from Q^3 and Q^4 units at the integral intensity ratios of 0.30, 0.70, 0.27, 0.73, and 0.22 : 0.78, respectively. The degree of silylation of SBA-15 was calculated by a way different from that used for octosilicate. Owing to the presence of the Q^2 unit in SBA-15, the degree of silylation was estimated from the consumption of silanol groups. The ratios of the silanol groups consumed over the total contents of silanol groups were calculated to be 0.02, 0.07, 0.10, 0.04, and 0.15 for C_3-SBA, C_8-SBA, C_8-SBA_F, MP-SBA, and MP-SBA_F, respectively. These values are consistent with previously reported values observed for SBA-15 silylated with octadecyltrimethoxysilane.[42] The amounts of silanol groups consumed for the silylation was similar when using C_3-SBA, C_8-SBA, and MP-SBA, which was different from when layered octosilicate was used. This indicates that the reactivities and accessibility of C_3TES, C_8TES, and MPTES to the reaction sites on SBA-15 surfaces are similar, indicating that MPTES is more accessible than C_nTES in the ionically modified interlayer surfaces of layered octosilicate. Furthermore, the increase in the degree of silylation of SBA-15 with both C_8TES and MPTES with the addition of TBAF was also confirmed.

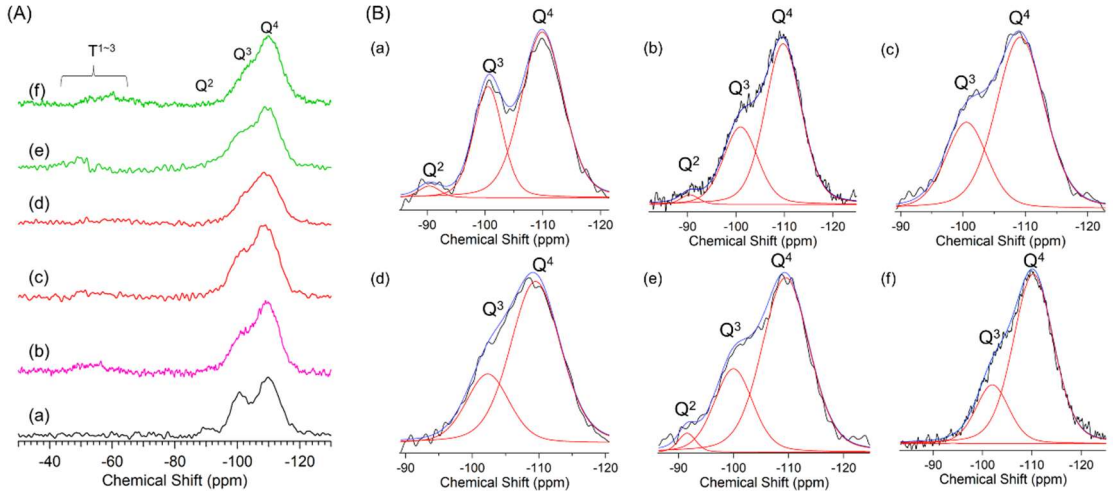

Fig. 4.12 (A) ^{29}Si MAS NMR spectra of (a) SBA-15, (b) C_3-SBA, (c) C_8-SBA, (d) C_8-SBA_F (e) MP-SBA, and (f)MP-SBA_F. (B) Their deconvoluted spectra in the range of Q environment

It is interesting to note that the morphologies of C_8-Oct_0.27F, C_3-Oct_0.27F, and C_{18}-Oct_0.27F were slightly different from that of MP-Oct_0.27F (Fig. 4.13). In particular a slight disintegration of layers was observed for the former three samples (Figs. 4.13 (a), (b), and (c)) but not in MP-Oct_0.27F (Fig. 4.13 (d)). However, further analysis is difficult at this stage.

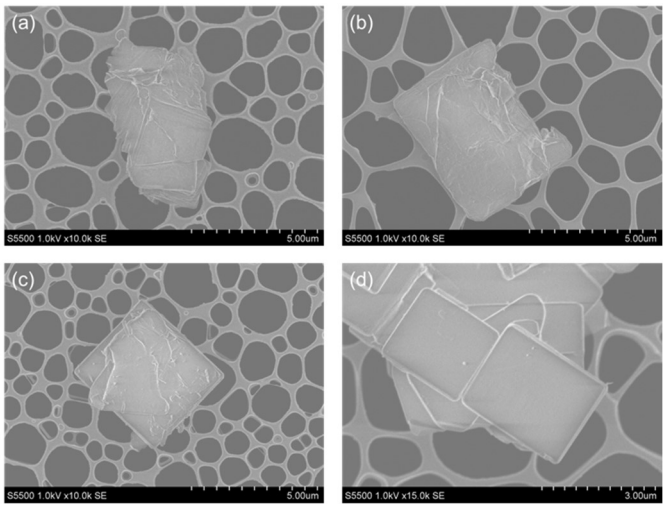

Figure 4.13 SEM images of (a) C_8-Oct_0.27F, (b) C_3-Oct_0.27F, (c) C_{18}-Oct_0.27F, and (d) MP-Oct_0.27F.

The higher degree of silylation of octosilicate with MPTES was observed even when TBAF was not added. Because there are no large differences in the reactivity of C_nTES (alkyltriethoxysilane; C_n (n = 3, 8, and 18)) and MPTES for the silylation onto SBA-15, the polarity of the mercapto group is likely to increase the accessibility to the interlayer surfaces of layered octosilicate where organoammonium cations are located.

4.4 Conclusion

The addition of TBAF was found to promote the interlayer silylation of layered octosilicate with C_8TES. The degree of silylation increased with an increase in the amount of TBAF added. When the ratio of TBAF to the reaction sites of silicate increased, the water content in the reaction system increased due to the presence of water in TBAF, which caused side reactions. The role of fluoride ions in the promotion of silylation was proposed. Although the degree of silylation using a silylating agent with different alkyl chains was improved by the addition of TBAF, MPTES improved the accessibility between layers due to its polarity, resulting in a higher degree of silylation without the addition of TBAF. The addition of TBAF in the silylation of a layered silicate effectively promoted the silylation of alkylalkoxysilanes with low interlayer accessibility. Because silica and silicates are diverse in structure and reactivity, the search for appropriate catalysts or suitable experimental conditions for the preparation of silica-organic hybrid materials by silylation will be further developed using the concept reported here.

4.5 References

1 N. Takahashi and K. Kuroda, *J. Mater. Chem.*, 2011, **21**, 14336–14353.

2 E. Ruiz-Hitzky, P. Aranda, M. Darder and M. Ogawa, *Chem. Soc. Rev.*, 2011, **40**, 801–828.

3 T. Okada, Y. Ide and M. Ogawa, *Chem. - An Asian J.*, 2012, **7**, 1980–1992.

4 F. M. Fernandes, H. Baradari and C. Sanchez, *Appl. Clay Sci.*, 2014, **100**, 2–21.

5 M. Faustini, L. Nicole, E. Ruiz-Hitzky and C. Sanchez, *Adv. Funct. Mater.*, 2018, **28**, 1–30.

6 U. Díaz and A. Corma, *Chem. - A Eur. J.*, 2018, **24**, 3944–3958.

7 N. Takahashi, H. Hata and K. Kuroda, *Chem. Mater.*, 2010, **22**, 3340–3348.

8 Y. Ide, N. Kagawa, M. Sadakane and T. Sano, *Chem. Commun.*, 2013, **49**, 9027–9029.

9 E. Doustkhah, S. Rostamnia, N. Tsunoji, J. Henzie, T. Takei, Y. Yamauchi and Y. Ide, *Chem. Commun.*, 2018, **54**, 4402–4405.

10 D. Mochizuki, A. Shimojima, T. Imagawa and K. Kuroda, *J. Am. Chem. Soc.*, 2005, **127**, 7183–7191.

11 Y. Asakura, Y. Matsuo, N. Takahashi and K. Kuroda, *Bull. Chem. Soc. Jpn.*, 2011, **84**, 968–975.

12 N. Tsunoji, M. Bandyopadhyay, Y. Yagenji, H. Nishida, M. Sadakane and T. Sano, *Dalton Trans.*, 2017, **46**, 7441–7450.

13 K. Isoda, K. Kuroda and M. Ogawa, *Chem. Mater.*, 2000, **12**, 1702–1707.

14 R. Ishii, T. Ikeda, T. Itoh, T. Ebina, T. Yokoyama, T. Hanaoka and F. Mizukami, *J. Mater. Chem.*, 2006, **16**, 4035–4043.

15 U. Díaz, A. Cantín and A. Corma, *Chem. Mater.*, 2007, **19**, 3686–3693.

16 H. M. Moura and H. O. Pastore, *Dalton Trans.*, 2014, **43**, 10471–10483.

17 S. Vortmann, J. Rius, S. Siegmann and H. Gies, *J. Phys. Chem. B*, 1997, **101**, 1292–1297.

18 E. Ruiz-Hitzky and J. M. Rojo, *Nature*, 1980, **287**, 28–30.

19 T. Yanagisawa, K. Kuroda and C. Kato, *Bull. Chem. Soc. Jpn.*, 1988, **61**, 3743–3745.

20 I. Fujita, K. Kuroda and M. Ogawa, *Chem. Mater.*, 2005, **17**, 3717–3722.

21 K. Park, J. Hwa, S. Kim and O. Kwon, *Appl. Clay Sci.*, 2009, **46**, 251–254.

22 K.-W. Park, S.-Y. Jeong and O.-Y. Kwon, *Appl. Clay Sci.*, 2004, **27**, 21–27.

23 C. J. Brinker and G. W. Scherer, *'SOL-GEL SCIENCE'*, ACADEMIC PRESS, 1990.

24 T. Montheil, C. Echalier, J. Martinez, G. Subra and A. Mehdi, *J. Mater. Chem. B*, 2018, **6**, 3434–3448.

25 N. Rey, S. Carenco, C. Carcel, A. Ouali, D. Portehault, M. Wong Chi Man and C. Sanchez, *Eur. J. Inorg. Chem.*, 2019, **2019**, 3148–3156.

26 J. L. Bréfort, R. J. P. Corriu, C. Guérin, B. J. L. Henner and W. W. C. W. C. Man, *Organometallics*, 1990, **9**, 2080–2085.

27 D. Mochizuki, S. Kowata and K. Kuroda, *Chem. Mater.*, 2006, **18**, 5223–5229.

28 L. Chmielarz, P. Kuśtrowski, R. Dziembaj, P. Cool and E. F. Vansant, *Microporous Mesoporous Mater.*, 2010, **127**, 133–141.

29 D. Zhao, J. Feng, Q. Huo, N. Melosh, G. H. Fredrickson, B. F. Chmelka and G. D. Stucky, *Science*, 1998, **279**, 548–552.

30 B. B. Kharkov and S. V. Dvinskikh, *J. Phys. Chem. C*, 2013, **117**, 24511–24517.

31 C. Bisio, F. Carniato, G. Paul, G. Gatti, E. Boccaleri and L. Marchese, *Langmuir*, 2011, **27**, 7250–7257.

32 T. D. Courtney, C. C. Chang, R. J. Gorte, R. F. Lobo, W. Fan and V. Nikolakis, *Microporous Mesoporous Mater.*, 2015, **210**, 69–76.

33 T. Kimura, K. Kuroda, Y. Sugahara and K. Kuroda, *J. Porous Mater.*, 1998, **5**, 127–132.

34 Y. Mitamura, Y. Komori, S. Hayashi, Y. Sugahara and K. Kuroda, *Chem. Mater.*, 2001, **13**, 3747–3753.

35 J. Pereira, L. E. Pichon, R. Dussart, C. Cardinaud, C. Y. Duluard, E. H. Oubensaid, P. Lefaucheux, M. Boufnichel and P. Ranson, *Appl. Phys. Lett.*, 2009, **94**, 071501.

36 J. Alauzun, A. Mehdi, C. Reyé and R. J. P. Corriu, *Chem. Commun.*, 2006, 347–349.

37 Y. Ide, G. Ozaki and M. Ogawa, *Langmuir*, 2009, **25**, 5276–5281.

38 Y. Li, Y. Wang, T. Tran and A. Perkins, *Spectrochim. Acta Part A*, 2005, **61**, 3032–3037.

39 J. Li, D. Cheng, T. Yin, W. Chen, Y. Lin, J. Chen, R. Li and X. Shuai, *Nanoscale*, 2014, **6**, 1732–1740.

40 P. Moriones, G. Arzamendi, A. Cornejo, J. J. Garrido and J. C. Echeverria, *J. Phys. Chem. A*, 2019, **123**, 10364–10371.

41 M. C. Brochier Salon, P. A. Bayle, M. Abdelmouleh, S. Boufi and M. N. Belgacem, *Colloids Surfaces A Physicochem. Eng. Asp.*, 2008, **312**, 83–91.

42 A. P. Amrute, B. Zibrowius and F. Schüth, *Chem. Mater.*, 2020, **32**, 4699–4706.

Chapter 5

General Conclusions

In this thesis, the surface modification of layered silicates through the approach of controlling the reactivity of the modifier led to the isolated dialkyltin species and dense organosilyl groups with well-defined local structures. In this chapter, the findings of this thesis are summarized, and the future perspectives of this research are described.

In Chapter 2, bidentate dimethyltin groups were formed by the reaction of bifunctional dimethyltin dichloride with confronting SiOH/SiO^- groups of layered octosilicates. The local structure of the immobilized dimethyltin groups was comprehensively characterized using various spectroscopic and elemental analyses. Even when excess Me_2SnCl_2 was added, the degree of the modified silanol sites was limited to approximately 50%, which might be caused by the expansion of the framework due to the larger Sn relative to the confronting silanol site. Thus, well-defined isolated tin species were successfully formed on the interlayer surfaces by controlling the number of reactive bonds in metal reagents.

In Chapter 3, dibutyltin species were successfully grafted on the interlayer surfaces of layered octosilicate. The local structure of dibutyltin-modified octosilicate was similar to that of dimethyltin-modified one, besides the slightly larger layer spacing. The dibutyltin-modified octosilicate exhibited the swelling ability with *N*-methylformamide. Furthermore, the interlayer acidity of dibutyltin-modified octosilicate was clarified by solid-state ^{31}P NMR using trimethylphosphine oxide as a probe molecule, indicating the presence of silanol groups and Lewis acid sites on the interlayer surfaces.

In Chapter 4, the effects of catalysts and functional groups on improving the degree of silylation with organoalkoxysilanes were investigated. In silylation with alkylalkoxysilanes, the presence of fluoride ions contributed to the increase in the degree of silylation without condensation between silyl groups and alkoxysilanes. In silylation

with organoalkoxysilanes having polar functional groups such as mercapto groups, a higher degree of silylation was observed even without catalysts, suggesting that ion-dipole interactions with the interlayer surface of layered silicates contribute to enhanced silylation.

In summary, this thesis demonstrates a methodology for modifying SiOH/SiO^- groups on the layer surfaces of layered silicates with well-defined chemical species using dialkyltin precursors and alkoxysilanes. In the immobilization of isolated metal species, the local structure of metal species could be controlled by matching the structure of the SiOH/SiO^- groups on the layer surface with the number of reaction points of the metal precursors. In the silylation of layered silicates with organoalkoxysilanes, it was also shown that the modification density can be increased by adding fluoride ion catalysts and designing reaction systems that consider the interaction between the interlayer surfaces and the silylating agents. Therefore, the findings in this thesis will broaden the scope of material design using layered silicates, leading to the creation of silica-based materials with advanced adsorption and catalytic properties.

List of Achievements

1. Original articles related to this thesis

(1) **M. Yatomi***, M. Koike*, N. Rey, Y. Murakami, S. Saito, H. Wada, A. Shimojima, D. Portehault, S. Carenco, C. Sanchez, C. Carcel, M. Wong Chi Man, and K. Kuroda, "Interlayer Silylation of Layered Octosilicate with Organoalkoxysilanes: Effects of Tetrabutylammonium Fluoride as a Catalyst and the Functional Groups of Silanes", *Eur. J. Inorg. Chem.* **2021**, *2021*, 1836. (*Contributed equally)

(2) **M. Yatomi**, T. Hikino, S. Yamazoe, K. Kuroda, A. Shimojima, "Immobilization of Isolated Dimethyltin Species on Crystalline Silicates through Surface Modification of Layered Octosilicate", *Dalton Trans.* **2023**, *52*, 18158.

(3) **M. Yatomi**, K. Kuroda, A. Shimojima, "Swelling Ability and Lewis Acidity of Layered Octosilicate Modified with Isolated Dialkyltin Species", *Chem. Lett.*, in press (doi:10.1093/chemle/upae020).

2. Oral or poster presentations

(1) **彌富 昌**, N. Rey, 村上 優樹, 小池 正和, 齋藤 祥平, 和田 宏明, 下嶋 敦, D. Portehault, S. Carenco, C. Sanchez, A. Ouali, C. Carcel, M. Wong Chi Man, 黒田 一幸, "層状オクトシリケート層表面へのシリル化におけるフッ化テトラブチルアンモニウム（TBAF)の効果", 日本化学会第 99 回春季年会, 3D4-04, 甲南大学, 兵庫, (2019 年 3 月).

(2) **M. Yatomi**, M. Koike, Y. Murakami, S. Saito, H. Wada, A. Shimojima, N. Rey, S. Carenco, C. Carcel, D. Portehault, M. Wong Chi Man, C. Sanchez, and K. Kuroda, "Effect of ammonium fluoride on interlayer silylation of layered silicate with organoalkoxysilanes", 3rd International Symposium of Silsesquioxane-based Functional Materials (SFM19), P11, 桐生市市民文化会館, 群馬, (July 2019).

(3) **M. Yatomi**, M. Koike, Y. Murakami, S. Saito, H. Wada, A. Shimojima, N. Rey, S. Carenco, C. Carcel, D. Portehault, M. Wong Chi Man, C. Sanchez, and K. Kuroda, "フッ化テトラブチルアンモニウムによる層状オクトシリケートの層間に対する効率的なシリル化", 第 11 回日本粘土学会若手研究者発表会, P-10, 埼玉大学, 埼玉, (2019 年 9 月).

(4) **彌富昌**, 小池正和, 村上優樹, 齋藤祥平, 和田宏明, 下嶋敦, N. Rey, S. Carenco, C. Carcel, D. Portehault, M. Wong Chi Man, C. Sanchez, 黒田一幸, "有機アルコキシシランによる層状ケイ酸塩のシリル化反応におけるフッ化物イオンの効果", 第 9 回 CSJ フェスタ 2019, P6-018, タワーホール船堀, 東京, (2019 年 10 月).

(5) **彌富昌**, 小池正和, N. Rey, 村上優樹, 齋藤祥平, 和田宏明, 下嶋敦, D. Portehault, S. Carenco, C. Sanchez, C. Carcel, M. Wong Chi Man, 黒田一幸, "種々の有機アルコキシシランによる層状ケイ酸塩のシリル化における F–触媒と官能基の影響", 第 64 回粘土科学討論会, B3, オンライン, (2021 年 9 月).

(6) **彌富昌**, 黒田一幸, 下嶋敦, "層状オクトシリケート層間のジクロロジメチルスズによる修飾", 第 65 回粘土科学討論会, B18, 島根大学, 島根, (2022 年 9 月).

(7) **彌富昌**, 片山穂南, 小池正和, 和田宏明, 黒田一幸, 下嶋敦, "ラポナイト層端面のアルコキシシリル化とポリジメチルシロキサンによる修飾", 2022 年度第 9 回 ZAIKEN フェスタ, B6, 早稲田大学, 東京, (2022 年 10 月).

(8) **M. Yatomi**, K. Kuroda, A. Shimojima, “Preparation of stannosilicates by grafting organotin species on layered silicate”, 5th International Conference on Nanospace Materials, P15, Pattaya, Thailand, (December 2022).

(9) **M. Yatomi**, “My study of layered silicates until now”, International seminar on the design and the characterization of nano materials 2022, VISTEC, Thailand, (December 2022).

ほか講演 8 件

Acknowledgements

I would like to express my greatest gratitude to Professor Dr. Atsushi Shimojima for his supervision, valuable advice, and profound research guidance. I would also like to thank Professor Dr. Yoshiyuki Sugahara and Professor Dr. Toshiyuki Momma for their productive discussion regarding this thesis.

I would like to express the great appreciation to Professor Dr. Kazuyuki Kuroda and Professor Dr. Hiroaki Wada for their fruitful discussion, earnest encouragement, and considerable support.

I am deeply thankful to all the members of the Kuroda-Shimojima-Wada group and the Shimojima group. I really appreciate Mr. Yuki Murakami for his kind guidance in the laboratory. I am also grateful to Dr. Masakazu Koike, a senior researcher in the related field, for the advice on my research. I would like to express my appreciation to Assistant Professor Dr. Takamichi Matsuno, Assistant Professor Dr. Keisuke Muramatsu, Dr. Naoto Sato, Dr. Shohei Saito, Mr. Yuta Shimasaki, and Mr. Koki Fujino, as senior doctoral course students, for valuable advice and discussion. I would like to thank Mr. Takeru Hirohashi and Ms. Rika Sakai, senior members of the relevant field, for the fruitful discussion. I would like to express my gratitude to Mr. Taiki Hayashi, Mr. Takuya Hikino, and Mr. Yoshiaki Miyamoto for their continuous encouragement as colleagues in the doctoral course. I received a great deal of discussion and assistance with my research from Mr. Yosuke Oka, Ms. Ayaka Komatsu, Mr. Hiroki Noda, Ms. Honami Katayama, Mr. Yuta Hattori, Mr. Takahiro Mizuno, Ms. Nonna Hori, Mr. Takeshi Iwakami, Ms. Riho Wakino, and Mr. Sota Hasebe. I am deeply grateful to Ms. Sadae Himeshima for her office consultations and daily kindness.

I would like to express the great appreciation to Dr. Nadège Rey, Dr. Carole Carcel, Dr. Michel Wong Chi Man (Univ Montpellier), Dr. David Portehault, Dr. Sophie Carenco, and Professor Dr. Clément Sanchez (Sorbonne Université) for their fruitful discussion of research in Chapter 4. I am very grateful to all the members in Materials Characterization Central Laboratory, Kagami Memorial Research Institute for Materials Science and Technology, and Environmental Safety Center at Waseda University, especially, Dr. Toshimichi Shibue, Dr. Natsuhiko Sugimura, Dr. Noriko Hanzawa, Mr. Shinpei Enomoto, and Dr. Ryota Takahashi, for their analytical supports and fruitful discussion. I am also grateful to Associate Professor Dr. Seiji Yamazoe (Tokyo Metropolitan University) for expert advice on XAFS analysis.

I gratefully acknowledge financial supports by the JST SPRING (No. JPMJSP2128) and Grant-in-Aid for JSPS Fellows (No. 22J13718).

Finally, I would like to extend my most sincere to my family, Mr. Tatsunari Yatomi, Ms. Kyoko Yatomi, and Mr. Satoshi Yatomi, for their endless love, understanding, support, encouragement, and sacrifice throughout my life.